PHOTODISSOCIATION OF THE ACENAPHTHENE, ACENAPHTHYLENE, AND BENZOFLUORENE CATIONS

By

JOHN JAMES BANISAUKAS III

A DISSERTATION PRESENTED TO THE GRADUATE SCHOOL
OF THE UNIVERSITY OF FLORIDA IN PARTIAL FULFILLMENT
OF THE REQUIREMENTS FOR THE DEGREE OF
DOCTOR OF PHILOSOPHY

UNIVERSITY OF FLORIDA

2003

TABLE OF CONTENTS

page

ABSTRACT iv

CHAPTER

1 BACKGROUND 1

Unidentified Infrared Emission Bands 1
Polycyclic Aromatic Hydrocarbons 5
Relevant PAH Cation Studies 8
Current Research Goals 17

2 METHODS 19

Density Functional Theory Calculations 19
Fourier Transform Ion Cyclotron Resonance Mass Spectrometry 21
Matrix Isolation Spectroscopy 31

3 ACENAPHTHENE 38

Background 38
DFT Calculations 41
FT-ICR Photodissociation Studies 49

4 ACENAPHTHYLENE 59

Background 59
DFT Calculations 62
FT-ICR Photodissociation Studies 67

5 AGGREGATION OF THE ACENAPHTHYLENE CATION 82

Cyclobuta[1,2-α:3,4-α′]diacenaphthylene 82
1,1′-Bi-(acenaphthenylidene) 95
Comparison to the Acenaphthylene Aggregate 106

6 BENZOFLUORENE 115

Background 115

DFT Calculations 117
FT-ICR Photodissociation Studies 125
Infrared and UV-visible Spectroscopy 141

7 SUMMARY AND CONCLUSIONS 168

Acenaphthene 168
Acenaphthylene 169
Benzofluorene 170
PAHs Containing Pentagonal Rings 171

REFERENCE LIST 173

BIOGRAPHICAL SKETCH 178

Abstract of Dissertation Presented to the Graduate School
of the University of Florida in Partial Fulfillment of the
Requirements for the Degree of Doctor of Philosophy

PHOTODISSOCIATION OF THE ACENAPHTHENE, ACENAPHTHYLENE, AND BENZOFLUORENE CATIONS

By

John James Banisaukas III

August 2003

Chair: Dr. Martin Vala
Major Department: Department of Chemistry

Polycyclic aromatic hydrocarbons (PAHs) are considered to be carriers of the unidentified infrared (UIR) emission bands observed from a variety of interstellar objects. In harsh stellar environments, these PAHs are likely ionized and fragmented by ultraviolet radiation. In this work, photofragmentation pathways and spectroscopic properties were investigated for three PAHs containing pentagonal rings: acenaphthene, acenaphthylene, and benzofluorene.

Photofragmentation routes were characterized for acenaphthene, acenaphthylene, and benzofluorene cations using Fourier transform ion cyclotron resonance (FT-ICR) mass spectrometry. Ions were trapped in an ICR cell and irradiated with light from a xenon arc lamp for various lengths of time. The acenaphthene and acenaphthylene cations lost only hydrogen atoms upon UV irradiation, whereas the photofragmentation of benzofluorene involved carbon loss. Infrared and electronic absorption spectra were collected for neutral and cationic benzofluorene trapped in solid argon at 12 K. Infrared absorption bands observed for the benzofluorene cation matched several of the UIR emission bands. Density functional theory calculations yielded optimized geometries, ground-state energies, and vibrational frequencies for each PAH cation. Predicted vibrational frequencies correlated well with those observed in solid argon.

Evidence of an acenaphthylene aggregate ion was observed in FT-ICR studies. Although neutral acenaphthylene dimerization has been well characterized, the structure and properties of the dimer-like ion are unknown. Photofragmentation pathways and predicted structures for the acenaphthylene aggregate ion are reported in this work.

CHAPTER 1
BACKGROUND

Determining the composition of interstellar molecular clouds is an active area of astronomical research. Identification of material in these regions provides insight on astrophysical processes, such as star formation and collapse. Spectroscopic investigation of these clouds requires light from nearby stars. Absorption spectra are recorded by comparing the spectral profiles of stars behind and in front of dense regions of interstellar matter. Emission spectra are collected for species excited by stellar energy. Although comparison of astronomical and laboratory spectra has led to the identification of a variety of species in the interstellar medium, the sources of many spectroscopic features remain undetermined.

Unidentified Infrared Emission Bands

Emission Feature Observation

In 1973, Gillet et al. observed continuum radiation features between 8 μm and 13 μm emitted from two planetary nebula: NGC 7027 and BD+30°3639.[1] This continuum radiation was defined by a broad feature at 8.6 μm and a strong band at 11.3 μm. Investigation of the 2-8 μm spectral range of NGC 7027 revealed additional features at 3.3 μm, 6.2 μm, and 7.7 μm.[2,3] These features were broader than the instrument resolution, yet narrower than a blackbody distribution. Moreover, these features could not be reasonably matched to blends of atomic lines. Collectively, these bands at 3.3 μm, 6.2 μm, 7.7 μm, 8.6 μm, and 11.3 μm became known as the unidentified infrared (UIR) emission bands. This set of five bands has been observed in a variety of astronomical objects and regions: planetary nebulae, reflection nebulae, bipolar nebulae, galaxy nuclei, and the diffuse interstellar medium. All objects exhibiting the UIR bands contain interstellar matter and are close to sources of ultraviolet radiation.

Several weaker bands have since been discovered in the same spectral region. However, the appearance of these bands varies significantly with position within astronomical objects. Emission bands at 3.40 μm, 3.46 μm, 3.51 μm, and 3.57 μm have been observed on top of a rounded plateau extending from 3.2 μm to 3.6 μm.[4] Recently, high resolution spectra in the 10 μm to 13 μm range revealed additional features around the prominent 11.3 μm band.[5] These distinct features, located on the shoulders of the 11.3 μm band, were also spatially dependent.

Astrophysical Environment

The possible carriers of the UIR bands are limited by the chemical composition of the astrophysical environment. Hydrogen is the most abundant element in the interstellar medium (density ~1 cm^{-3}).[6] The abundance of helium is approximately 0.1% of the hydrogen abundance. Carbon, oxygen, and nitrogen all exhibit fractional abundances of ~10^{-4} with respect to hydrogen. The fractional abundances of other elements (neon, magnesium, silicon, sulfur, and iron) are lower than 10^{-4}. The interstellar medium contains a mixture of dust grains and gas-phase molecules. The most abundant elements condensed into dust grains are carbon and oxygen.[7] The grain cores are believed to consist mostly of silicates and carbon. Grain mantles contain a variety of elements as well as small molecules, such as H_2O, CH_4, and NH_3.[8] Grain particle sizes are estimated between 3 nm and 300 nm.[6]

The type of material present in astronomical objects and the interstellar medium depends on the local ultraviolet field. Material at the surface of interstellar clouds is subject to a harsher UV environment than material shielded within the cloud interior. The diffuse interstellar medium experiences a UV photon flux of approximately 5.9×10^{8} photons cm^{-2} s^{-1}.[9] Material within the Orion Bar is subjected to 1.1×10^{13} photons cm^{-2} s^{-1}. Photon fluxes for the NGC 7027 and BD+30°3639 planetary nebulae are 4.6×10^{13} photons cm^{-2} s^{-1} and 1.7×10^{14} photons cm^{-2} s^{-1}, respectively. A higher photon flux of 1.6×10^{15} photons cm^{-2} s^{-1} is observed for the HD44179 protoplanetary nebula. Thus, the spatial dependence of several of the UIR bands may correlate with the relative UV field.

Proposed Emission Mechanisms

Initial proposals for sources of UIR emission focused on dust grains in the interstellar medium. Allamandola et al. suggested that small molecules or radicals frozen in grain mantles could be excited by UV radiation and emit during vibrational mode relaxation.[8] However, matching this emission to the ubiquitous UIR bands required improbable, constant composition for the grain mantles. Similarly, Duley and Williams proposed that functional groups on the surface of graphitic grains would emit at the characteristic UIR wavelengths.[10] In this model, carbon-hydrogen stretching and bending vibrations would account for the 3.3 μm and 11.3 μm bands. However, fitting the remaining UIR bands required functional groups that would also emit at non-UIR wavelengths. The major problem with both models was non-radiative energy transfer to the grain instead of radiative emission by molecules or functional groups on the grain surface. Subsequent emission by the grain would occur in the far-infrared region instead of at the characteristic UIR wavelengths.

Thermal emission by small heated grains was also proposed as a source of the UIR bands. Dwek et al. proposed that small grains (r = 100 Å) heated radiatively to a thermal equilibrium would emit in the near IR region.[11] However, modeling the bands as blackbody emission required an equilibrium temperature of 1500 K, which was relevant only for grains very close to stars. To account for high grain temperatures at greater distances from radiation sources, Sellgren suggested transient heating of much smaller grains (r = 5 Å) by ultraviolet photons.[12] Due to the low heat capacity of these small grains, absorption of a UV photon (~10 eV) could momentarily raise the grain temperature by 1000 K, allowing thermal emission at large distances from stellar sources.

Leger and Puget proposed that the small carbon grains described by Sellgren were actually large polycyclic aromatic hydrocarbon (PAH) molecules.[13] According to this IR emission model, absorption of a UV photon by a large PAH molecule results in an electronic excitation. The absorbed energy is then transferred non-radiatively to the molecule's vibrational modes in less than 10^{-12} s. Relaxation from the excited vibrational levels to the vibrational ground state results in photon emission in the near-IR range.

Comparison of the predicted emission spectrum of coronene ($C_{24}H_{12}$) with the observed UIR emission bands provided support for this large PAH hypothesis. The calculated emission spectrum of coronene heated to 600 K contained strong bands at 3.3 μm, 6.2 μm, 7.6 μm, 8.85 μm, and 11.9 μm, which correlated well with the UIR features at 3.3 μm, 6.2 μm, 7.7 μm, 8.6 μm, and 11.3 μm. The 3.3 μm and 6.2 μm emission bands in coronene were assigned to aromatic C-H and aromatic C-C stretching modes, respectively. The 8.85 μm and 11.9 μm bands were assigned to in-plane and out-of-plane aromatic C-H bends. Although not an exact match, the strong correlation between the coronene emission bands and the observed UIR features supported PAHs as carriers of the UIR emission bands.

Polycyclic Aromatic Hydrocarbons

The presence of polycyclic aromatic hydrocarbons in the interstellar medium fits within the available carbon budget proposed by Snow and Witt.[14] However, only a limited number of PAH forms is allowed. The nature of the PAH species present depends on both formation mechanisms and interstellar conditions.

PAH Formation

The PAH hypothesis of Leger and Puget depended on the sublimation of PAH molecules from graphitic grains.[13] A small spherical grain of 50 carbon atoms would have a radius of 4.8 Å. Therefore, this grain would consist of two layers of graphite with an interplane distance of 3.35 Å. As proposed by Duley and Williams, the carbon atoms at the edge of these graphitic planes would most likely be hydrogenated.[10] Because interplane binding in graphite layers is relatively weak (0.06 eV), these hydrogenated graphite layers could separate to form large PAH molecules at high temperatures.

An alternative source of PAH molecules is the condensation of interstellar carbon.[15,16] This condensation occurs in regions of high carbon abundance, such as stellar winds from carbon stars. The most abundant elements in these regions are hydrogen, carbon, oxygen, and nitrogen.[16] Hydrogen and nitrogen are mostly in their molecular forms. Carbon is present as carbon monoxide and acetylene (C_2H_2). Temperatures in these stellar winds range from 750 K to 950 K. Pressures range from 10^{-9} Torr to 10^{-6} Torr.[15]

Because only the carbon present as acetylene is condensable under these conditions, the accepted model of PAH formation involves sequential addition of acetylene molecules to form aromatic rings. Prior to each acetylene addition, hydrogen abstraction is required to create an active radical site. Free atomic hydrogen reacts with hydrogen attached to the growing carbon chain or ring to form molecular hydrogen. The first two PAHs formed by this condensation mechanism are naphthalene, which consists of two six-membered rings, and acenaphthylene, which contains an additional five-membered ring. Subsequent acetylene additions and structural rearrangements allow formation of a wide variety of PAH molecules. Condensation is eventually terminated by dilution of the gas in the wind, consumption of the available carbon, or conversion of all atomic hydrogen to molecular hydrogen. Keller proposed that the most thermodynamically favorable condensation products would be compact PAHs containing both five-membered and six-membered rings.[15]

Dehydrogenated PAHs

In highly vibrationally excited PAH molecules, bond fragmentation may compete with IR photon emission as a relaxation mechanism.[4] Based on relative bond energies in PAHs, hydrogen loss is more likely than carbon loss. The energy required to break an aromatic C-H bond is approximately 4.5 eV, whereas the energy required to break an aromatic C-C bond is approximately 5.5 eV. Furthermore, removal of a carbon atom from a PAH molecule requires breaking two C-C bonds (11 eV) simultaneously, which is less likely than simple hydrogen loss. Geballe et al. proposed that small PAH molecules would be completely stripped of hydrogens in high UV fields.[4] Larger PAHs were not likely to reach the critical energy required for C-H bond fragmentation. In shielded environments, hydrogen reattachment would compete with photofragmentation; therefore, PAHs in these regions would be completely hydrogenated.

In PAH molecules, the aromatic C-H out-of-plane bends in the 10-14 μm range are strongly dependent on the number of adjacent hydrogens. For a carbon-hydrogen bond with no hydrogens on adjacent carbons (solo C-H), this out-of-plane bend occurs in the 11.1 μm to 11.6 μm range. Increasing the number of adjacent hydrogens shifts this vibrational mode to higher wavelengths: 11.6 μm to 12.5 μm for one adjacent hydrogen (duo C-H), and 12.4 μm to 13.3 μm for two adjacent hydrogens (trio C-H). The observed UIR emission feature at 11.3 μm (solo C-H) indicated low hydrogen coverage for emitting PAHs.[13] Additionally, because the observed intensity of the C-C stretching mode (6.6 μm) was greater than the intensity of the C-H bending mode (11.3 μm), the number of C-H emitters was expected to be small. Thus, PAH molecules were possibly partially dehydrogenated in the interstellar medium.

Hydrogenated PAHs

The majority of UIR emission profiles include a strong feature at 3.3 μm and weaker bands between 3.3 μm and 3.6 μm. For example, the protoplanetary nebula IRAS 05341 exhibits such emission features at 3.294 μm and 3.419 μm.[17] The 3.3 μm band has been attributed to aromatic C-H stretching vibrations in PAH molecules. The weaker bands between 3.3 μm and 3.6 μm, however, are more characteristic of aliphatic C-H stretching vibrations. As such, sources of these bands may include hydrogenated PAHs with aliphatic components or side-chains.[18] Based on the observed intensity ratios of the aromatic C-H (3.3 μm) and aliphatic C-H (3.4 μm) stretching modes, Schutte et al.

proposed that 1% to 2% of peripheral PAH binding sites may be doubly-hydrogenated in interstellar regions where the 3.4 μm emission band appears.[9]

PAH Cations

Due to the low ionization potential of PAH molecules (6-10 eV), Allamandola et al. proposed that PAHs were likely ionized by UV photons from stellar sources.[19] The degree of ionization would vary with the photon flux associated with different astronomical objects. For example, nearly all PAHs within a nebula would be ionized, whereas a mixture of PAH neutrals and cations could exist in the interstellar medium.[17] The relative intensities of the UIR bands were found to vary with distance from sources of UV radiation. For the NGC 1333 reflection nebula, the ratio of the 8.6 μm band to the 11.3 μm band decreased as the distance from the star increased.[17] Because both PAH ionization and relative UIR intensities were dependent upon distance from UV sources, PAH cations were suggested as possible carriers of the UIR bands.

Relevant PAH Cation Studies

Theoretical and experimental IR spectra for PAH cations and neutrals revealed that IR band intensities for PAHs varied significantly with charge state.[20-23] Laboratory spectra for PAH neutrals exhibited C-C modes weaker than the C-H out-of-plane modes. In astronomical spectra, however, the C-C modes (6-9 μm) are stronger than the C-H out-of-plane bends (10-13 μm).[5] The C-C stretches and C-H in-plane bends (6-9 μm) are much stronger for PAH cations than for PAH neutrals. Also, the C-H out-of-plane bends (11-14 μm) are weaker in the PAH cation than in the PAH neutral. Thus, the intensity ratios observed for PAH cations eliminated the need for extensive PAH dehydrogenation in explaining the relative UIR band intensities. Because the infrared spectra of PAH cations closely matched the intensity distribution of the UIR emission bands, recent research has focused on PAH cations in their unperturbed, fragmented, or hydrogenated forms.

Computational Studies

Harmonic frequencies and intensities were calculated via density functional theory (B3LYP/4-31G) for a large class of neutral and cationic PAHs by Langhoff.[21] Infrared spectra were predicted for both linear and compact PAHs containing only six-membered rings. In general, harmonic frequencies and relative intensities of PAH cations provided a better fit to astronomical data than their neutral counterparts. The total integrated intensity was substantially higher for PAH ions than for neutral PAHs, and increased quadratically with system size. Predicted spectra for linear PAH cations contained strong bands falling between the observed 6.2 μm and 7.7 μm UIR bands. Therefore, large, compact PAH cations were proposed as carriers of the UIR emission features.

Because infrared spectra for ionized PAHs provided a better match for the UIR bands, the need for extensive PAH dehydrogenation was reevaluated. The combined effects of ionization and dehydrogenation were studied by Pauzat et al. for anthracene ($C_{14}H_{10}$) and pyrene ($C_{16}H_{10}$).[20] Infrared spectra were calculated (HF/3-21G) for the fully-hydrogenated, doubly-dehydrogenated, and quadri-dehydrogenated neutral and cationic PAHs. Ionization significantly increased the intensity ratio of C-C vibrations to C-H stretching modes, and blueshifted the out-of-plane C-H bending modes. Dehydrogenation of the PAH ions created benzyne bonds with strong vibrational modes around 5.0 μm. The frequencies of these benzyne modes correlated well with weak UIR bands observed in the 5.1-5.3 μm range.[24] However, the low intensity of the 5.1-5.3 μm UIR bands suggested that the number of benzyne bonds is small. Thus, only partial dehydrogenation is expected for PAH cations in the interstellar medium. In general, the calculated IR spectra of compact, doubly-dehydrogenated PAH cations provided a good match to the observed UIR features.

The abundance of hydrogen is estimated to be 10,000 times the abundance of PAH molecules in regions of UIR emission. Therefore, the reaction of hydrogen with PAH cations may be an important process in the interstellar medium. Naphthalene and pyrene cations were found to rapidly react with atomic hydrogen in selected ion flow tube (SIFT) experiments conducted by Snow et al.[25] Reaction energies and barrier heights were calculated for the reaction of the naphthalene cation ($C_{10}H_8^+$) with atomic hydrogen by Bauschlicher.[26] The addition of one hydrogen to $C_{10}H_8^+$ was calculated to be exothermic (-62.1 kcal/mol) with no reaction barrier. The addition of a hydrogen to the 1-hydronaphthalene cation ($C_{10}H_9^+$) was also exothermic (-45.8 kcal/mol). Bauschlicher suggested that hydrogenated PAH cations formed by these exothermic reactions could stabilize through IR emission. Furthermore, addition of the second hydrogen to an adjacent carbon reduces the aromatic character of the PAH cation. This lowered aromaticity is consistent with the weaker C-H stretching modes observed in the UIR emission bands.

Because the UIR emission bands are likely due to a mixture of PAHs rather than a single PAH species, the UIR bands have been modeled using experimental and theoretical spectroscopic data for PAH neutrals and cations. Based on available experimental and theoretical IR cross sections, Bakes et al. created a model to calculate the IR emission spectra of PAHs as a function of charge state and interstellar UV field strength.[27,28] The PAH populations modeled were divided into five structural classes: symmetric condensed, symmetric noncondensed, linear, pentagonal ring containing, and methylated PAHs. Although symmetric condensed PAHs more accurately fit the observed UIR emission bands, charge state appeared to have a greater effect on the IR emission spectrum than molecular structure variations.

Matrix Isolation Spectroscopy

Because it approximates the collision-free astrophysical environment, matrix isolation spectroscopy has been widely applied to the study of PAHs.[22,23,29-37] In general, neutral or cationic PAHs are trapped in a low temperature, solid rare-gas matrix, which provides an isolated environment with little perturbation. Infrared or electronic spectra are then recorded for the matrix isolated PAH species. The PAH cations can be produced either prior to or following PAH deposition in the matrix.

One method of PAH cation production involves photolysis of neutral PAHs trapped in the rare gas matrix. Hudgins and coworkers deposited a mixture of argon and PAH vapor on a 10 K window.[22,29-31] Trapped PAHs were ionized by irradiating the matrix with a microwave-powered flow discharge hydrogen lamp (10.2 eV). The PAH ions were identified through comparison of infrared spectra collected before and after matrix irradiation. Addition of electron acceptors (CCl_4 or NO_2) to the matrix in parallel experiments increased the concentration of PAH cations, supporting identification of PAH cation bands. Neutral and ionic PAH bands were assigned based on calculated harmonic frequencies. The PAH cations studied to date by Hudgins et al. include naphthalene,[22,29] phenanthrene,[29] pyrene,[29] benzopyrene,[29] benzoperylene,[29] coronene,[29] the series of polyacenes through pentacene,[30] fluoranthene,[31] and the four isomers of benzofluoranthene.[31]

In experiments conducted by Vala and coworkers, PAH cations were formed by electron bombardment of PAH/argon/CCl_4 gas mixtures prior to matrix deposition.[23,32-37] The gas mixture containing both neutral and ionic species was condensed on a BaF_2 or CsI window at 12 K. Because electron bombardment yields neutral, cationic, and fragmented PAH species, the absorption spectra were quite complex. Deposited species were identified through photolysis and annealing techniques, as well as through correlation of IR and electronic spectra recorded for the same matrix. Neutral, cationic, and fragment bands were assigned based on calculated harmonic frequencies and predicted vertical excitation energies. The PAH cations studied to date by Vala and coworkers include naphthalene,[23,32,33] pyrene,[23,33] anthracene,[23,33,34] perylene,[23,33] coronene,[33] fluorene,[35,36] acenaphthylene,[37] and acenaphthene.[37]

Gas-Phase Infrared Absorption and Emission

Absorption spectra collected for matrix isolated PAH cations often lack species selectivity and are subject to matrix perturbations. Although these shortcomings are absent in gas-phase experiments, the ion densities required for standard infrared absorption techniques are unattainable in the gas phase due to space charge effects. However, gas-phase infrared photodissociation spectroscopy does not require high ion concentrations. The infrared photodissociation spectra of gas-phase PAH cations have been reported by Piest et al.[38,39] and Oomens et al.[40,41] The PAH cations were trapped in a Paul-type quadrupole ion trap and irradiated with the pulsed, tunable output (5 μm to 250 μm) of a free electron laser (FEL). Fragments produced during multiphoton dissociation were extracted into a time-of-flight mass spectrometer. Both hydrogen and C_2H_2 fragmentation channels were monitored as a function of IR laser wavelength. Due to the limited resolution of the ion trap, the loss of two hydrogens was monitored as an increase in the low mass shoulder of the parent ion peak.

Recent IR photodisscociation studies focused on PAH cations containing a five-membered ring: indane (C_9H_{10}), acenaphthene ($C_{12}H_{10}$), fluorene ($C_{13}H_{10}$), and fluoranthene ($C_{16}H_{10}$).[41] The IR spectra of the indane, fluorene, and fluoranthene cations contained intense bands due to aromatic ring breathing modes in the 10 μm region. Because the UIR spectrum does not exhibit bands in this region, these PAH cations are not likely to be carriers of the UIR emission bands. Acenaphthene, however, did not exhibit these breathing modes. Each aromatic six-membered ring in the acenaphthene cation is fused directly to another aromatic ring. At least one aromatic ring in the indane, fluorene, and fluoranthene cations is fused only to the pentagonal ring. Thus, if PAH cations containing pentagonal rings contribute to the UIR emission bands, the aromatic six-membered rings in the cation must be fused directly to another aromatic ring.

Because absorption and emission spectra differ significantly for vibrationally excited molecules, the collection of infrared emission spectra for PAH cations is a high priority. Infrared emission spectra of gas-phase pyrene cations ($C_{16}H_{10}^+$) have recently been recorded via single photon infrared emission spectroscopy (SPIRES).[42,43] This technique approximates interstellar PAH emission in that a gas-phase PAH molecule emits IR photons after absorbing energy. Instead of UV photon excitation, however, pyrene was both ionized and excited by high-energy electron bombardment. Pyrene cations were then directed into a cooled (77 K) sample chamber where IR emission was recorded with an IR single-photon counting fluorescence spectrometer. The emission spectrum of the pyrene cation closely matched several UIR features. Electron ionization of pyrene also generated fragment ions, the most stable of which were the doubly-dehydrogenated ($C_{16}H_8^+$) and quadri-dehydrogenated ($C_{16}H_6^+$) ions. The emission spectra collected for the dehydrogenated pyrene fragment ions provided a slightly better fit, especially in the 7.7 μm region. Bands in this region were assigned to vibrational modes involving the benzyne bond present only in the dehydrogenated species. Thus, dehydrogenated PAH cations seemed to be likely candidates for the UIR band carriers.

Photodissociation Experiments

The mechanism for PAH photodissociation by multi-photon absorption was described by Boissel et al. in a Fourier transform ion cyclotron resonance (FT-ICR) mass spectrometric study of PAH cations.[44,45] Anthracene ($C_{14}H_{10}$) or pyrene ($C_{16}H_{10}$) cations were trapped in a cooled (30 K) ICR cell in a 0.85 Tesla magnet and fragmented with UV irradiation from a Xe arc lamp. Through use of long-pass filters, irradiation was limited to wavelengths longer than 590 nm. Upon irradiation, pyrene cations lost a maximum of four hydrogens. The primary photofragment of anthracene corresponded to loss of an acetylene (C_2H_2) unit. Because the highest available photon energy (2.1 eV) was lower than the binding energy of both hydrogen and acetylene, the fragmentation of pyrene and anthracene involved absorption of multiple photons.

The proposed multi-photon absorption mechanism requires competition between fluorescence and non-radiative internal conversion. After absorption of the first photon by the PAH cation, the absorbed energy is distributed among the vibrational degrees of freedom before fluorescence can occur. Absorption of an additional photon prior to radiative cooling raises the molecule to an internal energy greater than that of a single absorbed photon. In this manner, multiple photons can be absorbed until the fragmentation threshold of the PAH ion is reached. For example, sequential absorption of four photons (2.1 eV apiece) is required to remove an acetylene molecule from the anthracene cation.

The photofragmentation of a large class of PAH cations was investigated by Ekern et al. via FT-ICR mass spectrometry.[46,47] The PAH cations were trapped in an ICR cell at the center of a 3 Tesla magnetic field and irradiated with a UV photon flux of 10^{17} photons cm^{-2} nm^{-1} s^{-1} for 0.5 s. Fragmentation patterns were determined by comparing the mass spectra recorded before and after UV irradiation. Based on these fragmentation patterns, the PAHs studied were classified as photostable, losing hydrogen only, losing carbon and hydrogen, or photodestroyed.

Although it was previously proposed that only large PAHs containing more than 50 carbon atoms could survive the harsh interstellar environment,[48] the photostable PAH cations observed by Ekern et al. were among the smallest studied. All photostable PAH cations studied contained at least one four-membered or five-membered ring. Proposed explanations for this photostability included unattainable dissociation energy barriers, short radiative lifetimes, or unfavorable absorption profiles. No simple correlation was found between fragmentation patterns and PAH size, structure, or symmetry. However, with only a few exceptions, acetylene loss appeared to be limited to PAH ions containing four adjacent hydrogens on a six-membered ring not fused to a four-membered or five-membered ring. In most cases, if an exposed six-membered ring was not present, only hydrogen loss was observed. Thus, compact PAHs tend to lose only hydrogens whereas non-compact PAHs can lose both hydrogens and acetylene units.

Although the photodissociation patterns of many PAH ions were described by Ekern et al.,[46,47] the actual structures of the photofragments were not determined. Furthermore, the photofragmentation pathways were not investigated. Based on photoion mass spectrometry (PIMS) experiments, Jochims et al. proposed three low-energy photofragmentation channels for PAH ions: loss of hydrogen atoms, loss of hydrogen molecules (H_2), and loss of acetylene (C_2H_2).[49,50] Of these pathways, single hydrogen loss was determined to be the most energetically favorable. The structural dependence of PAH photodissociation was investigated in terms of the single hydrogen loss pathway.[51] It was determined that highly conjugated PAH ions containing more than 30-40 carbon atoms should be photostable in interstellar regions of moderate UV photon energy ($\leq$ 13.6 eV). Small PAH ions containing less than 30-40 carbon atoms and PAH ions containing methyl side groups would not be photostable under these conditions. However, the photostability of the singly-dehydrogenated PAH ions was not investigated.

Recently, photodissociation pathways and fragment ion structures were reported for the fluorene cation ($C_{13}H_{10}^+$) by Dibben et al.[52,53] Photofragmentation pathways were determined via FT-ICR mass spectrometry.[52] Fluorene cations trapped in an ICR cell at the center of a 2 Tesla magnet were irradiated with the continuous output of a Xe arc lamp for one to four seconds. Dissociation pathways were determined by ejecting specific fragment ions during lamp irradiation and noting the effect on the resulting mass spectrum. The primary photodissociation pathway for the fluorene cation was the sequential loss of five hydrogens. Fragment ions underwent a variety of dissociation pathways including single hydrogen, double hydrogen, and carbon fragment loss. Pathway energies and photoproduct structures were determined through density functional theory calculations.[53] Several monocyclic ring structures were proposed to account for the observed photofragment ions.

Current Research Goals

It is generally accepted that the carriers of the UIR emission bands are PAH cations. However, the structures of PAH ions that are stable under astrophysical conditions are still undetermined. The majority of PAH cation studies to date have focused on large PAH cations containing only aromatic six-membered rings. However, small PAH ions containing at least one four or five-membered ring were found to be relatively photostable by Ekern et al.[47] Furthermore, the interstellar PAH cations may be partially dehydrogenated, making the study of PAH fragment ions a high priority. The research presented in this study focuses on three PAHs containing a pentagonal ring: acenaphthene, acenaphthylene, and benzofluorene.

The spectroscopic properties and photochemical behavior of these PAH cations and subsequent fragment ions are investigated via density functional theory (DFT) calculations, Fourier transform ion cyclotron resonance (FT-ICR) mass spectrometry, and matrix isolation spectroscopy. Fragmentation energies, fragment ion structures, and harmonic vibrational frequencies are calculated through application of density functional theory. The photofragmentation pathways of these PAH cations are characterized with FT-ICR mass spectrometry. The infrared and electronic absorption spectra recorded for neutral and cationic benzofluorene trapped in solid argon are compared to the UIR emission features. The infrared and electronic absorption spectra of matrix isolated acenaphthene and acenaphthylene have previously been reported,[37] and will not be described in detail in this work.

CHAPTER 2
THEORETICAL AND EXPERIMENTAL METHODS

Density Functional Theory Calculations

To support experimental data, theoretical calculations were conducted for each PAH system studied. Optimized geometries, vibrational frequencies, ground-state energies, and carbon-hydrogen bond energies were calculated for PAH neutrals and cations using density functional theory methods in the Gaussian 98 platform.[54] The B3LYP hybrid density functional theory method was applied in conjunction with the 4-31G, 6-31G(d,p), or 6-311+G(d,p) basis set. The B3LYP hybrid functional is a modification of the original Becke hybrid functional.[55] The B3LYP/4-31G level of theory accurately predicts the C-H bond energy of C_6H_6, and thus has been widely applied to PAH systems.[26] Due to addition of a set of d functions to carbon and a set of p functions to hydrogen, the 6-31G(d,p) and 6-311+G(d,p) basis sets yield lower, and inherently more accurate, vibrational frequencies than the 4-31G basis set. However, since predicted frequencies are scaled to match experimental vibrational bands, the less accurate 4-31G basis set is routinely applied to larger PAH systems to reduce computational cost.

Optimized Geometries and Vibrational Frequencies

The geometries of each PAH neutral and cation were optimized to attain a minimum potential energy for each system. Geometry optimization calculations yielded bond lengths, bond angles, and spin densities. Following geometry optimization, harmonic vibrational frequencies and intensities were calculated for each PAH neutral and cation. These frequency calculations also yielded ground-state energies and zero-point energy corrections. Zero-point energies were scaled to bring theoretical and experimental vibrational frequencies into agreement.

In an extensive computational study of a large class of PAHs, Langhoff reported an average scaling factor of 0.958 for vibrational frequencies of PAH neutrals and cations calculated at the B3LYP/4-31G level of theory.[21] Scaling factors were determined by comparing the predicted IR frequencies of each PAH studied with the vibrational bands observed experimentally in an argon matrix. Typically, C-H stretches required a lower scaling factor than C-C stretches. Increasing the basis set to either 6-31G(d) or 6-31G(d,p) reduced the predicted frequencies. Scaling factors for these more accurate basis sets were typically higher than those required for the 4-31G basis set.[21] In the current work, a scaling factor of 0.978 was calculated to fit the theoretical harmonic frequencies to experimentally observed vibrational bands. This factor correlates well with those reported by Langhoff.

Bond Energies and Predicted Dehydrogenation Pathways

Carbon-hydrogen bond energies were calculated by comparing the corrected ground-state energies of PAH molecules before and after hydrogen removal. The energy difference between the parent molecule energy and the sum of the fragment molecule energy and atomic hydrogen energy corresponds to the energy required to remove a hydrogen atom from the parent molecule. An example of this bond energy calculation for neutral acenaphthene is shown in Figure 2-1.

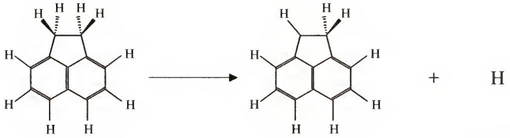

$-463.1512405\ E_h$ $-462.5211767\ E_h$ $-0.500273\ E_h$

$$\text{Dehydrogenation Energy} = 0.129791\ E_h = 3.53\ \text{eV}$$

Figure 2-1. Calculation of the energy required for hydrogen abstraction from neutral acenaphthene ($C_{12}H_{10}$).

In order to determine the primary sequential dehydrogenation pathway for a particular PAH molecule, all C-H bond energies within the molecule were calculated. Assuming the hydrogen with the smallest C-H bond energy was the first hydrogen removed, the most probable structure of the singly-dehydrogenated PAH was determined. Prediction of subsequent hydrogen removal required calculating all C-H bond energies for the new singly-dehydrogenated structure. Occasionally, several C-H bond energies were too close in magnitude ($\Delta E < 10\%$) to determine the most probable hydrogen removed. In these cases, the dissociation of each C-H bond was considered, leading to multiple routes for the predicted dehydrogenation.

Fourier Transform Ion Cyclotron Resonance Mass Spectrometry

Fourier transform ion cyclotron resonance (FT-ICR) mass spectrometry was used to investigate the photofragmentation of PAH cations. The long ion storage times and high mass resolution inherent to FT-ICR mass spectrometry enabled characterization of PAH photoproducts and photofragmentation pathways.

Experimental Apparatus

All experiments were performed on a FT-ICR mass spectrometer inserted into the bore of an unshielded superconducting magnet (Figure 2-2). The magnet was 58.5 cm long, with a bore diameter of 21.5 cm. The magnetic field measured at the center of the bore was 2.038 Tesla. The vacuum chamber was pumped to 10^{-9} Torr by a 700 L/s diffusion pump (Alcatel). The method of PAH sample introduction was determined by the vapor pressure of the PAH. Low molecular weight PAHs (MW < 200 amu) with relatively high vapor pressures were loaded into a glass sample tube and attached to an inlet port located 1.2 m from the center of the magnet. The PAH vapor was leaked into the system through a variable leak valve (Varian, model 951-5100). Adjustment of a sapphire-copper alloy valve seal within the leak valve provided ultra-fine control of gas flow and overall sample pressure. The minimum achievable flow rate was 10^{-9} TorrL/s. High molecular weight PAHs (MW > 200 amu) with relatively low vapor pressures were vaporized by a resistively heated stainless steel probe. The PAH solid was loaded into either a glass capillary tube (length = 11 mm; inner diameter = 1.2 mm) or a brass cup (depth = 6 mm; inner diameter = 2.5 mm) which was then mounted on the tip of the probe. The probe was inserted perpendicular to the bore axis, with the capillary or cup 58 cm from the center of the magnet. The maximum attainable probe temperature was 170°C.

The PAH cations were generated by electron ionization of the neutral gas-phase molecules. The electron ionization source (Figure 2-3) was located 25.4 cm from the center of the magnet. Electrons were generated by 1.5 A to 2.5 A applied to a rhenium filament (length = 7.5 mm; width = 0.5 mm). Electrons were accelerated towards the

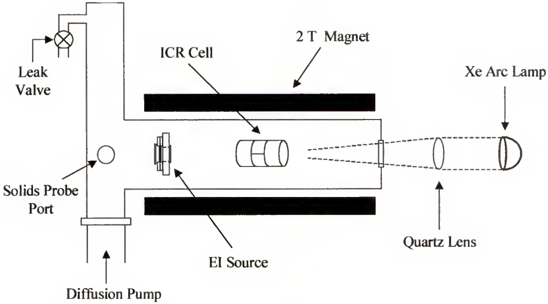

Figure 2-2. General schematic of the ICR experimental apparatus.

center of the magnet by a negative potential applied to a repeller plate 4.0 mm behind the filament. Repeller plate voltages ranged from -15 V to -30 V, yielding electron kinetic energies of 15 eV to 30 eV. Since typical PAH ionization energies are 7 eV to 10 eV, and typical PAH carbon-hydrogen bond energies range from 3 eV to 7 eV, neutral PAHs are ionized and fragmented by electron bombardment.

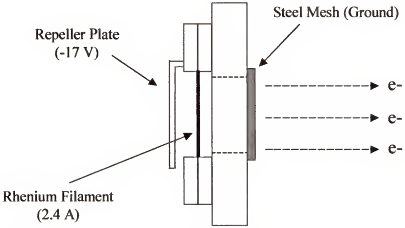

Figure 2-3. Electron ionization source for ionization of gas-phase PAHs.

Ions were trapped in an open-ended cylindrical cell located at the center of the magnetic field (Figure 2-4). The cell consisted of four curved stainless steel plates: two opposing excitation plates and two opposing detection plates. Ions were confined axially to the center of the cell by positive voltages applied to cylindrical trapping plates at the ends of the cell. Typical trapping voltages were +1 V to +2 V. All plates in the cell were electrically isolated by Teflon spacers.

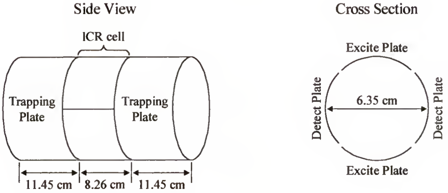

Figure 2-4. Dimensions of the ICR cell comprised of two cylindrical trapping plates, two curved excitation plates, and two curved detection plates.

Ionization Efficiency

In order to determine the relative concentrations of ions and neutrals in the cell during a standard experiment, electron and cation currents were measured under typical ionization conditions. For these measurements, a stainless steel Faraday plate (diameter = 3.81 cm) was temporarily mounted on the end of the cell, 42 cm from the filament. Current was measured with a Keithley 601 electrometer.

Electron concentration and kinetic energy were determined by monitoring the current produced by electrons striking the Faraday plate. Background pressure for these experiments was 1 x 10^{-9} Torr, which corresponds to 3 x 10^{7} molecules/cm^{3}. To simulate normal operating conditions, +1 V was applied to each trapping plate, and the four plates comprising the cell were held at 0 V. For a filament current of 1.7 A and a repeller voltage of -16 V, the electron current measured on the Faraday plate was -5.6 nA. Based on the area of the Faraday plate (11.40 cm^2) and the length of the ICR cell (8.26 cm), the concentration of the electron beam within the cell was 4×10^5 electrons/cm^3 for a standard 10 ms ionization pulse. Electron kinetic energy was measured by applying a negative stopping potential to the Faraday plate. For the above filament conditions, a negative potential of -14.5 V was required to reduce the measured current from -5.6 nA to +25 pA. This measured electron kinetic energy of 14.5 eV correlates well with the 16 eV expected from the repeller plate potential.

Ion current was measured by monitoring acenaphthene cations striking the Faraday plate. Acenaphthene vapor was introduced into the system to a maximum pressure of 4×10^{-7} Torr. Cations produced by electron ionization were directed towards the Faraday plate by decreasing positive voltages applied across the cell assembly: 10 V on the trapping plate closest to the filament, 4 V on the cell plates, and 1 V on the final trapping plate. Voltage applied to the Faraday plate was varied from 0 V to -25 V. Cation currents measured on the Faraday plate at different acenaphthene pressures are presented in Table 2-1. The maximum positive current measured was +100 pA, which corresponds to an ion concentration of 7×10^4 ions/cm^3 for a standard 10 ms ionization pulse. At a normal operating pressure of 1.5×10^{-8} Torr, this ion concentration yields an ion to neutral ratio of 1 to 10^4. Electron-PAH collision efficiency was estimated by comparing the number of electrons and ions striking the Faraday plate during 10 ms. For an electron count of 4×10^7 and an ion count of 6×10^6, collision efficiency was 15%.

Table 2-1. Current (A) measured on the Faraday plate at various acenaphthene pressures (Torr) and applied Faraday plate potentials (V).

	Applied Faraday Plate Potential		
Pressure (Torr)	**0 V**	**-14.5 V**	**- 25 V**
1.0×10^{-9}	-5.0×10^{-9} A	-6.3×10^{-9} A	-4.5×10^{-9} A
1.5×10^{-8}	$+8.4 \times 10^{-11}$ A	$+9.1 \times 10^{-11}$ A	$+8.6 \times 10^{-11}$ A
4.0×10^{-7}	$+1.0 \times 10^{-10}$ A	$+1.0 \times 10^{-10}$ A	$+1.0 \times 10^{-10}$ A

Xenon Arc Lamp

Trapped PAH cations were irradiated by the continuous radiant output of a 300 W collimated xenon arc lamp (ILC Technology, model LX300UV). The spectral distribution of the lamp extended from 250 nm to 1100 nm (Figure 2-5). Based on the minimum wavelength of 250 nm, the maximum single photon energy produced by the lamp was 5 eV. Since PAH ionization requires at least 7 eV, ionization of PAH neutrals during lamp irradiation was insignificant.

According to manufacturer specifications, lamp power was 6.7 W in the ultraviolet and visible regions of the spectrum, and 26.8 W in the infrared region.[56] The estimated photon flux in the UV-visible region was 7×10^{15} photons cm^{-2} nm^{-1} s^{-1}, and the photon flux in the infrared region was 3×10^{16} photons cm^{-2} nm^{-1} s^{-1}. Light emitted by the lamp was focused by a fused silica lens (diameter = 7.5 cm) through a quartz window (diameter = 3.0 cm) into the vacuum chamber (Figure 2-6). The focused spot diameter at the center of the ICR cell was 2.5 cm. Assuming 100% lamp efficiency, the number of UV photons reaching the center of the cell during a standard 1.0 s irradiation time was ~4 x 10^{16} photons nm^{-1}. Irradiation times were regulated by an electronically operated shutter (Uniblitz, model VMM-D1) placed between the lamp and the focusing lens. The mechanical response time of the shutter limited the minimum irradiation time to 0.1 s.

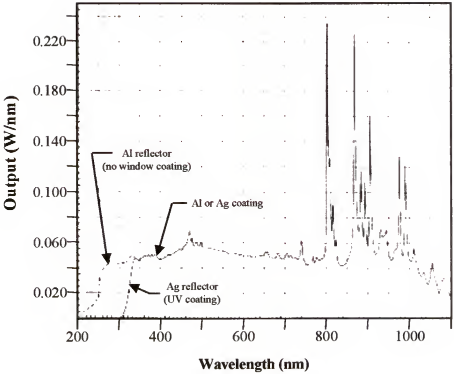

Figure 2-5. Spectral outputs of three xenon arc lamps.[56] The lamp used in these experiments had an Al reflector with no window coating.

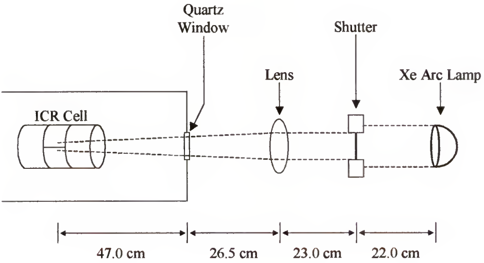

Figure 2-6. Optimal arrangement for focusing light into the center of the ICR cell.

Data Acquisition System

Ion excitation and data collection were controlled by a modular ICR data acquisition system (MIDAS)[57] developed by the National High Field FT-ICR facility at the National High Magnetic Field Laboratory (NHMFL) in Tallahassee, FL. This data system enabled the sequencing of pulsed events and the Fourier transform of time domain ICR signals. Experimental timing was controlled by a digital pattern generator (Interface Technology DG 600VXI). Digital signals were converted to DC voltages and TTL triggers by a homebuilt instrument control module.[57] Excitation waveforms were created by a waveform generator (Tektronix VX4790A) and amplified by a RF power amplifier (ENI 2100L) that provided a gain of ~400. Free ion decay signals were amplified by a LeCroy preamplifier which provided a gain of ~1000 and a bandwidth of 10 kHz to 3 MHz. Following preamplification, the free ion decay time domain signals were acquired by a Hewlett-Packard E1437A digitizer.

Two excitation techniques were applied during ICR experiments: broadband frequency sweep (chirp) excitation and stored-waveform inverse Fourier transform (SWIFT) excitation.[58] Because chirp excitation spans a broad frequency range and requires relatively low applied excitation voltage, chirp waveforms were used to excite ions to a detectable cyclotron radius. Conversely, inverse Fourier transform waveforms create precise, frequency selective excitation windows. Therefore, SWIFT excitation was used for ion ejection and ion isolation. Characteristic frequency domains of chirp excitation, SWIFT ejection, and SWIFT isolation waveforms are shown in Figure 2-7.

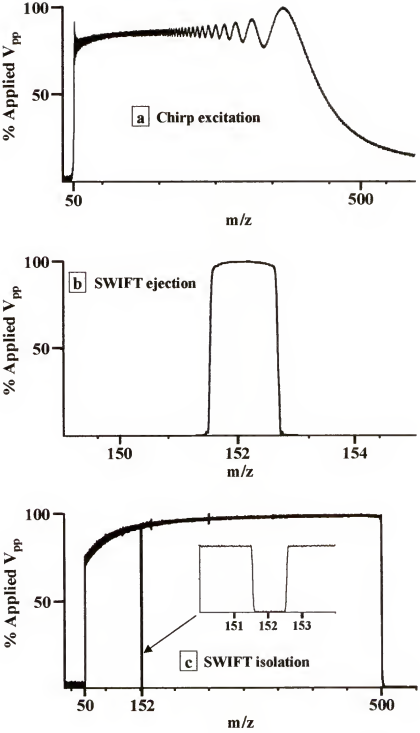

Figure 2-7. Ion excitation waveforms. A) Chirp excitation of ions from m/z 50 to m/z 500. B) SWIFT ejection of the m/z 152 ion. C) SWIFT isolation of the m/z 152 ion.

Standard Experiment

A typical experiment consisted of ionization, isolation, photolysis, excitation, and detection events controlled by the MIDAS system. Prior to electron ionization, ions from previous experiments were removed from the cell by a 20 ms quench pulse. During this quench pulse, a high positive potential (+9.5 V) was applied to one trapping plate, and a high negative potential (-9.5 V) was applied to the second trapping plate. After the quench pulse, trapping voltages were returned to +1 V. Electron pulse lengths were controlled by applying a negative potential (-15 V to -30 V) to the repeller plate for the desired ionization period. After ionization, the repeller plate potential was reduced to -1 V to prevent further ionization during the remainder of the experiment.

Because significant fragmentation occurred during ionization, the parent ion was isolated using a stored waveform inverse Fourier transform (SWIFT)[58] to eject fragment ions and ^{13}C isotope-containing ions. The isolated parent ion was then irradiated for 0.1 s to 10.0 s to create the photoproducts of interest. Photofragmentation pathways were investigated by two methods. In the first method, each fragment ion was isolated with a second SWIFT waveform, and subsequently photolyzed to determine its fragmentation pattern. The second method involved ejection of individual fragment ions during the lamp irradiation steps. An ion ejected from the cell during lamp irradiation cannot absorb UV photons, and thus cannot be the source of any fragment ions.

Prior to detection, ions were excited to a larger cyclotron radius by standard chirp waveforms. Ions were then detected as a decaying image current induced on the opposing detection plates. This time domain ion decay was Fourier transformed to a frequency domain spectrum, which was then converted to the corresponding mass spectrum. All mass spectra presented in this work are the signal-averaged composites of 50 scans.

Matrix Isolation Spectroscopy

To investigate possible carriers of the unidentified infrared emission bands, infrared and UV-visible absorption spectra were collected for PAH neutrals and cations isolated in a solid argon matrix.

Experimental Apparatus

Matrix isolation experiments were conducted in a vacuum chamber pumped to 2 x 10^{-7} Torr by a diffusion pump (Figure 2-8). This chamber was mounted on a moveable plate to allow insertion into both a MIDAC M2000 FT-IR spectrometer and a Nicolet UV-visible spectrophotometer. Barium fluoride windows were mounted on two opposing sides of the chamber to accommodate an IR or UV-visible beam.

The deposition surface was a barium fluoride window (diameter = 2.0 cm) mounted in a copper holder cooled to 12 K by a closed cycle helium cryostat (Displex HC-2, APD Cryogenics Inc.). Barium fluoride is transparent from 67,000 cm^{-1} to 870 cm^{-1}, allowing transmission of both IR and UV-visible radiation. Window temperature was monitored on a 9600-5 Thermocouple temperature controller (Scientific Instruments) via an indium-gold thermocouple attached at the top of the sample holder. The deposition window assembly was surrounded on three sides by a 1.0 mm thick copper thermal shield. The distance between the sides of the holder and the interior of the thermal shield was 3.0 mm. A 2.0 cm diameter hole was cut into the back of the thermal shield to allow passage of the IR and UV-visible beams. The window was aligned with the IR beam to allow collection of IR absorption spectra during matrix deposition.

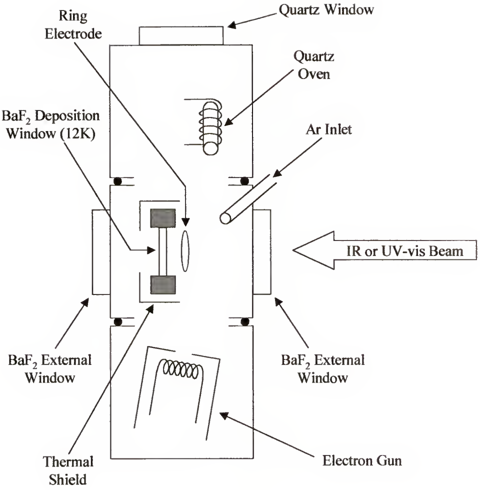

Figure 2-8. Apparatus for matrix isolation experiments.

Argon gas was directed towards the deposition window by a stainless steel tube inserted through the side of the vacuum chamber. The end of the gas inlet was 2.0 cm from the deposition window. Gas flow was controlled through adjustment of a needle valve. For PAH cation experiments, carbon tetrachloride vapor was added to the argon gas as a source of counterions. This gas mixture was 99.7% argon (99.995% purity, Matheson) and 0.3% carbon tetrachloride vapor (Kodak, Spectrograde). Prior to mixing, water vapor was removed from the argon through use of a methanol slush trap (175 K), and the carbon tetrachloride was degassed by traditional freeze-pump-thaw techniques. Solid PAH samples were vaporized in a quartz oven positioned 2.5 cm from the deposition window. The sample oven was heated to ~40°C by 14 W to 17 W applied to copper wire surrounding the oven. The PAH vapor exiting the sample oven was co-condensed with either argon or the argon/CCl_4 gas mixture on the 12 K deposition window.

The gas-phase PAH was ionized by an electron gun located 3.0 cm from the deposition window. A diagram of the electron gun and ionization region is shown in Figure 2-9. The cathode of the electron gun consisted of fifteen spiral loops of tungsten wire (0.1 mm diameter). The anode was a tantalum plate with a 3 mm diameter hole in the center. The distance from anode to cathode was 3.5 mm. Electrons emitted from the heated tungsten wire (11 W) were accelerated through the hole in the tantalum plate by a large negative cathode potential (-140 V to -200 V). The anode was always held at ground potential. The electron beam was further accelerated towards the deposition region by a +90 V potential applied to a copper ring electrode located 5 mm in front of the deposition window. This ring electrode was 1.0 mm thick, with an inner ring diameter of 1.4 cm. Electron current was monitored on a micro-ammeter in line with the ring electrode.

PAH Ionization

Accelerated electrons initiated three PAH ionization mechanisms: Penning ionization, charge transfer, and direct electron bombardment. In Penning ionization, excited argon atoms relax by ionizing PAH neutrals. This ionization process begins with high-energy electrons (~200 eV) striking argon atoms near the electron gun exit aperture.

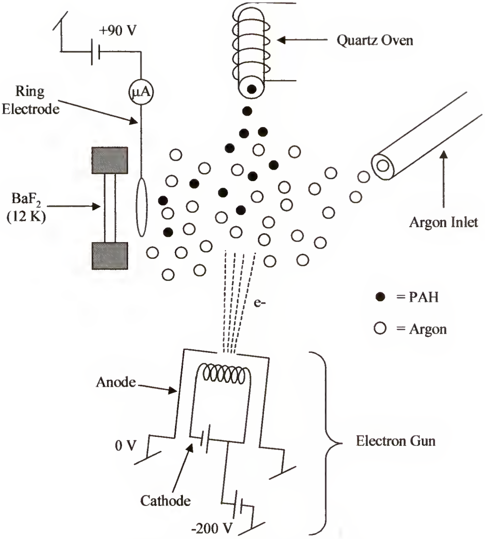

Figure 2-9. Deposition region during matrix isolation experiments.

These high-energy electrons easily ionize the argon atoms (IE = 15.8 eV), yielding two electrons of reduced energy for each argon cation formed. This electron cascade process continues until the electrons no longer have sufficient energy to ionize argon atoms. These low-energy electrons excite argon atoms near the deposition window to metastable states. The excited argon atoms relax during collisions with PAH neutral molecules. Because the energy of the excited argon atoms is greater than the PAH ionization energy (IE = 7 eV to 10 eV), the PAH neutral molecules are ionized during these collisions.

$e^- + Ar \rightarrow Ar^+ + 2e^-$ [electron cascade]

$e^- + Ar \rightarrow Ar^* + e^-$ [argon excitation]

$Ar^* + PAH \rightarrow Ar + PAH^+ + e^-$ [Penning ionization]

Due to the relatively low energy of the excited argon atoms, Penning ionization of PAH neutrals produces very few fragment ions.

Argon cations and high-energy electrons produced during the electron cascade also contribute to PAH ionization. Collision of an argon cation with a PAH neutral results in charge transfer, yielding an argon atom and a PAH cation.

$Ar^+ + PAH \rightarrow Ar + PAH^+$

Electrons striking PAH neutrals directly both ionize and fragment the PAH neutrals.

$e^- + PAH \rightarrow PAH^+$ (or fragments) $+ 2e^-$

Consequently, PAH fragment yield is directly proportional to the energy of electrons exiting the electron gun.

During deposition, the concentration ratio of argon atoms to PAH molecules is approximately 300:1. Due to cryopumping by the 12 K cryostat, the pressure of argon atoms in the deposition region is approximately ten times the overall system pressure. Thus, the major PAH ionization route involves PAHs colliding with ionic and excited argon species rather than direct electron bombardment of PAH neutrals. This proposed route is supported by the direct relationship between argon pressure and PAH cation production.[34] Based on the electron cascade model, excited argon atoms are more prominent in the deposition region than argon cations. Therefore, Penning ionization is the predominant ionization process near the deposition window.

The carbon tetrachloride in the gas mixture both enhances PAH ionization and leads to charge neutrality in the argon matrix.[32] Electron bombardment of carbon tetrachloride molecules yields both CCl_3 cations and chlorine atoms.

$$CCl_4 + e^- \rightarrow CCl_3^+ + Cl + 2e^-$$

The CCl_3 cations can ionize PAH neutrals in charge transfer reactions.

$$CCl_3^+ + PAH \rightarrow CCl_3 + PAH^+$$

Due to the high electron affinity of chlorine, chlorine atoms dissociated from CCl_4 capture low energy electrons to form chlorine anions.

$$Cl + e- \rightarrow Cl^-$$

The negatively charged chlorine ions balance the positively charged PAH and argon cations trapped in the argon matrix. This overall matrix charge neutrality is crucial to PAH cation accumulation in the matrix. The proposed carbon tetrachloride reactions are supported by the appearance of CCl_3^+ and the weakly bound $CCl_3{*}Cl$ complex in the IR spectrum.[32]

Standard Deposition Experiment

Prior to cryostat cooling, the system pressure was 2×10^{-7} Torr. Cooling the cryostat to 12 K reduced the background pressure to 4×10^{-8} Torr. The argon/CCl_4 gas mixture was leaked into the chamber to an operating pressure of 4×10^{-7} Torr. Electrons emitted from the heated cathode (11 W) were accelerated by an applied potential of -140 V to -200 V. The quartz sample oven was heated by 14 W to 17 W depending on the PAH to be vaporized. Deposition times ranged from 2 hr to 4 hr. Because the deposition window was aligned with the IR beam during deposition, vibrational band intensity could be monitored as a function of deposition time.

After deposition, the infrared absorption spectrum (4000 cm^{-1} to 700 cm^{-1}) was collected at 1 cm^{-1} resolution by a MIDAC M2000 FT-IR spectrometer . The cryostat was then inserted into a Nicolet UV-visible spectrophotometer for collection of the electronic absorption spectrum (800 nm to 200 nm). Bandwidth resolution for electronic absorption spectra ranged from 0.28 nm to 0.60 nm.

Vibrational and electronic bands were correlated by matrix annealing and photolysis experiments. The argon matrix was annealed by raising the cryostat temperature to 34 K, creating a fluid matrix environment. During annealing, charged species are free to move throughout the matrix, resulting in the neutralization of trapped cations. For photolysis experiments, the cryostat was rotated 90° to align the deposition window with the exterior quartz window. The matrix was then irradiated with UV light (225 nm to 900 nm) from a 100 W medium pressure mercury lamp. Irradiation of the matrix liberates electrons from the trapped negatively charged species. These free electrons are then captured by the PAH cations, resulting in cation neutralization. Depending on the bond energies of the PAH, UV irradiation can also photofragment trapped neutral and cationic PAHs. After annealing and/or photolysis, infrared and UV-visible spectra were recollected for comparison with spectra from the original, unaltered matrix.

CHAPTER 3
ACENAPHTHENE

Background

Acenaphthene ($C_{12}H_{10}$) is a peri-condensed polycyclic aromatic hydrocarbon (PAH) consisting of an aliphatic five-membered ring fused to two aromatic six-membered rings (Figure 3-1). Although not fully conjugated, acenaphthene is classified as a PAH due to the aromaticity of the naphthalene base structure.

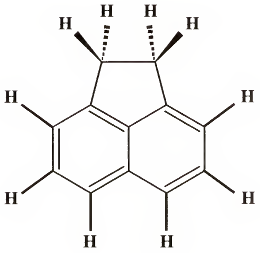

Figure 3-1. Acenaphthene structure.

Astrophysical Relevance

The weak UIR emission bands between 3.3 μm and 3.6 μm are characteristic of aliphatic C-H stretching vibrations. Therefore, sources of these bands may include hydrogenated PAHs with aliphatic components or side-chains.[18] To identify possible carriers of the 3.419 μm aliphatic band, Beegle et al. created molecular aggregates by subjecting PAHs to a high-energy hydrogen plasma.[59,60] The infrared spectrum of the residue produced from a PAH precursor mixture of acenaphthene (25%) and acenaphthylene (75%) correlated well with the emission profile of the IRAS 05341 protoplanetary nebula.[60] The spectrum was also similar to emission features observed by Sloan et al. in the Orion Bar,[61] although relative intensities did not match as well. Nevertheless, acenaphthene is a possible source of the C-H aliphatic stretches observed in the UIR emission bands.

Infrared and Electronic Spectroscopy

The infrared photodissociation spectrum of the gas-phase acenaphthene cation was reported by Oomens et al.[41] Acenaphthene cations were trapped in a Paul-type quadrupole ion trap and irradiated with the pulsed, tunable output (5 μm to 250 μm) of a free electron laser (FEL). Fragmentation was monitored as a function of IR laser wavelength. The observed infrared photodissociation of the acenaphthene cation was limited to the loss of two hydrogens. Because the resolution of the ion trap prevented the removal of dehydrogenated ionization products prior to FEL irradiation, hydrogen loss from the acenaphthene cation was monitored as an increase in the low mass shoulder of the parent ion mass peak. The experimental IR spectrum correlated well with vibrational frequencies calculated at the B3LYP/D95(d,p) level of theory for the acenaphthene cation. The strongest observed bands at 1162 cm^{-1}, 1384 cm^{-1}, and 1492 cm^{-1} were attributed to C-H in-plane bending, symmetric $-CH_2$ scissor, and C-C stretching vibrations, respectively.

The photodehydrogenation of acenaphthene neutral molecules trapped in solid argon has recently been reported.[37] Acenaphthene and argon (1:600) were deposited onto a BaF_2 window at 12 K. Infrared and electronic absorption spectra were collected before and after irradiation of the matrix with the full output of a 100 W Hg lamp. In the IR spectrum, photolysis reduced the 838.6 cm^{-1} and 782.8 cm^{-1} acenaphthene ($C_{12}H_{10}$) bands and produced the 832.4 cm^{-1} and 773.7 cm^{-1} bands previously assigned to acenaphthylene ($C_{12}H_8$). Therefore, photolysis of the matrix isolated acenaphthene removes two hydrogens from the aliphatic pentagonal ring to form acenaphthylene. Band assignments for both acenaphthene and acenaphthylene were confirmed by calculations at the B3LYP/6-31G(d,p) level of theory.

Evidence of hydrogen loss was also observed in the UV-visible absorption spectrum. Photolysis of the matrix reduced the 319.0 nm acenaphthene band and produced new bands at 337.3 nm and 363.0 nm. The 337.3 nm band was previously assigned to the $S_2 \leftarrow S_0$ transition of acenaphthylene ($C_{12}H_8$). The 363.0 nm band was assigned to a singly-dehydrogenated acenaphthene radical fragment ($C_{12}H_9$). Based on time-dependent density functional theory (TDDFT) vertical excitation energy calculations, this fragment was most likely produced by hydrogen abstraction from the pentagonal ring. Thus, UV irradiation of isolated acenaphthene ($C_{12}H_{10}$) yielded both singly and doubly-dehydrogenated photoproducts.

Gas-Phase Photofragmentation

Photofragmentation of the gas-phase acenaphthene cation (m/z 154) was investigated by Ekern et al. via Fourier transform ion cyclotron resonance (FT-ICR) mass spectrometry.[47] Acenaphthene cations were trapped in an ICR cell in a 3 Tesla magnet and irradiated with a UV photon flux of 10^{17} photons cm^{-2} nm^{-1} s^{-1} for 0.5 s. Loss of up to two hydrogens was observed. It was proposed that the acenaphthene cation photodissociates to form the acenaphthylene cation (m/z 152), which was determined to be photostable in similar experiments. However, the mechanism of this double hydrogen loss (sequential or simultaneous) was not investigated. Although it was assumed that the two aliphatic hydrogens in the pentagonal ring were removed, actual fragment structures were not determined.

DFT Calculations

Optimized geometries and fragmentation energies were calculated using the Gaussian 98 platform.[54] Hybrid density functional theory (B3LYP) was applied in conjunction with the 6-31G(d,p) basis set.

Optimized Geometries

Optimized geometries for the neutral and ionic ground states of acenaphthene were calculated with the 6-31G(d,p) basis set. The acenaphthene structure with labeled atom positions is shown in Figure 3-2. Numbered positions correspond to IUPAC numbering conventions. Letter designations are unique to this work.

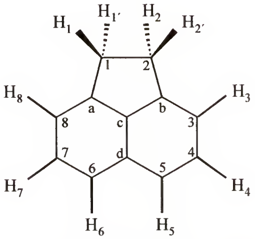

Figure 3-2. Structure and atom position labeling for acenaphthene.

Bond lengths and bond angles are presented in Table 3-1 and Table 3-2, respectively. For the acenaphthene neutral molecule, all hydrogens attached to the sp^2 hybridized carbons of the six-membered rings have a calculated carbon-hydrogen bond length of approximately 1.09 Å. The four hydrogens attached to the sp^3 hybridized carbons (C_1 and C_2) in the five-membered ring have a slightly greater C-H bond length of 1.10 Å. All carbon-carbon bond lengths for the six-membered rings are approximately 1.40 ± 0.02 Å, indicating the delocalized double bond character of the C-C bonds in these rings. For comparison, the C-C bond lengths for a neutral benzene molecule calculated at the B3LYP/6-31G(d,p) level of theory are all 1.397 Å. The C_1-C_2 bond in the five-membered ring has a bond length of 1.57 Å, which is consistent with the expected single bond between the sp^3 hybridized C_1 and C_2. Similarly, the C_a-C_1 and C_2-C_b single bonds in the five-membered ring have bond lengths of 1.52 Å.

Carbon-hydrogen bond lengths in the acenaphthene radical cation are similar to those in the acenaphthene neutral: 1.09 Å for hydrogens on sp^2 hybridized carbons and 1.10 Å for hydrogens on sp^3 hybridized carbons. As in the neutral, all C-C bonds in the six-membered rings are calculated to be 1.40 ± 0.01 Å, indicating the expected π-bond character of the aromatic rings. Upon ionization, the C_a-C_8, C_b-C_3, C_6-C_7, and C_4-C_5 bond lengths all increase by 0.03 Å. The C_8-C_7 and C_3-C_4 bond lengths decrease by 0.03 Å. No significant change in bond lengths is observed for the aliphatic five-membered ring during ionization. Thus, the overall structural effect of acenaphthene ionization is a distortion of the aromatic six-membered rings.

Ionization of PAH molecules involves removal of a π electron from the conjugated π electron network. Although these π electrons are initially delocalized,

Table 3-1. Bond lengths (Å) calculated at the B3LYP/6-31G(d,p) level of theory for neutral and cationic acenaphthene.

Bond	Neutral (Å)	Cation (Å)	Bond	Neutral (Å)	Cation (Å)
C_1-C_2	1.5690	1.5600	C_1-H_1	1.0960	1.0971
C_2-C_b	1.5194	1.5027	C_1-$H_{1'}$	1.0960	1.0971
C_b-C_3	1.3771	1.4092	C_2-H_2	1.0960	1.0971
C_3-C_4	1.4231	1.3972	C_2-$H_{2'}$	1.0960	1.0971
C_4-C_5	1.3828	1.4115	C_3-H_3	1.0867	1.0852
C_5-C_d	1.4220	1.4154	C_4-H_4	1.0866	1.0849
C_d-C_c	1.4142	1.4127	C_5-H_5	1.0868	1.0858
C_c-C_b	1.4119	1.4054	C_6-H_6	1.0868	1.0858
C_a-C_c	1.4119	1.4054	C_7-H_7	1.0866	1.0849
C_d-C_6	1.4220	1.4154	C_8-H_8	1.0867	1.0852
C_6-C_7	1.3828	1.4115			
C_7-C_8	1.4231	1.3972			
C_8-C_a	1.3771	1.4092			
C_a-C_1	1.5194	1.5027			

removal of an electron creates a radical cation with a partially localized, unpaired electron. The most probable location of this unpaired electron can be determined from atomic spin densities. Calculated atomic spin densities for the acenaphthene cation are presented in Table 3-3. In the acenaphthene radical cation, the largest atomic spin density resides on the C_5 and C_6 atoms. An unpaired electron on C_5 or C_6 correlates well with the lengthening of the C_4-C_5 and C_6-C_7 bonds. Similarly, significant spin density is also associated with the C_a and C_b atoms, which explains the lengthening of the C_a-C_8 and C_b-C_3 bonds.

Sequential Hydrogen Loss

Lowest energy pathways for sequential hydrogen loss were constructed based on carbon-hydrogen bond energies. These bond energies were calculated by comparing the

Table 3-2. Bond angles (degrees) calculated at the B3LYP/6-31G(d,p) level of theory for neutral and cationic acenaphthene.

Angle	Neutral	Cation
C_1-C_2-C_b	104.9	104.8
C_2-C_b-C_c	108.8	109.3
C_b-C_c-C_a	112.7	111.8
C_c-C_a-C_1	108.8	109.3
C_a-C_1-C_2	104.9	104.8
C_b-C_3-C_4	118.8	118.7
C_3-C_4-C_5	122.4	122.4
C_4-C_5-C_d	120.1	120.1
C_5-C_d-C_c	116.2	116.3
C_d-C_c-C_b	123.7	124.1
C_c-C_b-C_3	118.8	118.5
C_a-C_c-C_d	123.7	124.1
C_c-C_d-C_6	116.2	116.3
C_d-C_6-C_7	120.1	120.1
C_6-C_7-C_8	122.4	122.4
C_7-C_8-C_a	118.8	118.7
C_8-C_a-C_c	118.8	118.5

Angle	Neutral	Cation
H_1-C_1-$H_{1'}$	106.4	105.6
H_1-C_1-C_2	111.4	112.1
$H_{1'}$-C_1-C_2	111.4	112.1
H_2-C_2-$H_{2'}$	106.4	105.6
H_2-C_2-C_b	111.4	111.1
$H_{2'}$-C_2-C_b	111.4	111.1
H_3-C_3-C_4	119.5	120.1
H_4-C_4-C_5	119.1	118.6
H_5-C_5-C_d	119.7	120.3
H_6-C_6-C_7	120.1	119.7
H_7-C_7-C_8	118.5	119.1
H_8-C_8-C_a	121.7	121.2

corrected ground-state energies of the parent and fragment species (Figure 3-3). Hydrogen removal energies for the acenaphthene neutral and cation were calculated using the 6-31G(d,p) basis set and are presented in Table 3-4. In both cases, the easiest hydrogen to remove is one of the four hydrogens bonded to the sp^3 hybridized carbons (C_1 and C_2) in the pentagonal ring: 3.53 eV for the neutral and 2.67 eV for the cation. All other carbon-hydrogen bond energies were greater than 4.77 eV (35% higher) for the neutral, and greater than 5.03 eV (88% higher) for the cation. This carbon-hydrogen bond energy (2.67 eV) for the acenaphthene cation is similar to the bond energy reported

Table 3-3. Calculated atomic spin densities at the B3LYP/6-31G(d,p) level of theory for the acenaphthene cation.

Atom	Spin Density	Atom	Spin Density
C_1	-0.007700	H_1	0.013944
C_2	-0.007700	$H_{1'}$	0.013944
C_3	0.103771	H_2	0.013938
C_4	-0.016588	$H_{2'}$	0.013946
C_5	0.303908	H_3	-0.005268
C_6	0.303907	H_4	-0.000586
C_7	-0.016587	H_5	-0.011933
C_8	0.103770	H_6	-0.011933
C_a	0.189020	H_7	-0.000586
C_b	0.189020	H_8	-0.005286
C_c	-0.055545		
C_d	-0.109472		

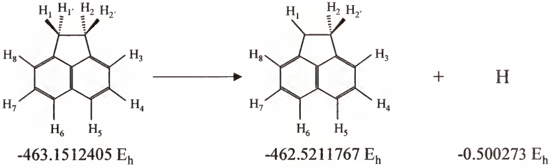

C_1-$H_{1'}$ Bond Energy = 0.129791 E_h = 3.53 eV

Figure 3-3. Calculation of the energy (eV) required to abstract $H_{1'}$ from neutral acenaphthene.

for hydrogens attached to the sp^3 carbon in the fluorene cation (2.64 eV).[53] The difference in the neutral and cationic C-H bond energies can be attributed to the higher stability of the closed-shell (no unpaired electrons) configuration of the neutral versus the lower stability of the open-shell (unpaired electron) configuration of the radical cation. Removing a hydrogen atom from the open-shell cation returns it to a more favorable closed-shell system; therefore, C-H bond energies are lower in the open-shell cation than in the closed-shell neutral.

Table 3-4. Carbon-hydrogen bond energies (eV) calculated at the B3LYP/6-31G(d,p) level of theory for neutral and cationic acenaphthene.

	H_1	$H_{1'}$	H_2	$H_{2'}$	H_3	H_4	H_5	H_6	H_7	H_8
Neutral	3.53	3.53	3.53	3.53	5.18	4.77	4.81	4.81	4.77	5.18
Cation	2.67	2.67	2.67	2.67	5.03	5.06	5.13	5.13	5.06	5.03

Energies for hydrogen removal from the acenaphthene cation and subsequent fragment ions are listed in Figure 3-4. The complete sequential hydrogen loss pathway is depicted in Figure 3-5. After removal of the first hydrogen ($H_{1'}$) from the five-membered ring to form the m/z 153 fragment ion, abstraction of one of the two hydrogens (H_2 or $H_{2'}$) from the other sp^3 hybridized carbon in the five-membered ring requires 3.21 eV. All other carbon-hydrogen bond energies in the m/z 153 fragment ion are at least 51% higher (4.85 eV to 5.02 eV).

For the m/z 152 cation, carbon-hydrogen bond energies in the five-membered ring (6.57 eV) are 38% higher than those in the six-membered ring (4.77 eV to 5.10 eV). However, because the C-H bond energies in the six-membered ring differ by only 6.9%, each of the three hydrogens in the six-membered ring have an equal probability of removal. The resulting three possible structures for the m/z 151 ion will be identified as 151a, 151b, and 151c. In each case, the lowest C-H bond energy in the m/z 151 ion corresponds to the hydrogen(s) adjacent to the hydrogen removed from the m/z 152 ion. After removal of H_3 (4.77 eV) from the m/z 152 ion to form 151a, H_4 requires 4.09 eV

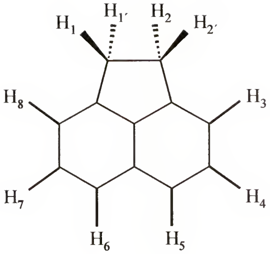

	H removed									
	H_1	$H_{1'}$	H_2	$H_{2'}$	H_3	H_4	H_5	H_6	H_7	H_8
154	2.67	**2.67**	2.67	2.67	5.03	5.06	5.13	5.13	5.06	5.03
153 ($H_{1'}$)	5.02		3.21	**3.21**	4.87	4.89	4.92	4.85	4.91	4.91
152 ($H_{1'}$, $H_{2'}$)	6.57		6.57		**4.77**	**5.10**	**5.06**	5.06	5.10	4.77
151a ($H_{1'}$, $H_{2'}$, H_3)	5.14		5.14			**4.09**	4.82	4.93	4.92	4.84
151b ($H_{1'}$, $H_{2'}$, H_4)	4.97		5.10		**3.75**		**3.69**	4.73	4.70	4.58
151c ($H_{1'}$, $H_{2'}$, H_5)	5.06		5.04		4.53	**3.74**		4.85	4.78	4.64
150a ($H_{1'}$, $H_{2'}$, H_3, H_4)	5.37		5.33				**4.17**	5.05	5.05	4.74
150b ($H_{1'}$, $H_{2'}$, H_4, H_5)	5.21		5.43		**4.23**			5.11	5.05	4.83
149 ($H_{1'}$, $H_{2'}$, H_3, H_4, H_5)	5.11		5.16					4.96	4.92	4.88

Figure 3-4. Carbon-hydrogen bond energies (eV) calculated at the B3LYP/6-31G(d,p) level of theory for sequential hydrogen loss from the acenaphthene cation ($C_{12}H_{10}^+$, m/z 154).

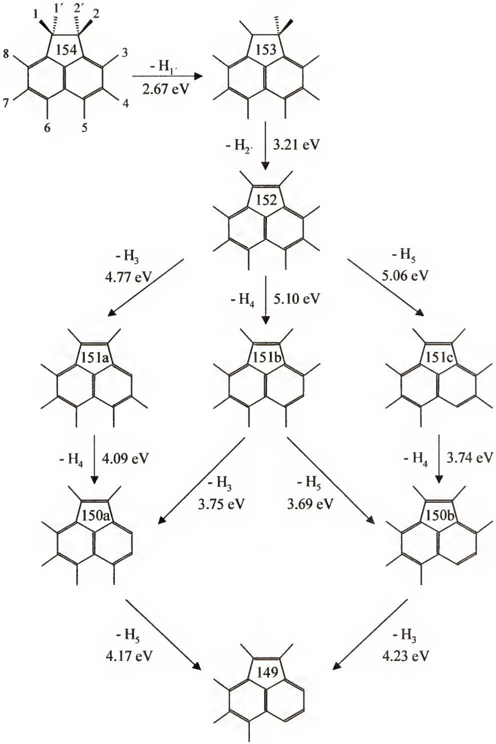

Figure 3-5. Calculated sequential hydrogen loss pathway for the acenaphthene cation ($C_{12}H_{10}^+$, m/z 154).

for abstraction. After removal of H_5 (5.06 eV) from the m/z 152 ion to form 151c, H_4 requires 3.74 eV for removal. All other C-H bond energies in these m/z 151 cations are at least 18% higher: 4.82 eV to 5.14 eV for 151a, and 4.53 eV to 5.06 eV for 151c. After removal of H_4 from the m/z 152 ion to form 151b, the two adjacent hydrogens, H_3 and H_5, have C-H bond energies of 3.75 eV and 3.69 eV, respectively. All other C-H bond energies in the 151b ion are at least 22% higher (4.58 eV to 5.10 eV).

The four probable hydrogen abstraction routes for the m/z 151 cations yield two possible structures for the m/z 150 ion: 150a and 150b. In each case, the remaining hydrogen on the partially stripped six-membered ring is the easiest hydrogen to remove. For the150a ion, H_5 requires 4.17 eV for abstraction; for the 150b ion, H_3 requires 4.23 eV for removal. All other C-H bond energies are at least 14% higher (4.74 eV to 5.43 eV). The two pathways for dehydrogenation of the m/z 150 ion thus lead to the same structure for the m/z 149 ion, in which one of the six-membered rings is completely dehydrogenated.

Carbon-hydrogen bond energies in the m/z 149 ion ranged from 4.88 eV to 5.16 eV, with those in the six-membered ring being slightly lower than those in the five-membered ring. Because the m/z 149 ion was not experimentally observed in photodissociation experiments, further dehydrogenation pathways were not calculated.

FT-ICR Photodissociation Studies

Experimental Conditions

The vapor pressure of acenaphthene (154 amu) was high enough for introduction via a leak valve. Background pressure for these experiments was 1 x 10^{-9} Torr. Acenaphthene vapor was leaked into the system to an operating pressure of 1.1 x 10^{-8}

Torr, which corresponds to approximately 3 x 10^8 acenaphthene molecules/cm^3. Gas-phase acenaphthene was ionized by electron impact. The ionization energy of acenaphthene is 7.7 eV. The optimal filament current for electron generation was 2.4 A. Electrons were accelerated towards the cell during the 20 ms ionization pulse by a repeller plate voltage of -17 V.

Results and Discussion

Electron ionization of gas-phase PAH neutrals yielded both the PAH parent cation and fragment ions. Since the bombarding electron kinetic energy (17 eV) was much greater than the maximum available photon energy (~5 eV), electron impact fragmentation was typically more extensive than photolysis fragmentation. Thus, electron impact fragmentation patterns served as a guide for identifying possible photofragmentation products. Electron bombardment of acenaphthene (Figure 3-6) yielded the m/z 154 parent ion, ^{13}C isotope ions (m/z 155, m/z 156), and dehydrogenated fragment ions (m/z 149-153).

Prior to lamp irradiation, the m/z 154 parent ion was isolated using a SWIFT waveform. Irradiation of the isolated m/z 154 ion with light from the xenon arc lamp (250 nm to 1100 nm) for 1 s to 10 s yielded loss of up to four hydrogens. The relative abundances of the acenaphthene parent and fragment ions (m/z 154, 153, 152, 151, and 150) as a function of irradiation time are shown in Figure 3-7. The abundance of the m/z 154 parent ion rapidly decreased to 15% abundance during 2.8 s of irradiation. The abundance of m/z 153 initially increased proportionately with m/z 154 loss, indicating formation of the m/z 153 fragment ion via single hydrogen loss from the m/z 154 ion. The m/z 153 ion reached a maximum relative abundance of 45% at 1.3 s of lamp

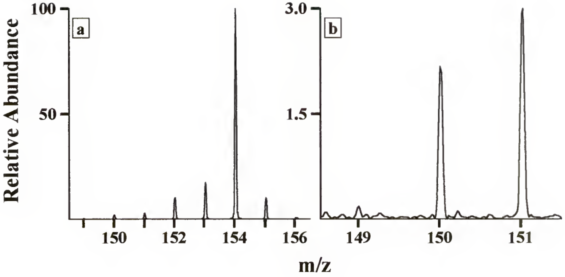

$$\text{acenaphthene} \xrightarrow{\text{e- impact}} \begin{array}{l}156,\ 155,\ 154,\ 153\\ 152,\ 151,\ 150,\ 149\end{array}$$

Figure 3-6. Electron ionization of acenaphthene ($C_{12}H_{10}$). A) FT-ICR mass spectrum in the m/z 149-156 range. B) FT-ICR mass spectrum in the m/z 149-151 range.

irradiation, and decreased with further lamp irradiation. This decrease of the m/z 153 ion was accompanied by an increase in the abundances of the m/z 151 and m/z 150 ions. Production of the m/z 151 and m/z 150 ions most likely involved dehydrogenation of the m/z 153 fragment ion. The initial increase of the m/z 152 ion was slower than the m/z 153 increase; however, after 2.3 s of lamp irradiation, the m/z 152 ion was the most abundant ion in the mass spectrum. The relative abundance of the m/z 152 ion reached a maximum of 60% at 5.5 s of irradiation time. Unlike the m/z 153 ion, no decrease was observed for the m/z 152 ion abundance with further lamp irradiation, indicating that the m/z 152 ion may be photostable.

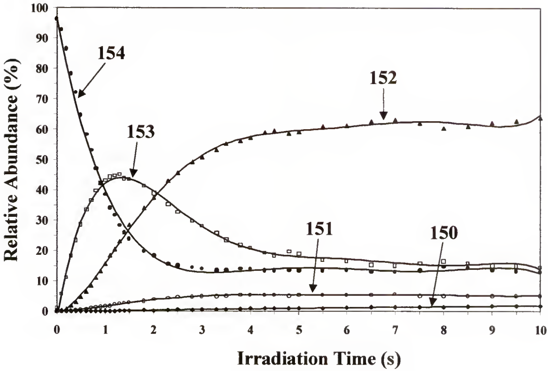

Figure 3-7. Relative abundance (%) of the m/z 154 parent ion and the m/z 153, 152, 151, and 150 fragment ions as a function of irradiation time (s).

During lamp irradiation, the m/z 154 parent ion lost a maximum of four hydrogen atoms. To distinguish between single and double hydrogen loss pathways, SWIFT ejection waveforms were applied during lamp irradiation. Ejection of a specific ion during lamp irradiation prevented the appearance of its corresponding photoproducts in the final mass spectrum. Therefore, SWIFT ejections allowed correlation between fragment ions. Ejection of the m/z 153 ion during 1.5 s lamp irradiation resulted in a 93% reduction of m/z 152, and elimination of the m/z 150 and m/z 151 ions (Figures 3-8 and 3-9). Thus, the predominant pathway for the formation of m/z 152 is single hydrogen loss from m/z 153. Ejection of m/z 152, however, had no effect on the m/z 151 or m/z 150 ions, indicating these ions are not formed via hydrogen loss from the m/z 152

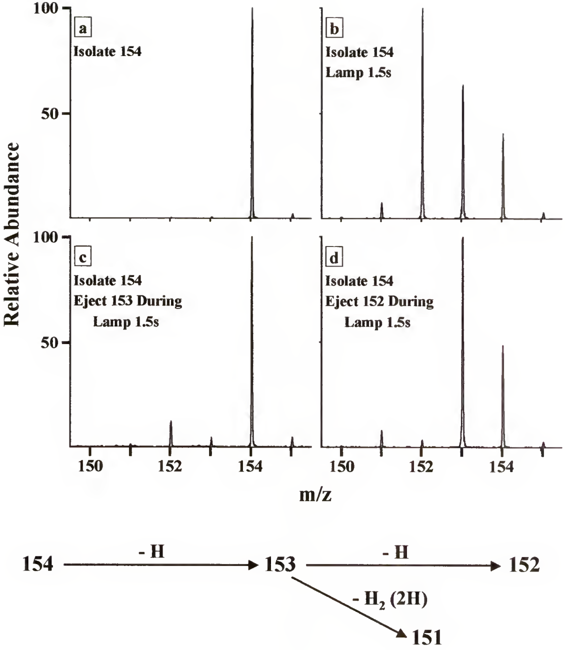

Figure 3-8. Dehydrogenation pathway for the acenaphthene m/z 154 parent ion (m/z 150-155 range). A) FT-ICR mass spectrum of isolated m/z 154. B) FT-ICR mass spectrum after Xe lamp irradiation (1.5 s) of isolated m/z 154. C) FT-ICR mass spectrum after Xe lamp irradiation (1.5 s) with simultaneous ejection of m/z 153. D) FT-ICR mass spectrum after Xe lamp irradiation (1.5 s) with simultaneous ejection of m/z 152.

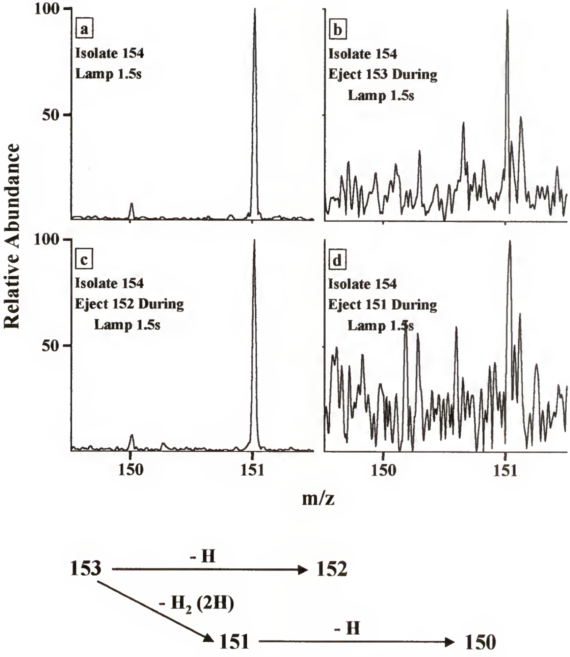

Figure 3-9. Dehydrogenation pathway for the acenaphthene m/z 154 parent ion (m/z 150-151 range). A) FT-ICR mass spectrum after Xe lamp irradiation (1.5 s) of isolated m/z 154. B) FT-ICR mass spectrum after Xe lamp irradiation (1.5 s) with simultaneous ejection of m/z 153. C) FT-ICR mass spectrum after Xe lamp irradiation (1.5 s) with simultaneous ejection of m/z 152. D) FT-ICR mass spectrum after Xe lamp irradiation (1.5 s) with simultaneous ejection of m/z 151.

ion. Consequently, the pathway for m/z 151 formation must involve double hydrogen loss from m/z 153 rather than single hydrogen loss from m/z 152. Ejection of m/z 151 during lamp irradiation eliminated the m/z 150 ion, indicating that m/z 150 is formed via single hydrogen loss from m/z 151.

Isolation and subsequent photolysis of the m/z 153 ion for 5.0 s yielded the m/z 152, 151, and 150 ions (Figure 3-10). Relative abundances of the m/z 152, 151, and 150 ions matched those observed after irradiating the isolated m/z 154 ion for 5.0 s. Ejection of m/z 152 during photolysis for 5.0 s yielded no significant reduction of m/z 151 or m/z 150, confirming that m/z 151 is formed by double hydrogen loss from m/z 153, not single hydrogen loss from m/z 152. Ejection of the m/z 151 ion during photolysis for 5.0 s eliminated the m/z 150 ion, confirming that m/z 150 is formed via single hydrogen loss from m/z 151. Sufficient isolation of the m/z 152 fragment ion was unattainable due to the large relative abundances of the m/z 154 and m/z 153 ions. As such, photolysis products of the m/z 152 ion remained ambiguous. The abundances of the m/z 151 and m/z 150 ions obtained by lamp photolysis were too small to allow subsequent isolation and photolysis.

The complete photofragmentation route for the acenaphthene cation is depicted in Figure 3-11. Percentages represent relative importance in cases where multiple pathways are available for photodissociation. Irradiation of the m/z 154 parent ion yielded single hydrogen loss to form the m/z 153 fragment ion. The m/z 153 fragment ion photodissociated further to form m/z 152 via single hydrogen loss (92.9% yield) and m/z 151 via double hydrogen loss (7.1% yield). The m/z 152 ion appeared to be photostable.

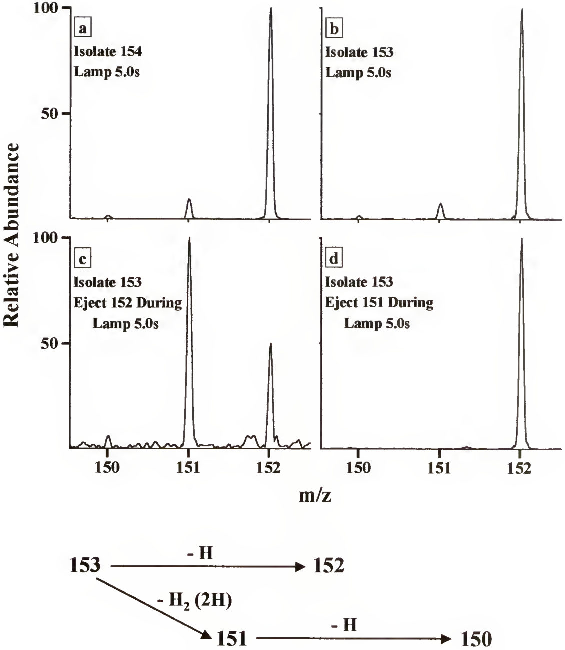

Figure 3-10. Dehydrogenation pathway for the m/z 153 fragment ion (m/z 150-152 range). A) FT-ICR mass spectrum after Xe lamp irradiation (5.0 s) of isolated m/z 154. B) FT-ICR mass spectrum after Xe lamp irradiation (5.0 s) of isolated m/z 153. C) FT-ICR mass spectrum after Xe lamp irradiation (5.0 s) of m/z 153 with simultaneous ejection of m/z 152. D) FT-ICR mass spectrum after Xe lamp irradiation (5.0 s) of m/z 153 with simultaneous ejection of m/z 151.

The m/z 151 ion underwent single hydrogen loss to form m/z 150. No fragments lower than m/z 150 were observed in the mass spectrum.

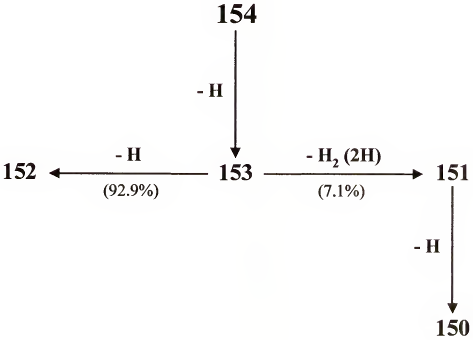

Figure 3-11. Overall observed photodissociation pathway for the acenaphthene cation (m/z 154). Percentages represent relative pathway importance.

Comparison of Observed and Predicted Dissociation Pathways

The observed photodissociation pathway for the m/z 154 parent ion was single hydrogen loss to form the m/z 153 fragment ion. Based on theoretical bond energy calculations, the removal of this first hydrogen from the five-membered ring requires 2.67 eV. The major pathway for photodissociation of the m/z 153 fragment ion was single hydrogen loss to form the m/z 152 fragment ion (92.9% yield). Removal of this second hydrogen from the five-membered ring requires 3.21 eV. Single hydrogen loss from the m/z 152 fragment ion to form m/z 151, however, was not observed as a photodissociation pathway, which correlates well with the high predicted energy (~5 eV) required for this fragmentation route. Thus, the observed double hydrogen loss to form the m/z 151 ion (7.1% yield) must be more energetically favorable than single hydrogen loss.

Unfortunately, methods for calculation of simultaneous hydrogen loss are quite complex and were not performed in this work. Nevertheless, double hydrogen loss from the m/z 153 cation most likely begins with the removal of $H_{2'}$ (3.21 eV) from the five-membered ring. If this double hydrogen loss involves formation of an H_2 molecule, the two hydrogens removed must be near one another on the PAH structure. Since simultaneous loss of two hydrogens from the same carbon is unlikely, the hydrogen removed simultaneously with $H_{2'}$ is either H_1 or H_3. The $H_{2'}$ and H_3 atoms are attached to non-adjacent carbons in different rings, whereas $H_{2'}$ and H_1 are attached to adjacent carbons in the same ring. However, based on the calculated bond lengths and angles in the m/z 153 cation, the estimated distance between $H_{2'}$ and H_3 (3.0 Å) is not much greater than the estimated distance between $H_{2'}$ and H_1 (2.5 Å). Furthermore, because the carbon-hydrogen bond energy of H_1 (5.02 eV) in the m/z 153 cation is 3.0% greater than the carbon-hydrogen bond energy of H_3 (4.87 eV), double hydrogen loss may occur as removal of $H_{2'}$ and H_3.

Formation of the m/z 150 ion occurred via single hydrogen loss from the m/z 151 ion. If the $H_{2'}$ and H_3 atoms are removed from the m/z 153 fragment ion to form the m/z 151 ion, the removal of H_4 to form the m/z 150 ion requires 3.74 eV. This low carbon-hydrogen bond energy correlates well with the observed abundance of the m/z 150 ion in the mass spectrum.

CHAPTER 4
ACENAPHTHYLENE

Background

Acenaphthylene ($C_{12}H_8$) is a peri-condensed polycyclic aromatic hydrocarbon (PAH) consisting of a conjugated five-membered ring fused to two aromatic six-membered rings (Figure 4-1). If viewed as a 12-π-electron system, acenaphthylene does not fit the conventional $4n + 2$ rule for aromaticity. However, acenaphthylene can be classified as aromatic in terms of a 2-π-electron etheno system connected to a 10-π-electron naphthalene molecule.[62]

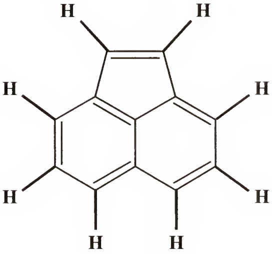

Figure 4-1. Acenaphthylene structure.

Astrophysical Relevance

Acenaphthylene is considered a keystone molecule in the formation of larger PAHs in Keller's interstellar PAH condensation model.[15] According to this model, acetylene (C_2H_2) molecules combine to form naphthalene ($C_{10}H_8$), which then serves as a base for larger PAHs. The next step in the proposed condensation mechanism is addition of an acetylene molecule to naphthalene to form acenaphthylene ($C_{12}H_8$).

Infrared and Electronic Spectroscopy

Infrared and electronic spectra have been reported for acenaphthylene cations trapped in solid argon.[37] Acenaphthylene cations formed by electron ionization were codeposited with argon and CCl_4 on a BaF_2 window at 12 K. Acenaphthylene cation bands were identified through photolysis experiments and comparison to harmonic frequencies calculated at the B3LYP/6-31G(d) and BP86/6-31G(d) levels of theory. The most intense acenaphthylene cation bands were the C-H out-of-plane bending mode at 853.8 cm^{-1} and the C-H in-plane bending mode at 1187.1 cm^{-1}. Due to the low concentration and predicted oscillator strength of the acenaphthylene cation, no acenaphthylene cation bands were observed in the electronic spectrum.

Several bands in the IR absorption spectrum collected after electron bombardment of the acenaphthylene/argon/CCl_4 mixture were not assignable to neutral or cationic acenaphthylene. Bands appearing at 832.4 cm^{-1} and 773.7 cm^{-1} were assigned to neutral acenaphthene ($C_{12}H_{10}$) based on IR absorption spectra previously collected for acenaphthene in solid argon. Bands at 801.5 cm^{-1} and 764.7 cm^{-1} were assigned to a singly-hydrogenated acenaphthylene neutral radical ($C_{12}H_9$) based on calculated frequencies (B3LYP/6-31G(d,p)). Because electron bombardment of acenaphthylene generates atomic hydrogen, the observed $C_{12}H_9$ and $C_{12}H_{10}$ species were likely due to reactions between atomic hydrogen and acenaphthylene on the matrix surface. Such PAH hydrogenation was calculated to be exothermic by Bauschlicher.[26] Bands assignable to the acenaphthene cation ($C_{12}H_{10}^+$) were observed in the electronic spectrum collected after electron bombardment of the acenaphthylene/argon/CCl_4 gas mixture. These acenaphthene cations were formed either by double-hydrogenation of acenaphthylene cations or by ionization of doubly-hydrogenated acenaphthylene neutral. Thus, the hydrogenation of both neutral and cationic acenaphthylene is likely in environments with available atomic hydrogen.

The infrared photodissociation spectrum of the gas-phase acenaphthylene cation has recently been reported.[37] Acenaphthylene cations were isolated in a Paul-type quadrupole ion trap, and irradiated with the pulsed, tunable output (5 μm to 250 μm) of a free electron laser (FEL). Fragmentation was monitored as a function of IR laser wavelength. Infrared photodissociation of the acenaphthylene cation (m/z 152) yielded loss of two hydrogens. Due to the limited resolution of the ion trap and mass spectrometer, the appearance of the m/z 150 ion was monitored as an increase in the low mass shoulder of the parent ion. The strongest bands in the photodissociation spectrum were observed at 1063 cm^{-1}, 1183 cm^{-1}, 1228 cm^{-1}, 1324 cm^{-1}, and 1566 cm^{-1}. Although several of these bands are close to the UIR emission features, the strong band at 1063 cm^{-1} (9.4 μm) does not appear in the UIR emission spectrum. Thus, the acenaphthylene cation was not considered to be a major contributor to the UIR emission bands.

Gas-Phase Photofragmentation

In FT-ICR photodissociation experiments conducted by Ekern et al, the acenaphthylene cation ($C_{12}H_8^+$, m/z 152) was classified as photostable.[47] No hydrogen or carbon loss was observed after irradiation of trapped gas-phase acenaphthylene cations with a UV photon flux of 10^{17} photons cm^{-2} nm^{-1} s^{-1} for 0.5 s. The m/z 152 ion was observed as a stable photoproduct of the phenanthrene ($C_{14}H_{10}$), anthracene ($C_{14}H_{10}$), and acenaphthene ($C_{12}H_{10}$) cations; however, the structure of the m/z 152 fragment ion was not investigated. Based on the structural similarities of the acenaphthene and acenaphthylene cations, the m/z 152 ion produced during hydrogen loss from the acenaphthene cation (m/z 154) was assumed to be the acenaphthylene cation (m/z 152). However, for phenanthrene and anthracene, significant isomerization would be required for the m/z 152 fragment ion to be acenaphthylene.

In photoion mass spectrometric experiments conducted by Jochims et al., acenaphthylene exhibited high photostability.[51] Acenaphthylene molecules inside a quadrupole mass spectrometer were irradiated with synchrotron radiation (7 eV to 35 eV) from an electron storage ring. Radiation wavelength was selected by a monochromator. The ionization energy for acenaphthylene was determined to be 7.74 eV based on the appearance of the m/z 152 cation in the mass spectrum. The m/z 151 fragment ion corresponding to single hydrogen loss was observed at 16.12 eV. The internal energy of the acenaphthylene cation at the threshold of fragmentation was calculated to be 8.54 eV based on the ionization energy of the acenaphthylene parent ion, appearance energy of the m/z 151 fragment ion, and average thermal energy of the parent ion (0.16 eV). The high energy required for fragmentation suggested the acenaphthylene cation would be photostable in the interstellar medium.

DFT Calculations

Optimized geometries and fragmentation energies were calculated using the Gaussian 98 platform.[54] Hybrid density functional theory (B3LYP) was applied in conjunction with the 6-31G(d,p) basis set.

Optimized Geometries

Optimized geometries for the neutral and ionic ground states of acenaphthylene were calculated with the 6-31G(d,p) basis set. The acenaphthylene structure with labeled atom positions is shown in Figure 4-2. Numbered positions correspond to IUPAC numbering conventions. Letter designations are unique to this work.

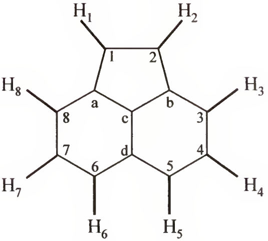

Figure 4-2. Structure and atom position labeling for acenaphthylene.

Bond lengths and bond angles are presented in Table 4-1 and Table 4-2, respectively. For the acenaphthylene neutral molecule, all calculated carbon-hydrogen bond lengths are approximately 1.09 Å. All carbon-carbon bond lengths for the six-membered rings are approximately 1.40 ± 0.02 Å, indicating the delocalized double bond character of the C-C bonds in these rings. The C_1-C_2 bond in the five-membered ring has a bond length of 1.36 Å, as expected for a C-C double bond. The C_a-C_1 and C_2-C_b bonds in the five-membered ring have bond lengths of 1.47 Å, indicating a lack of π character. Thus, these bonds do not participate in the π-conjugated, aromatic network.

All carbon-hydrogen bond lengths in the acenaphthylene radical cation are approximately 1.09 Å. The C-C bonds in the six-membered rings are calculated to be

Table 4-1. Bond lengths (Å) calculated at the B3LYP/6-31G(d,p) level of theory for neutral and cationic acenaphthylene neutral.

Bond	Neutral (Å)	Cation (Å)	Bond	Neutral (Å)	Cation (Å)
C_1-C_2	1.5690	1.5600	C_1-H_1	1.0960	1.0971
C_2-C_b	1.5194	1.5027	C_1-$H_{1'}$	1.0960	1.0971
C_b-C_3	1.3771	1.4092	C_2-H_2	1.0960	1.0971
C_3-C_4	1.4231	1.3972	C_2-$H_{2'}$	1.0960	1.0971
C_4-C_5	1.3828	1.4115	C_3-H_3	1.0867	1.0852
C_5-C_d	1.4220	1.4154	C_4-H_4	1.0866	1.0849
C_d-C_c	1.4142	1.4127	C_5-H_5	1.0868	1.0858
C_c-C_b	1.4119	1.4054	C_6-H_6	1.0868	1.0858
C_a-C_c	1.4119	1.4054	C_7-H_7	1.0866	1.0849
C_d-C_6	1.4220	1.4154	C_8-H_8	1.0867	1.0852
C_6-C_7	1.3828	1.4115			
C_7-C_8	1.4231	1.3972			
C_8-C_a	1.3771	1.4092			
C_a-C_1	1.5194	1.5027			

1.41 ± 0.02 Å, indicating the expected π-bond character of the aromatic rings. Upon ionization, the C_1-C_2 bond length in the five-membered ring increases by 0.07 Å. The C_a-C_1 and C_b-C_2 bond lengths both decrease by 0.05 Å. No significant change is observed for bond lengths in the six-membered rings. Thus, the overall structural effect of acenaphthylene ionization is a distortion of the pentagonal ring.

Calculated atomic spin densities for the acenaphthylene radical cation are presented in Table 4-3. The largest atomic spin density resides on the C_c atom, which is the only carbon atom common to all three rings. Significant spin density also resides on the C_1 and C_2 atoms in the five-membered ring. This partially localized spin density correlates well with the calculated structural distortion of the five-membered ring.

Table 4-2. Bond angles (degrees) calculated at the B3LYP/6-31G(d,p) level of theory for neutral and cationic acenaphthylene.

Angle	Neutral	Cation
C_1-C_2-C_b	104.9	104.8
C_2-C_b-C_c	108.8	109.3
C_b-C_c-C_a	112.7	111.8
C_c-C_a-C_1	108.8	109.3
C_a-C_1-C_2	104.9	104.8
C_b-C_3-C_4	118.8	118.7
C_3-C_4-C_5	122.4	122.4
C_4-C_5-C_d	120.1	120.1
C_5-C_d-C_c	116.2	116.3
C_d-C_c-C_b	123.7	124.1
C_c-C_b-C_3	118.8	118.5
C_a-C_c-C_d	123.7	124.1
C_c-C_d-C_6	116.2	116.3
C_d-C_6-C_7	120.1	120.1
C_6-C_7-C_8	122.4	122.4
C_7-C_8-C_a	118.8	118.7
C_8-C_a-C_c	118.8	118.5

Angle	Neutral	Cation
H_1-C_1-$H_{1'}$	106.4	105.6
H_1-C_1-C_2	111.4	112.1
$H_{1'}$-C_1-C_2	111.4	112.1
H_2-C_2-$H_{2'}$	106.4	105.6
H_2-C_2-C_b	111.4	111.1
$H_{2'}$-C_2-C_b	111.4	111.1
H_3-C_3-C_4	119.5	120.1
H_4-C_4-C_5	119.1	118.6
H_5-C_5-C_d	119.7	120.3
H_6-C_6-C_7	120.1	119.7
H_7-C_7-C_8	118.5	119.1
H_8-C_8-C_a	121.7	121.2

Sequential Hydrogen Loss

Hydrogen removal energies for the acenaphthylene neutral and cation were calculated using the 6-31G(d,p) basis set and are presented in Table 4-3. For the acenaphthylene neutral, all carbon-hydrogen bond energies differ by only 4%; consequently, all hydrogens are equally likely to be removed. In the acenaphthylene cation, C-H bond energies in the six-membered rings are 11% lower than C-H bond energies in the five-membered ring. However, the C-H bond energies in the six-membered rings differ by only 6%. Thus, all hydrogens attached to the six-membered rings in the acenaphthylene cation are equally likely to be removed.

Table 4-3. Atomic spin densities calculated at the B3LYP/6-31G(d,p) level of theory for the acenaphthylene radical cation.

Atom	Spin Density	Atom	Spin Density
C_1	-0.007700	H_1	0.013944
C_2	-0.007700	$H_{1'}$	0.013944
C_3	0.103771	H_2	0.013938
C_4	-0.016588	$H_{2'}$	0.013946
C_5	0.303908	H_3	-0.005268
C_6	0.303907	H_4	-0.000586
C_7	-0.016587	H_5	-0.011933
C_8	0.103770	H_6	-0.011933
C_a	0.189020	H_7	-0.000586
C_b	0.189020	H_8	-0.005286
C_c	-0.055545		
C_d	-0.109472		

Table 4-4. Carbon-hydrogen bond energies (eV) calculated at the B3LYP/6-31G(d,p) level of theory for neutral and cationic acenaphthylene.

	H_1	H_2	H_3	H_4	H_5	H_6	H_7	H_8
Neutral	4.98	4.98	4.78	4.78	4.81	4.81	4.78	4.78
Cation	5.38	5.38	4.77	5.10	5.06	5.06	5.10	4.77

Energies for hydrogen removal from the acenaphthylene cation (m/z 152) and subsequent fragment ions are equivalent to those calculated for the m/z 152 fragment ion in the acenaphthene cation (m/z 154) dehydrogenation pathway (Chapter 3). The discussion of these hydrogen abstraction pathways will not be repeated here. The sequential hydrogen loss pathway for the acenaphthylene cation is shown in Figure 4-3.

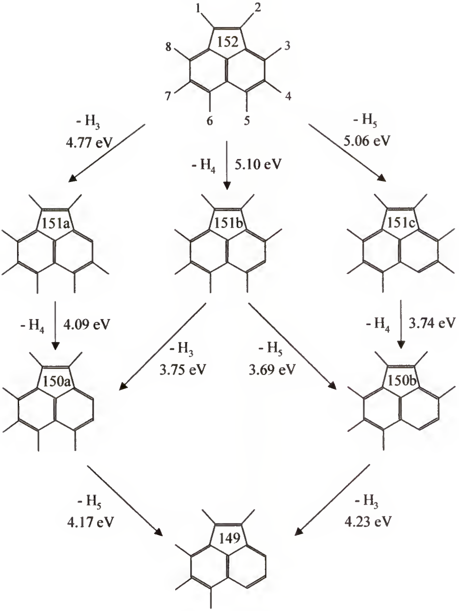

Figure 4-3. Calculated sequential hydrogen loss pathway for the acenaphthylene cation ($C_{12}H_8^+$, m/z 152).

FT-ICR Photodissociation Studies

Experimental Conditions

The vapor pressure of acenaphthylene (152 amu) was high enough for introduction via a leak valve. Background pressure for these experiments was 1 x 10^{-9}

Torr. Acenaphthylene vapor was leaked into the system to operating pressures ranging from 1.5 x 10^{-8} Torr to 1.5 x 10^{-7} Torr, which correspond to 5 x 10^8 to 5 x 10^9 acenaphthylene molecules/cm^3. Gas-phase acenaphthylene was ionized by electron ionization. The ionization energy of acenaphthylene is 8.1 eV. The optimal filament current for electron generation was 2.4 A. Electrons were accelerated towards the cell during the 20 ms ionization pulse by a repeller plate voltage of -17 V.

Results and Discussion

Electron bombardment of the acenaphthylene neutral (Figure 4-4) yielded the m/z 152 parent ion, ^{13}C isotope ions (m/z 153, m/z 154), dehydrogenated fragment ions (m/z 149-151), and several higher mass ions (m/z 300-305). The abundance of these higher mass ions (m/z 300, 301, 302, 303, 304, and 305) increased as a function of delay time between the ionizing electron pulse and the chirp excitation of the ions. These ions in the m/z 300-305 range were assumed to be aggregates produced by reactions between ions and neutral acenaphthylene molecules.

Aggregate formation

To determine the source of each aggregate ion, the m/z 152, m/z 151, and m/z 150 ions were each isolated with a SWIFT waveform and subjected to a reaction delay before chirp excitation (Figure 4-5). To increase overall aggregate abundance, the partial pressure of acenaphthylene was increased to 3.4 x 10^{-8} Torr. Application of a 3.0 s delay to the electron ionization products (m/z 149, 150, 151, 152, 153, and 154) yielded the m/z 300, 301, 302, 303, 304, and 305 aggregate ions. The m/z 303 ion was the most abundant aggregate, with 3.0% abundance relative to the m/z 152 parent ion. Application of a 3.0 s reaction delay to the isolated m/z 152 parent ion produced the m/z 302, 303, 304, and

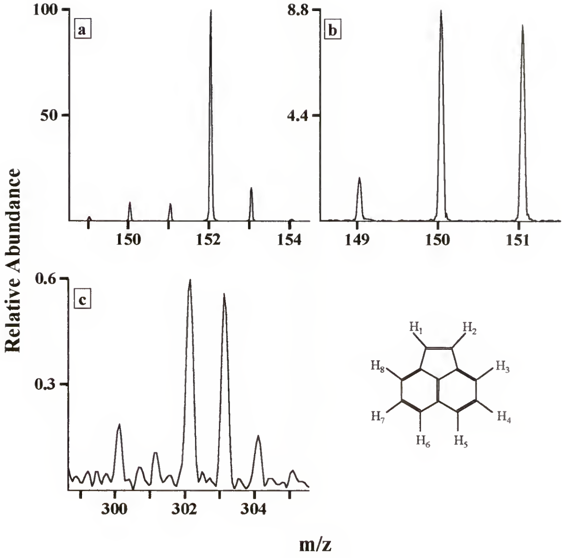

acenaphthylene $\xrightarrow{\text{e- impact}}$ **154, 153, 152, 151, 150, 149**

300, 301, 302, 303, 304, 305

Figure 4-4. Electron ionization of acenaphthylene ($C_{12}H_8$). A) FT-ICR mass spectrum in the m/z 149-154 range. B) FT-ICR mass spectrum in the m/z 149-151 range. C) FT-ICR mass spectrum in the m/z 299-305 range.

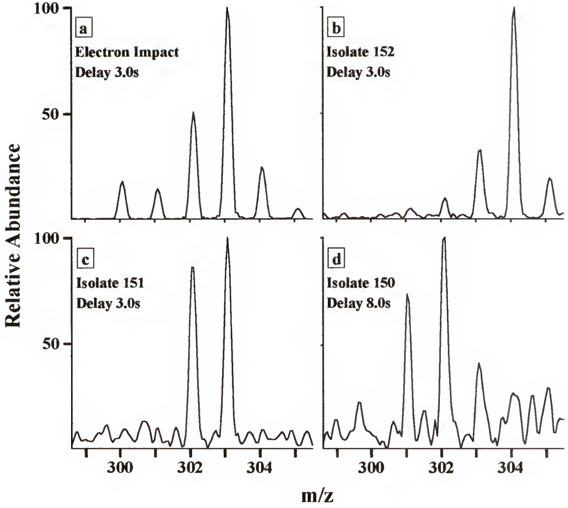

$$152^+ + 152\ n \longrightarrow 304^+ \left(\xrightarrow{-H} 303^+ \right)$$

$$151^+ + 152\ n \longrightarrow 303^+ \left(\xrightarrow{-H} 302^+ \right)$$

$$150^+ + 152\ n \longrightarrow 302^+ \left(\xrightarrow{-H} 301^+ \right)$$

Figure 4-5. Aggregate formation pathways (m/z 299-305 range). The “n” label designates neutral molecules. A) FT-ICR mass spectrum after a 3.0 s delay was applied to the electron impact products. B) FT-ICR mass spectrum after a 3.0 s delay was applied to isolated m/z 152. C) FT-ICR mass spectrum after a 3.0 s delay was applied to isolated m/z 151. D) FT-ICR mass spectrum after a 8.0 s delay was applied to isolated m/z 150.

305 aggregate ions, with the m/z 304 ion being the most abundant aggregate (1.0% of the m/z 152 parent ion). The high abundance of the m/z 304 aggregate indicates that m/z 304 is formed via collision of the m/z 152 cation with the acenaphthylene neutral molecule (152 amu). The appearance of the m/z 303 and m/z 302 ions suggests hydrogen loss during ion-molecule collisions.

Application of a 3.0 s delay to the isolated m/z 151 fragment ion yielded the m/z 303 and m/z 302 aggregate ions. Thus, the m/z 303 ion is formed during reaction of the m/z 151 ion with the acenaphthylene neutral, while m/z 302 is produced by single hydrogen loss during the collision. Due to the low abundance of the m/z 150 fragment ion, an 8.0 s reaction delay was applied to the isolated m/z 150 ion to increase aggregate abundance. This 8.0 s reaction delay resulted in the formation of the m/z 302 and m/z 301 aggregate ions, suggesting reaction of the m/z 150 ion with the acenaphthylene neutral accompanied by single hydrogen loss during collision.

Aggregate fragmentation

Irradiation of the isolated m/z 304 aggregate ion with light from the xenon arc lamp (250 nm to 1100 nm) yielded dehydrogenation to form the m/z 303, 302, 301, and 300 ions, and dissociation to form the m/z 152 parent ion (Figure 4-6). Operating pressure for these aggregate photolysis experiments was 1.3 x 10^{-7} Torr. Regardless of irradiation time, the major photoproduct of m/z 304 was always the m/z 152 ion (~75% yield). Isolation and photolysis of the m/z 303 aggregate for 2.0 s yielded the m/z 302, 301, and 300 ions; however, no m/z 152 was produced by fragmentation of m/z 303 (Figure 4-7). Similarly, photolysis of isolated m/z 302 yielded the m/z 301 and m/z 300 ions. Photolysis of m/z 301 produced only the m/z 300 ion. No hydrogen loss was

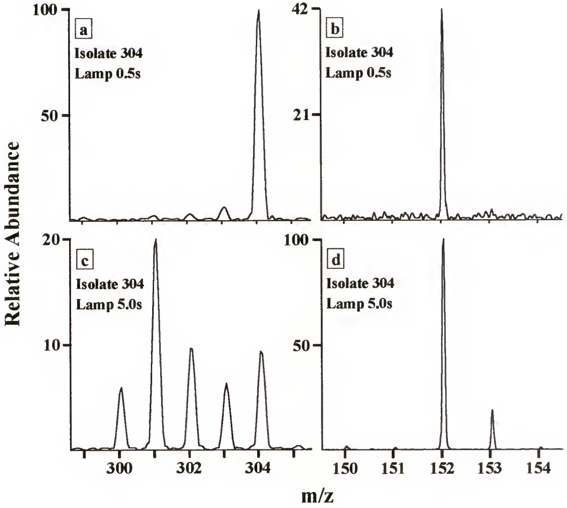

$$304 \xrightarrow{h\nu} 303, 302, 301, 300, 152$$

Figure 4-6. Photolysis of the m/z 304 aggregate ion. A) FT-ICR mass spectrum after Xe lamp irradiation (0.5 s) of isolated m/z 304 (m/z 299-305 range). B) FT-ICR mass spectrum after Xe lamp irradiation (0.5 s) of isolated m/z 304 (m/z 150-154 range). C) FT-ICR mass spectrum after Xe lamp irradiation (5.0 s) of isolated m/z 304 (m/z 299-305 range). D) FT-ICR mass spectrum after Xe lamp irradiation (5.0 s) of isolated m/z 304 (m/z 150-154 range).

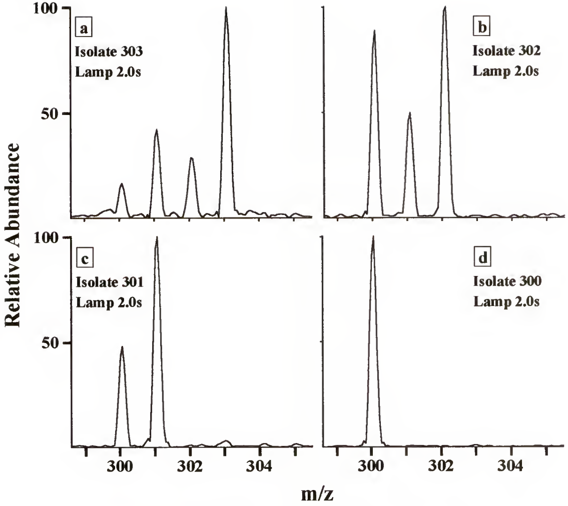

$$303 \xrightarrow{h\nu} 302, 301, 300$$

$$302 \xrightarrow{h\nu} 301, 300$$

$$301 \xrightarrow{h\nu} 300$$

$$300 \xrightarrow{h\nu} X$$

Figure 4-7. Photolysis of the m/z 303, 302, 301, and 300 aggregate ions (m/z 299-305 range). A) FT-ICR mass spectrum after Xe lamp irradiation (2.0 s) of isolated m/z 303. B) FT-ICR mass spectrum after Xe lamp irradiation (2.0 s) of isolated m/z 302. C) FT-ICR mass spectrum after Xe lamp irradiation (2.0 s) of isolated m/z 301. D) FT-ICR mass spectrum after Xe lamp irradiation (2.0 s) of isolated m/z 300.

observed during irradiation of the m/z 300 ion. In each case, the m/z 152, 151, and 150 ions were not produced, indicating that only the m/z 304 aggregate ion can photodissociate to form the m/z 152 parent ion.

The mechanism of hydrogen loss from the m/z 304 aggregate ion was investigated by ejecting specific aggregate ions during lamp irradiation (Figure 4-8). Ejection of the m/z 303 ion during 2.0 s of lamp irradiation eliminated the m/z 302, 301, and 300 ions, indicating that m/z 302 is formed via single hydrogen loss from m/z 303. Similarly, ejection of the m/z 302 ion eliminated the m/z 301 and m/z 300 ions; and, ejection of the m/z 301 ion eliminated the m/z 300 ion. Thus, the m/z 301 and m/z 300 ions are formed via single hydrogen loss from the m/z 302 and m/z 301 ions, respectively. The mechanism of m/z 304 dehydrogenation is sequential loss of four hydrogens.

Acenaphthylene cation fragmentation

Irradiation of the isolated m/z 152 parent ion yielded the m/z 151 and m/z 150 fragment ions (Figure 4-9). To minimize aggregate formation, the partial pressure of acenaphthylene was lowered to 1.8×10^{-8} Torr for these photolysis experiments. Ejection of the m/z 300-305 aggregates during lamp irradiation had no effect on the production of m/z 151 and m/z 150. However, an increase in m/z 153 and m/z 154 during lamp photolysis suggested additional reactions affecting the formation of m/z 151 and m/z 150 ions. Application of a 3.0 s delay to isolated m/z 151 resulted in significant formation of the m/z 152, 153, and 154 ions, suggesting possible hydrogenation or charge transfer (Figure 4-10). Application of a 3.0 s delay to the isolated m/z 150 ion yielded only the m/z 152, 153, and 154 ions. Because the m/z 151 ion was not observed, charge transfer, not hydrogenation, must be the mechanism of m/z 152, 153, and 154 formation.

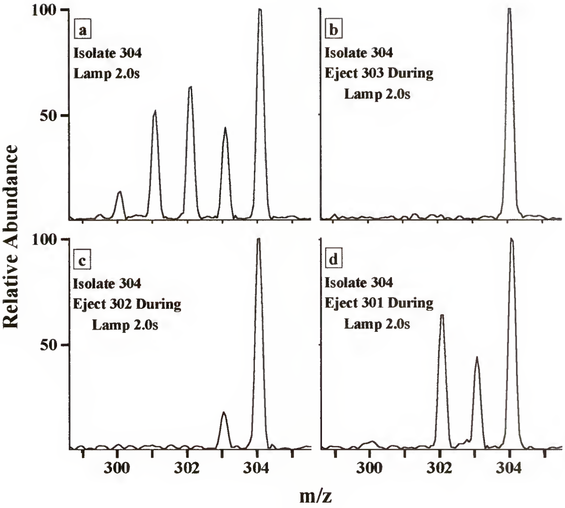

$$304 \xrightarrow{-H} 303 \xrightarrow{-H} 302 \xrightarrow{-H} 301 \xrightarrow{-H} 300$$

Figure 4-8. Dehydrogenation pathway for the m/z 304 aggregate ion (m/z 299-305 range). A) FT-ICR mass spectrum after Xe lamp irradiation (2.0 s) of isolated m/z 304. B) FT-ICR mass spectrum after Xe lamp irradiation (2.0 s) of isolated m/z 304 with simultaneous ejection of m/z 303. C) FT-ICR mass spectrum after Xe lamp irradiation (2.0 s) of isolated m/z 304 with simultaneous ejection of m/z 302. D) FT-ICR mass spectrum after Xe lamp irradiation (2.0 s) of isolated m/z 304 with simultaneous ejection of m/z 301.

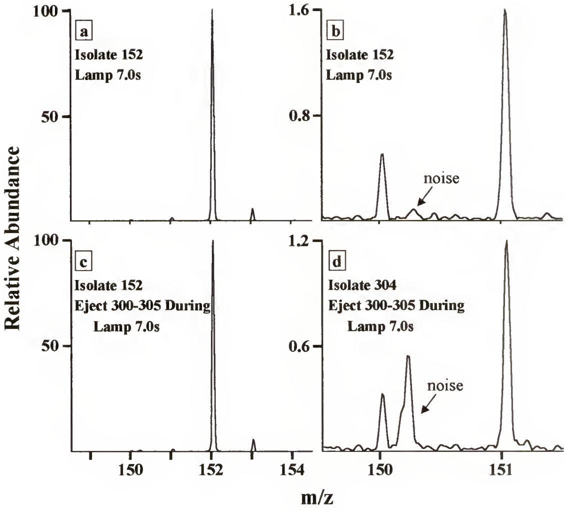

$$152 \xrightarrow{-H} 151 \xrightarrow{-H} 150$$

Figure 4-9. Dehydrogenation pathway for the m/z 152 parent ion. Labeled noise peaks were produced during waveform application. A) FT-ICR mass spectrum after Xe lamp irradiation (7.0 s) of isolated m/z 152 (m/z 149-154 range). B) FT-ICR mass spectrum after Xe lamp irradiation (7.0 s) of isolated m/z 152 (m/z 150-151 range). C) FT-ICR mass spectrum after Xe lamp irradiation (7.0 s) of isolated m/z 152 with simultaneous ejection of m/z 300-305 (m/z 149-154 range). D) FT-ICR mass spectrum after Xe lamp irradiation (7.0 s) of isolated m/z 152 with simultaneous ejection of m/z 300-305 (m/z 150-151 range).

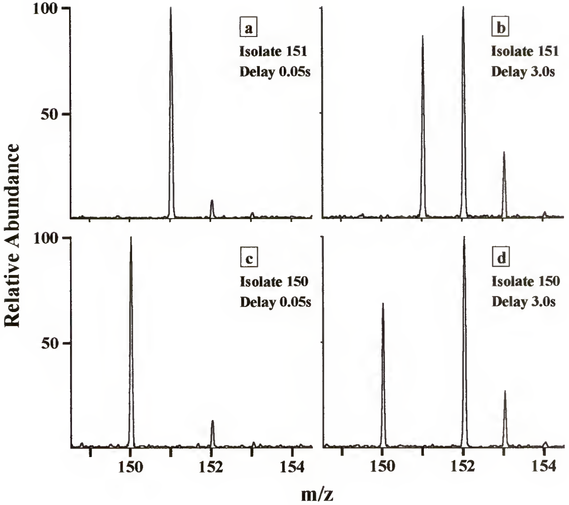

$$151^{+} + 152\,\mathrm{n} \longrightarrow 152^{+} + 151\,\mathrm{n}$$

$$151^{+} + 153\,\mathrm{n} \longrightarrow 153^{+} + 151\,\mathrm{n}$$

$$151^{+} + 154\,\mathrm{n} \longrightarrow 154^{+} + 151\,\mathrm{n}$$

$$150^{+} + 152\,\mathrm{n} \longrightarrow 152^{+} + 150\,\mathrm{n}$$

$$150^{+} + 153\,\mathrm{n} \longrightarrow 153^{+} + 150\,\mathrm{n}$$

$$150^{+} + 154\,\mathrm{n} \longrightarrow 154^{+} + 150\,\mathrm{n}$$

Figure 4-10. Charge transfer reactions for the m/z 151 and m/z 150 fragment ions (m/z 149-154 range). The "n" label designates neutral molecules. A) FT-ICR mass spectrum after isolated m/z 151 undergoes a 0.05 s reaction delay. B) FT-ICR mass spectrum after isolated m/z 151 undergoes a 3.0 s reaction delay. C) FT-ICR mass spectrum after isolated m/z 150 undergoes a 0.05 s reaction delay. D) FT-ICR mass spectrum after isolated m/z 150 undergoes a 3.0 s reaction delay.

To determine the dehydrogenation pathway of the m/z 152 parent ion, specific ions were ejected during lamp irradiation (Figure 4-11). Ejection of the aggregate ions (m/z 300-305) and the charge transfer products (m/z 153, m/z 154) during 7.0 s of lamp irradiation had no effect on the m/z 151 and m/z 150 ions, confirming that these fragment ions are produced solely from the m/z 152 parent ion. Thus, the only mechanism for m/z 151 formation is single hydrogen loss from the m/z 152 ion. Ejection of the m/z 151 ion during lamp irradiation eliminated the m/z 150 ion, indicating that m/z 150 is formed via single hydrogen loss from the m/z 151 ion.

Overall aggregation and photofragmentation pathway

The overall aggregation and photofragmentation pathway for the acenaphthylene cation is shown in Figure 4-12. Due to the competing dissociation, aggregation, and charge transfer mechanisms involved, percent yields were incalculable. During lamp irradiation, the m/z 152 parent ion either lost one hydrogen to form the m/z 151 fragment ion, or reacted with acenaphthylene neutral to form the m/z 304 and m/z 303 aggregate ions. The m/z 151 ion photodissociated further to produce the m/z 150 fragment ion via single hydrogen loss. The m/z 151 ion also reacted with acenaphthylene neutral to form the m/z 303 and m/z 302 ions. Photodissociation of the m/z 150 ion was not observed. However, the m/z 150 ion reacted with the acenaphthylene neutral to form the m/z 302 and m/z 301 aggregate ions.

After formation, the m/z 304 aggregate ion either photodissociated to the m/z 152 parent ion and acenaphthylene neutral (~75% yield), or lost one hydrogen to form the m/z 303 cation. After the loss of one hydrogen to form the m/z 303 ion, dissociation to the m/z 152 parent ion was no longer observed. The m/z 303 aggregate ion underwent

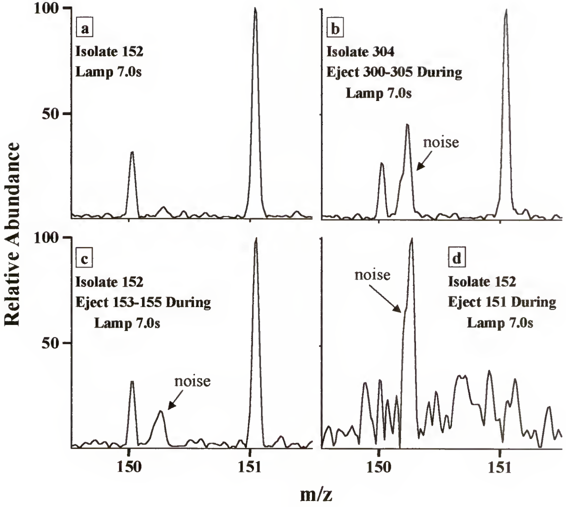

$$152 \xrightarrow{-H} 151 \xrightarrow{-H} 150$$

Figure 4-11. Dehydrogenation pathway for the m/z 152 parent ion (m/z 150-151 range). Labeled noise peaks were produced during waveform application. A) FT-ICR mass spectrum after Xe lamp irradiation (7.0 s) of isolated m/z 152. B) FT-ICR mass spectrum after Xe lamp irradiation (7.0 s) of isolated m/z 152 with simultaneous ejection of m/z 303-305. C) FT-ICR mass spectrum after Xe lamp irradiation (7.0 s) of isolated m/z 152 with simultaneous ejection of m/z 153-155. D) FT-ICR mass spectrum after Xe lamp irradiation (7.0 s) of isolated m/z 152 with simultaneous ejection of m/z 151.

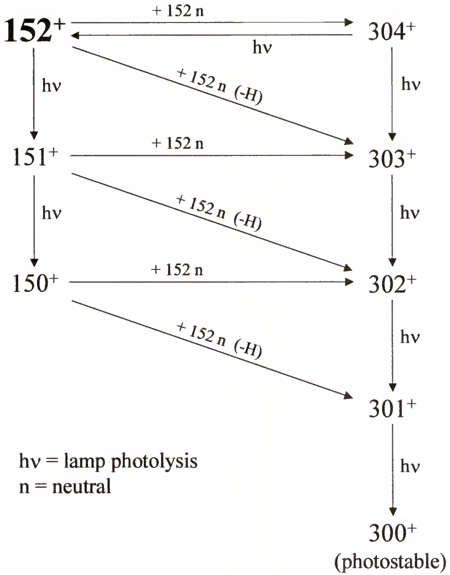

Figure 4-12. Overall observed aggregation and photodissociation pathway for the acenaphthylene cation (m/z 152).

sequential hydrogen loss to form the m/z 302, 301, and 300 ions. Regardless of irradiation time, no further photofragmentation was observed for the m/z 300 ion, indicating that it was photostable.

Comparison of observed and predicted dissociation pathways

Because the structures of the aggregate ions are unknown, only the sequential hydrogen loss pathway of the m/z 152 ion was calculated. Each of the hydrogens attached to the six-membered rings in the acenaphthylene cation is a likely candidate for removal to form the m/z 151 fragment ion. Calculated energies required for this first hydrogen removal ranged from 4.77 eV to 5.06 eV. These relatively high carbon-hydrogen bond energies may explain the low abundances of the observed m/z 151 and m/z 150 ions. Regardless of the first of these three hydrogens removed, the second hydrogen is abstracted from a position adjacent to the first hydrogen removed. Energies required for removal of this second hydrogen to form m/z 150 ranged from 3.69 eV to 4.09 eV. These lower energies are consistent with the observed abundance ratios of the m/z 151 and m/z 150 ions.

CHAPTER 5
AGGREGATION OF THE ACENAPHTHYLENE CATION

In FT-ICR studies, the acenaphthylene cation ($C_{12}H_8^+$) aggregated to form a dimer-like species ($C_{24}H_{16}^+$) with a mass of 304 amu. Although the dimerization of neutral acenaphthylene has been well-characterized,[63-68] the aggregation product of the acenaphthylene cation is unknown. To determine the structure of the aggregate ion, two $C_{24}H_{16}$ species were studied: cyclobuta[1,2-α:3,4-α′]diacenaphthylene and 1,1′-bi-(acenaphthenylidene). These PAHs were chosen based on their plausible acenaphthylene dimer-like structure.

Cyclobuta[1,2-α:3,4-α′]diacenaphthylene

Structure

Cyclobuta[1,2-α:3,4-α′]diacenaphthylene ($C_{24}H_{16}$) consists of two acenaphthylene units joined by a four-membered ring (Figure 5-1). Due to the absence of double bonds in the four-membered ring, cyclobuta[1,2-α:3,4-α′]diacenaphthylene has two stereoisomeric forms: the *Z*-isomer, with the acenaphthylene components on the same side of the four-membered ring, and the *E*-isomer, with the acenaphthylene components on opposite sides of the four-membered ring. For convenience, cyclobuta [1,2-α:3,4-α′]diacenaphthylene will be referred to as cyclobutadiacenaphthylene from this point forward.

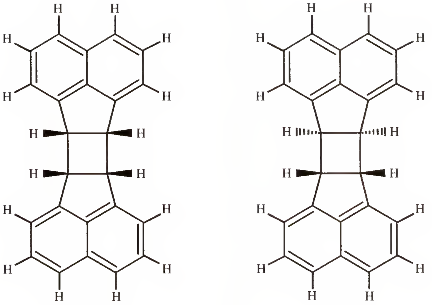

Z-isomer *E*-isomer

Figure 5-1. Cyclobutadiacenaphthylene stereoisomers.

Background

Dimerization of acenaphthylene was first observed by Dziewonski and Rapalski acenaphthylene solutions were exposed to direct sunlight.[63] Because molecules with ethylene linkages often react photochemically to form cyclobutane rings, the dimerization product was assigned as cyclobutadiacenaphthylene. This assignment was later verified by X-ray analysis of the purified dimerization products.[64] Photodimerization of the yellow acenaphthylene monomer to the colorless dimer occurred at wavelengths greater than 350 nm.[65] Dissociation of the dimer to acenaphthylene occurred at wavelengths less than 350 nm.

The first step in early acenaphthylene dimerization mechanisms was formation of a ground-state van der Waals complex. This complex consisted of two acenaphthylene molecules joined by dispersion forces between π electrons in the six-membered rings.[65]

Subsequent photon absorption would create an excited van der Waals complex, from which the dimer was formed. However, due to the face-to-face alignment required for the π electron overlap, this van der Waals complex could form only the *Z*-isomer.

Excited states participating in the dimerization mechanism were later identified using triplet state quenching and sensitization techniques.[66,67] Addition of triplet quenchers to acenaphthylene solutions prevented formation of the *E*-dimer and slightly reduced production of the *Z*-dimer. Moreover, the presence of triplet sensitizers increased the relative yield of the *E*-dimer. Thus, the *E*-dimer was produced from a triplet state species, while the *Z*-dimer was formed from both the triplet and singlet states. Since the majority of the *Z*-dimer was formed from a singlet excimer, it was proposed that this singlet species was the excited van der Waals complex. However, no ground-state van der Waals complexes were spectroscopically observed.

Kinetic studies conducted by Haga et al. clarified the role of the singlet (S_1) and triplet (T_1) states in the dimerization mechanism (Figure 5-2).[68] Due to the short lifetime of the S_1 state (10^{-10} s) and the low intersystem crossing efficiency for acenaphthylene ($\Phi = 0.029$ in cyclohexane), the relative yields of the *E*-dimer and *Z*-dimer were found to be concentration dependent. In concentrated solutions, acenaphthylene in the S_1 state reacted with ground-state acenaphthylene to form the *Z*-dimer before intersystem crossing could occur. However, in dilute solutions, intersystem crossing to the T_1 state proceeded faster than the reaction of the S_1 state with ground-state acenaphthylene. Reaction of this longer-lived triplet state (10^{-6} s) with ground-state acenaphthylene yielded a mixture of the *Z* and *E*-dimers.

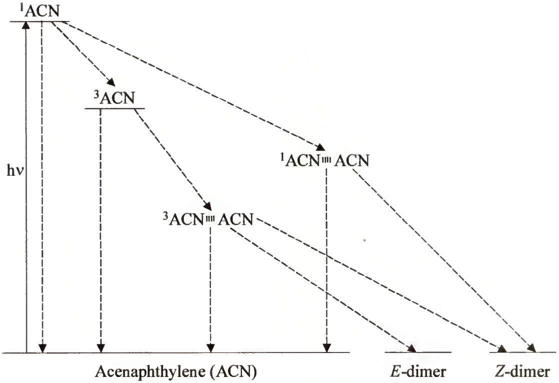

Figure 5-2. Mechanism for acenaphthylene dimerization.

DFT Calculations

The optimized geometry for the ground state of the cyclobutadiacenaphthylene cation was calculated at the B3LYP/6-31G(d,p) level of theory. Optimizations for both the *E*-isomer and *Z*-isomer of the cation were conducted; however, geometry optimizations for the *Z*-isomer failed to converge. Therefore, geometries and ground-state energies presented correspond to the cyclobutadiacenaphthylene cation *E*-isomer only. The cyclobutadiacenaphthylene structure with labeled atom positions is shown in Figure 5-3. Numbered positions correspond to IUPAC numbering conventions. Letter designations are unique to this work.

Bond lengths and bond angles for the cyclobutadiacenaphthylene cation are presented in Table 5-1 and Table 5-2, respectively. Due to the large number of

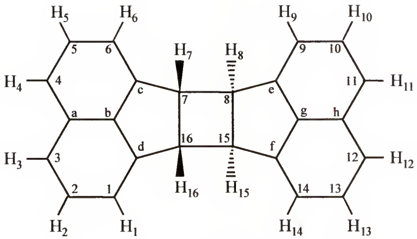

Figure 5-3. Structure and atom position labeling for the *E*-isomer of cyclobutadiacenaphthylene.

Table 5-1. Bond lengths (Å) calculated at the B3LYP/6-31G(d,p) level of theory for the cyclobutadiacenaphthylene cation.

Bond	Length (Å)	Bond	Length (Å)
C_1-C_2	1.4106	C_1-H_1	1.0857
C_2-C_3	1.3957	C_2-H_2	1.0852
C_3-C_a	1.4190	C_3-H_3	1.0859
C_a-C_b	1.4124	C_{16}-H_{16}	1.0911
C_b-C_d	1.4107		
C_d-C_1	1.3923		
C_d-C_{16}	1.4989		
C_7-C_{16}	1.5653		
C_{15}-C_{16}	1.6107		

geometrically equivalent carbon and hydrogen positions, each unique bond length and bond angle is tabulated only once. Because the dihedral bond angle incorporating the four-membered and five-membered rings (C_d-C_{16}-C_{15}-C_f) is 146.5°, the optimized structure is clearly that of the *E*-isomer. (A dihedral angle of 0° would be expected for the *Z*-isomer.) Calculated atomic spin densities for the cyclobutadiacenaphthylene cation are presented in Table 5-3. In this radical cation, the largest atomic spin density resides on C_3, C_4, C_{11}, and C_{12}.

Table 5-2. Bond angles (degrees) calculated at the B3LYP/6-31G(d,p) level of theory for the cyclobutadiacenaphthylene cation.

Angle	Degrees	Angle	Degrees
C_1-C_2-C_3	122.3	H_1-C_1-C_2	119.7
C_2-C_3-C_a	120.3	H_2-C_2-C_3	118.9
C_3-C_a-C_b	116.7	H_3-C_3-C_a	120.0
C_a-C_b-C_d	123.7	H_{15}-C_{15}-C_8	117.3
C_b-C_d-C_1	118.7	H_{16}-C_{16}-C_d	114.2
C_d-C_1-C_2	118.7	H_{16}-C_{16}-C_7	117.3
C_c-C_b-C_d	112.6	H_{16}-C_{16}-C_{15}	112.6
C_b-C_d-C_{16}	108.6		
C_d-C_{16}-C_7	105.1	C_d-C_{16}-C_{15}-C_f	146.5
C_7-C_{16}-C_{15}	90.0		

Table 5-3. Atomic spin densities calculated at the B3LYP/6-31G(d,p) level of theory for the cyclobutadiacenaphthylene cation.

Atom	Spin Density	Atom	Spin Density
C_1	0.073135	H_1	-0.003487
C_2	-0.021717	H_2	0.000284
C_3	0.157517	H_3	-0.006320
C_{16}	0.015358	H_{16}	0.007847
C_a	-0.059128		
C_b	-0.013903		
C_d	0.063865		

Due to the size of the cyclobutadiacenaphthylene system, energies for hydrogen abstraction from the cyclobutadiacenaphthylene cation were not calculated. However, the formation energy of the cyclobutadiacenaphthylene cation from an acenaphthylene cation and an acenaphthylene neutral can be estimated from the ground-state energies of the reactants and products (Figure 5-4). Approximately 1.15 eV is released during formation of the cyclobutadiacenaphthylene cation, indicating this reaction is energetically favorable overall. However, the energy barrier for this reaction may be significant due to the specific molecular orientations required for bond formation.

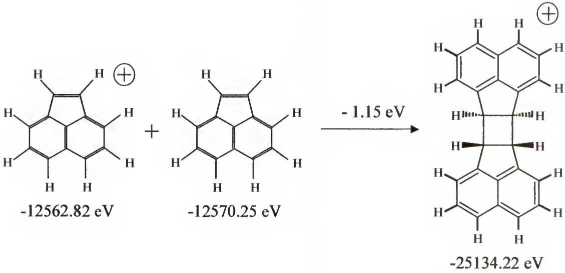

Figure 5-4. Calculation of the energy released during cyclobutadiacenaphthylene cation formation from cationic and neutral acenaphthylene.

FT-ICR Mass Spectrometry

Due to the low vapor pressure of cyclobutadiacenaphthylene, a heated probe equipped with a brass sample cup was required for vaporization of the solid. The optimal probe temperature for cyclobutadiacenaphthylene vaporization was 120°C. Background pressure for these experiments was 4 x 10^{-9} Torr. Vaporization of the solid at 120°C produced no observable increase in operating pressure, indicating that very little sample actually remained in the gas phase. Due to the large distance between the sample cup and the filament, most of the vaporized cyclobutadiacenaphthylene likely condensed onto the walls of the vacuum system before reaching the ionization region. Optimal ionization conditions were a filament current of 2.5 A and a repeller potential of -16 V. Electron bombardment of neutral cyclobutadiacenaphthylene (Figure 5-5) yielded the m/z 304 parent ion, ^{13}C isotope ions (m/z 305, m/z 306), dehydrogenated fragment ions (m/z 303-300, m/z 298-296), and dissociated fragment ions (m/z 154-151).

Irradiation of the isolated m/z 304 parent ion with light from the xenon arc lamp (250 nm to 1100 nm) yielded dehydrogenation to form m/z 303, 302, 301, and 300, and dissociation to form m/z 154, 153, and 152 (Figure 5-6). The major photoproduct of m/z 304 was the m/z 152 ion. Regardless of irradiation time, dehydrogenation terminated after the loss of four hydrogens from the m/z 304 ion, indicating that the resulting m/z 300 ion was photostable (Figure 5-7). Due to the low abundance of each dehydrogenated fragment ion, isolation and subsequent photolysis of these fragment ions was not possible.

The mechanism of hydrogen loss from the m/z 304 parent ion was investigated by ejecting specific ions during lamp irradiation (Figure 5-8). Ejection of the m/z 303 ion during 3.0 s of lamp irradiation eliminated the m/z 302, 301, and 300 ions. Ejection of the m/z 302 ion eliminated the m/z 301 and m/z 300 ions. Ejection of the m/z 301 ion eliminated the m/z 300 ion. Therefore, the dehydrogenation mechanism for the cyclobutadiacenaphthylene cation is the sequential loss of four hydrogens.

Proposed Structure of m/z 300

Although carbon-hydrogen bond energies were not calculated for the cyclobutadiacenaphthylene ion, a possible structure for the observed photostable m/z 300

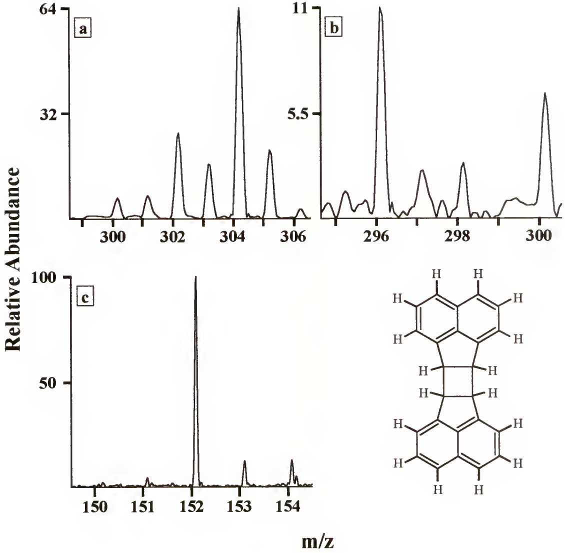

cyclobutadiacenaphthylene $\xrightarrow{\text{e- impact}}$ **306, 305, 304, 303, 302, 301, 300**

298, 297, 296, 154, 153, 152, 151

Figure 5-5. Electron ionization of cyclobutadiacenaphthylene ($C_{24}H_{16}$). A) FT-ICR mass spectrum in the m/z 299-306 range. B) FT-ICR mass spectrum in the m/z 295-300 range. C) FT-ICR mass spectrum in the m/z 150-154 range.

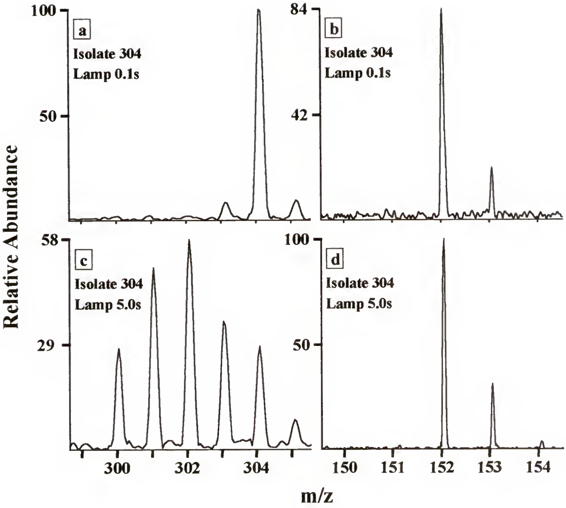

$$304 \xrightarrow{h\nu} 303, 302, 301, 300, 154, 153, 152$$

Figure 5-6. Photolysis of the cyclobutadiacenaphthylene cation (m/z 304). A) FT-ICR mass spectrum after Xe lamp irradiation (0.1 s) of isolated m/z 304 (m/z 299-305 range). B) FT-ICR mass spectrum after Xe lamp irradiation (0.1 s) of isolated m/z 304 (m/z 150-154 range). C) FT-ICR mass spectrum after Xe lamp irradiation (5.0 s) of isolated m/z 304 (m/z 299-305 range). D) FT-ICR mass spectrum after Xe lamp irradiation (5.0 s) of isolated m/z 304 (m/z 150-154 range).

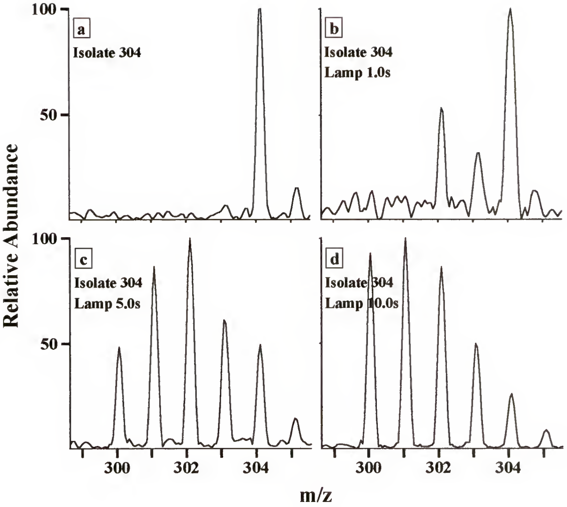

$$304 \xrightarrow{h\nu} 303, 302, 301, 300$$

Figure 5-7. Photolysis of the cyclobutadiacenaphthylene cation (m/z 304) in the m/z 299-305 range. A) FT-ICR mass spectrum of isolated m/z 304. B) FT-ICR mass spectrum after Xe lamp irradiation (1.0 s) of isolated m/z 304. C) FT-ICR mass spectrum after Xe lamp irradiation (5.0 s) of isolated m/z 304. D) FT-ICR mass spectrum after Xe lamp irradiation (10.0 s) of isolated m/z 304.

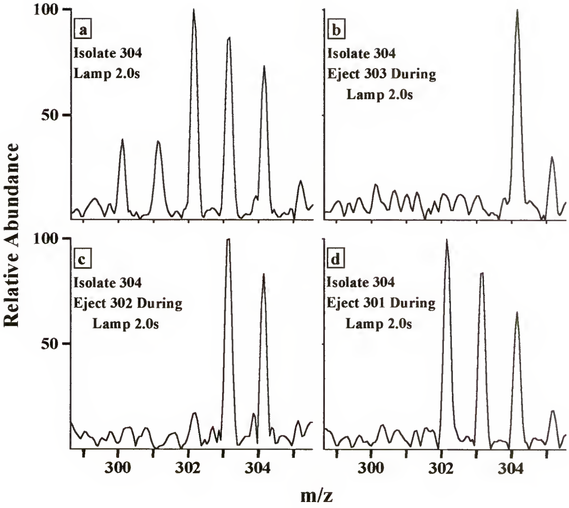

$$\mathbf{304} \xrightarrow{\text{-H}} \mathbf{303} \xrightarrow{\text{-H}} \mathbf{302} \xrightarrow{\text{-H}} \mathbf{301} \xrightarrow{\text{-H}} \mathbf{300}$$

Figure 5-8. Dehydrogenation pathway for the cyclobutadiacenaphthylene cation (m/z 299-305 range). A) FT-ICR mass spectrum after Xe lamp irradiation (2.0 s) of isolated m/z 304. B) FT-ICR mass spectrum after Xe lamp irradiation (2.0 s) of isolated m/z 304 with simultaneous ejection of m/z 303. C) FT-ICR mass spectrum after Xe lamp irradiation (2.0 s) of isolated m/z 304 with simultaneous ejection of m/z 302. D) FT-ICR mass spectrum after Xe lamp irradiation (2.0 s) of isolated m/z 304 with simultaneous ejection of m/z 301.

ion involves removal of the four hydrogens attached to the four-membered ring. Because calculated C-H bond lengths for these hydrogens are slightly greater than calculated C-H bond lengths in the six-membered ring, the hydrogens attached to the four-membered ring may be more weakly bound. If these hydrogens are removed from the m/z 304 ion, the resulting m/z 300 ion is a fully conjugated system, though still antiaromatic (Figure 5-9). This proposed structure is similar to that of biphenylene, which was observed to be photostable by Ekern et al. in similar photodissociation experiments.[47] However, relative bond strengths may change drastically after the removal of the first hydrogen. Therefore, carbon-hydrogen bond energies in the m/z 303, 302, and 301 ions must be calculated before an accurate structure for m/z 300 can be predicted.

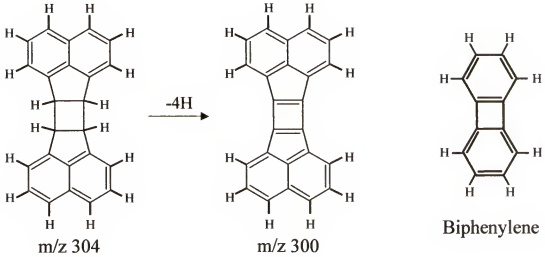

Figure 5-9. Possible structure for the photostable m/z 300 ion produced by removal of four hydrogens from the cyclobutadiacenaphthylene cation. The proposed structure of m/z 300 is similar to that of the photostable biphenylene ion.

1,1′-Bi-(acenaphthenylidene)

Structure

The structure of 1,1′-bi-(acenaphthenylidene) consists of two acenaphthylene-like units joined by a double bond between the two five-membered rings (Figure 5-10). From this point forward, 1,1′-bi-(acenaphthenylidene) will be referred to as biacenaphthenylidene.

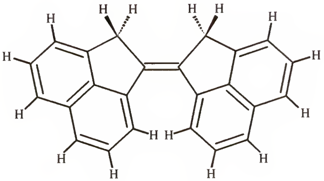

Figure 5-10. Structure of biacenaphthenylidene.

DFT Calculations

The optimized geometry for the ground state of the biacenaphthenylidene cation was calculated at the B3LYP/6-31G(d,p) level of theory. The biacenaphthenylidene structure with labeled atom positions is shown in Figure 5-11. Numbered positions correspond to IUPAC numbering conventions. Letter designations are unique to this work.

Bond lengths and bond angles for the biacenaphthenylidene cation are presented in Table 5-4 and Table 5-5, respectively. Due to the large number of geometrically equivalent carbon and hydrogen positions in the biacenaphthenylidene structure, each unique bond length and bond angle is tabulated only once. Because the dihedral angle

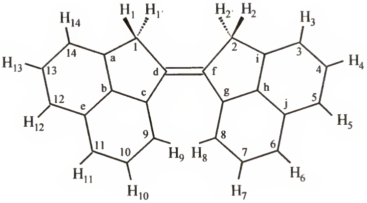

Figure 5-11. Atom position labeling for biacenaphthenylidene.

Table 5-4. Bond lengths (Å) calculated at the B3LYP/6-31G(d,p) level of theory for the biacenaphthenylidene cation.

Bond	Length (Å)	Bond	Length (Å)
C_1-C_a	1.5078	C_1-H_1	1.0974
C_a-C_b	1.3999	C_1-$H_{1'}$	1.0994
C_b-C_c	1.4280	C_9-H_9	1.0824
C_c-C_d	1.4416	C_{10}-H_{10}	1.0851
C_d-C_1	1.5327	C_{11}-H_{11}	1.0862
C_a-C_{14}	1.3848	C_{12}-H_{12}	1.0856
C_{14}-C_{13}	1.4175	C_{13}-H_{13}	1.0851
C_{13}-C_{12}	1.3973	C_{14}-H_{14}	1.0857
C_{12}-C_e	1.4209		
C_e-C_b	1.4111		
C_e-C_{11}	1.4169		
C_{11}-C_{10}	1.3993		
C_{10}-C_9	1.4020		
C_9-C_c	1.4077		
C_d-C_f	1.3925		

Table 5-5. Bond angles (degrees) calculated at the B3LYP/6-31G(d,p) level of theory for the biacenaphthenylidene cation.

Angle	**Degrees**	**Angle**	**Degrees**
C_1-C_d-C_c	107.8	H_1-C_1-$H_{1'}$	106.2
C_d-C_c-C_b	107.7	H_1-C_1-C_d	111.2
C_c-C_b-C_a	112.3	$H_{1'}$-C_1-C_d	110.9
C_b-C_a-C_1	107.7	H_9-C_a-C_{10}	119.2
C_a-C_1-C_d	104.3	H_{10}-C_{10}-C_{11}	118.8
C_1-C_d-C_f	120.9	H_{11}-C_{11}-C_e	119.9
C_a-C_b-C_e	123.5	H_{12}-C_{12}-C_{13}	120.2
C_b-C_e-C_{12}	116.6	H_{13}-C_{13}-C_{14}	118.6
C_e-C_{12}-C_{13}	119.9	H_{14}-C_{14}-C_a	121.6
C_{12}-C_{13}-C_{14}	122.2		
C_{13}-C_{14}-C_a	118.8	C_1-C_d-C_f-C_2	18.0
C_{14}-C_a-C_b	119.0		
C_b-C_c-C_9	117.5		
C_c-C_9-C_{10}	119.1		
C_9-C_{10}-C_{11}	122.5		
C_{10}-C_{11}-C_e	120.5		
C_{11}-C_e-C_b	116.1		
C_e-C_b-C_c	124.1		

between the two acenaphthylene-like units (C_1-C_d-C_f-C_2) is greater than 0°, the biacenaphthenylidene structure is not planar. This 18° twist around the connecting double bond is presumably due to repulsions between H_8 and H_9. Calculated atomic spin densities for the biacenaphthenylidene cation are presented in Table 5-6. In this radical cation, the largest atomic spin density resides on C_{11} and C_6, with significant spin density also appearing on C_9, C_d, C_f, and C_8.

Table 5-6. Atomic spin densities calculated at the B3LYP/6-31G(d,p) level of theory for the biacenaphthenylidene cation.

Atom	Spin Density	Atom	Spin Density
C_1	-0.008639	H_1	0.009246
C_9	0.136607	$H_{1'}$	0.015577
C_{10}	-0.057352	H_9	-0.005820
C_{11}	0.205178	H_{10}	0.001526
C_{12}	0.104135	H_{11}	-0.008385
C_{13}	-0.048164	H_{12}	-0.004187
C_{14}	0.084308	H_{13}	0.001615
C_a	-0.009195	H_{14}	-0.003665
C_b	0.023699		
C_c	-0.001800		
C_d	0.130681		
C_e	-0.065365		

Due to the size of the biacenaphthenylidene system, energies for hydrogen abstraction from the biacenaphthenylidene cation were not calculated. The formation energy of the biacenaphthenylidene cation from an acenaphthylene cation and an acenaphthylene neutral was estimated from the ground-state energies of the reactants and products (Figure 5-12). Approximately 2.03 eV is released during formation of the biacenaphthenylidene cation, indicating this reaction is energetically favorable overall. However, the energy barrier for this reaction may be significant due to the hydrogen rearrangement required for biacenaphthenylidene formation.

FT-ICR Mass Spectrometry

As in the case of cyclobutadiacenaphthylene, biacenaphthenylidene required a heated probe equipped with a brass sample cup for vaporization. The optimal probe temperature for biacenaphthenylidene vaporization was 185°C. Background pressure for

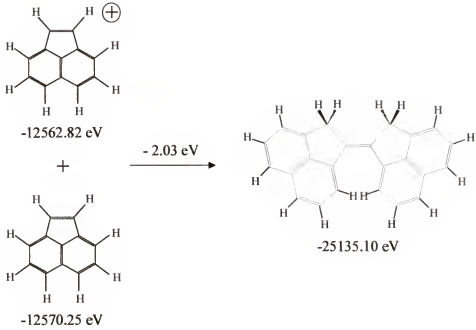

Figure 5-12. Calculation of the energy released during biacenaphthenylidene cation formation from cationic and neutral acenaphthylene.

these experiments was 8 x 10^{-9} Torr. Vaporization of biacenaphthenylidene at 185°C resulted in an operating pressure of 1.0 x 10^{-8} Torr, which corresponds to approximately 7 x 10^{7} biacenaphthenylidene molecules/cm^{3}. Optimal ionization conditions were a 1.8 A filament current and a -20 V repeller potential. Electron bombardment of neutral biacenaphthenylidene (Figure 5-13) yielded the m/z 304 parent ion, ^{13}C isotope ions (m/z 305, m/z 306), dehydrogenated fragment ions (m/z 303-300, m/z 298-296), and dissociated fragment ions (m/z 154-150).

Irradiation of the isolated m/z 304 parent ion with light from the xenon arc lamp (250 nm to 1100 nm) yielded dehydrogenation to form m/z 303, 302, 301, and 300, and dissociation to form m/z 154, 153, 152, and 151 (Figure 5-14). The major photoproduct of m/z 304 was the m/z 152 ion. Regardless of irradiation time, dehydrogenation

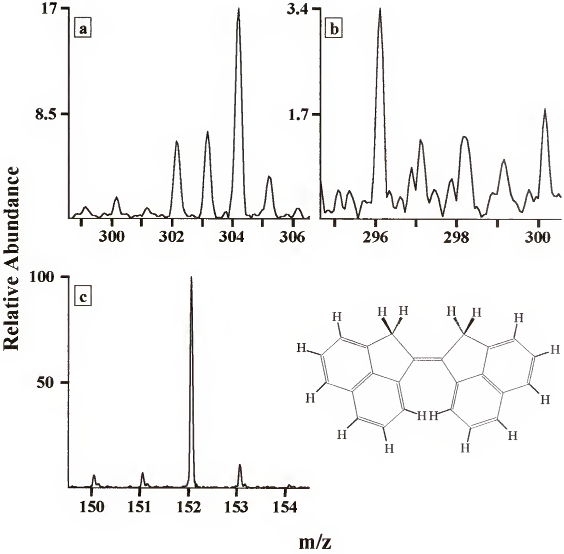

biacenaphthenylidene $\xrightarrow{\text{e- impact}}$ **306, 305, 304, 303, 302, 301, 300**

298, 297, 296, 154, 153, 152, 151, 150

Figure 5-13. Electron ionization of biacenaphthenylidene ($C_{24}H_{16}$). A) FT-ICR mass spectrum in the m/z 299-306 range. B) FT-ICR mass spectrum in the m/z 295-300 range. C) FT-ICR mass spectrum in the m/z 150-154 range.

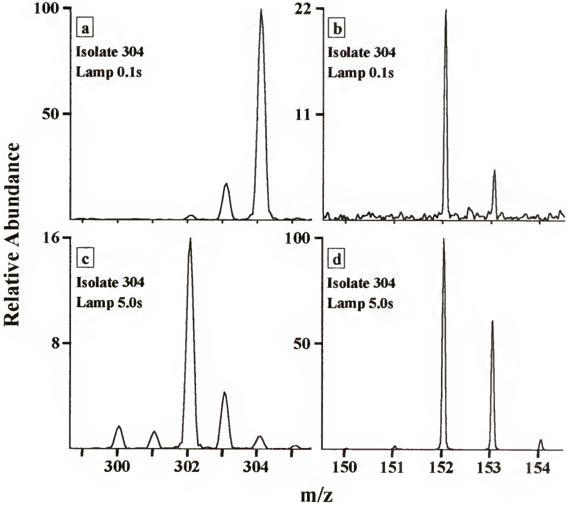

$$304 \xrightarrow{h\nu} 303, 302, 301, 300, 154, 153, 152, 151, 150$$

Figure 5-14. Photolysis of the biacenaphthenylidene cation (m/z 304). A) FT-ICR mass spectrum after Xe lamp irradiation (0.1 s) of isolated m/z 304 (m/z 299-305 range). B) FT-ICR mass spectrum after Xe lamp irradiation (0.1 s) of isolated m/z 304 (m/z 150-154 range). C) FT-ICR mass spectrum after Xe lamp irradiation (5.0 s) of isolated m/z 304 (m/z 299-305 range). D) FT-ICR mass spectrum after Xe lamp irradiation (5.0 s) of isolated m/z 304 (m/z 150-154 range).

terminated after the loss of four hydrogens from the m/z 304 ion, indicating that the resulting m/z 300 ion was photostable (Figure 5-15). Due to the low abundance of each dehydrogenated fragment ion, isolation and subsequent photolysis of these fragment ions was not possible.

The mechanism of hydrogen loss from the m/z 304 parent ion was investigated by ejecting specific ions during lamp irradiation (Figure 5-16). Ejection of the m/z 303 ion during 3.0 s of lamp irradiation greatly reduced, but did not eliminate the m/z 302, 301, and 300 ions. Ejection of the m/z 302 ion eliminated the m/z 301 ion, and reduced the m/z 300 ion. Ejection of the m/z 301 ion eliminated the m/z 300 ion. Therefore, the dehydrogenation mechanism for the biacenaphthenylidene cation is not purely sequential hydrogen loss. Since all of the m/z 302 did not disappear during ejection of m/z 303, the formation of m/z 302 involves both single hydrogen loss from m/z 303 (major route) and double hydrogen loss from m/z 304 (minor route).

Although ejection of m/z 302 eliminates m/z 301 from the mass spectrum, the remaining m/z 300 ion suggests m/z 301 may be formed from m/z 303 as well as from m/z 302. Ejection of m/z 301 eliminates m/z 300, indicating that m/z 300 is formed via single hydrogen loss from m/z 301. Because m/z 300 is reduced, but not eliminated, by m/z 302 ejection, the m/z 302 ion cannot account for all of the m/z 301 ion produced. If m/z 301 were completely eliminated by m/z 302 ejection, m/z 300 would disappear as well. Therefore, the m/z 301 ion must be produced partly by double hydrogen loss from m/z 303. The m/z 301 ion is absent from the mass spectrum during ejection of m/z 302 because m/z 301 dehydrogenates further to form the observed m/z 300.

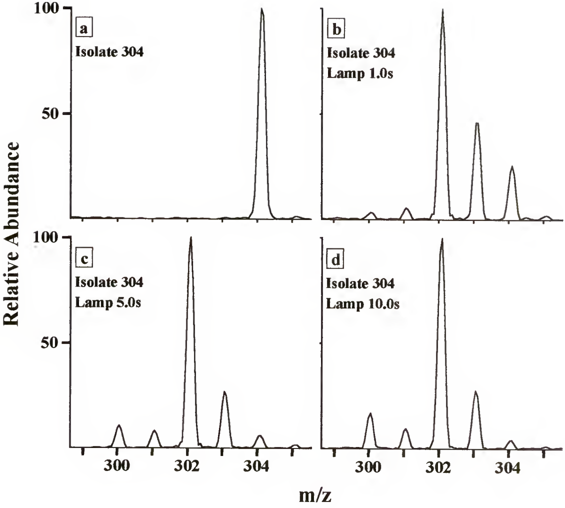

$$304 \xrightarrow{h\nu} 303, 302, 301, 300$$

Figure 5-15. Photolysis of the biacenaphthenylidene cation (m/z 304) in the m/z 299-305 range. A) FT-ICR mass spectrum of isolated m/z 304. B) FT-ICR mass spectrum after Xe lamp irradiation (1.0 s) of isolated m/z 304. C) FT-ICR mass spectrum after Xe lamp irradiation (5.0 s) of isolated m/z 304. D) FT-ICR mass spectrum after Xe lamp irradiation (10.0 s) of isolated m/z 304.

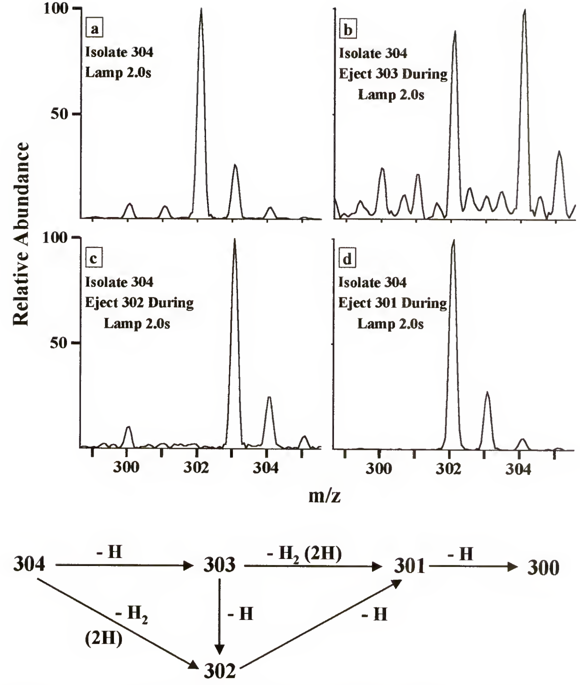

Figure 5-16. Dehydrogenation pathway for the biacenaphthenylidene cation (m/z 299-305 range). A) FT-ICR mass spectrum after Xe lamp irradiation (2.0 s) of isolated m/z 304. B) FT-ICR mass spectrum after Xe lamp irradiation (2.0 s) of isolated m/z 304 with simultaneous ejection of m/z 303. C) FT-ICR mass spectrum after Xe lamp irradiation (2.0 s) of isolated m/z 304 with simultaneous ejection of m/z 302. D) FT-ICR mass spectrum after Xe lamp irradiation (2.0 s) of isolated m/z 304 with simultaneous ejection of m/z 301.

Proposed Structure of m/z 300

Although carbon-hydrogen bond energies were not calculated for the biacenaphthenylidene ion, formation of the photostable m/z 300 ion most likely begins with abstraction of hydrogens attached to sp^3 hybridized carbons in the five-membered rings. Removal of these two hydrogens may yield a relatively stable m/z 302 ion (Figure 5-17), which would account for the observed high abundance of m/z 302 relative to m/z 301 and m/z 300. Based on bond energy calculations for acenaphthylene, it is unlikely that the remaining two hydrogens on the five membered rings will be removed. All other hydrogens are attached to sp^2 carbons in the six-membered rings, and thus appear energetically equivalent. However, the proximity of the two hydrogens bound to C_8 and C_9 suggests possible removal to form an H_2 molecule. Removal of these two hydrogens may result in a ring closure to form a potentially stable, planar m/z 300 ion.

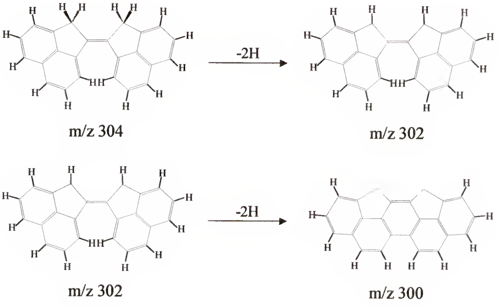

Figure 5-17. Possible structure for the photostable m/z 300 ion produced by removal of four hydrogens from the biacenaphthenylidene cation.

Comparison to the Acenaphthylene Aggregate

Candidates for the observed acenaphthylene aggregate must meet two photofragmentation criteria: dissociation to form the m/z 152 ion and sequential dehydrogenation to form the photostable m/z 300 ion. Thus, fragmentation patterns and fragmentation pathways must be compared for the acenaphthylene aggregate ion, the cyclobutadiacenaphthylene ion, and the biacenaphthenylidene ion.

Photofragmentation Patterns

All three m/z 304 ions photodissociated to form m/z 152 as the most abundant fragment ion (Figure 5-18). However, the ratio of the m/z 152 ion to the m/z 153 ion was not consistent. If the m/z 153 ion was purely due to ^{13}C and ^{2}H isotopes, the abundance of m/z 153 should be 13% of the abundance of the m/z 152 ion. For the acenaphthylene aggregate, the m/z 153 abundance is 19% of m/z 152, suggesting charge transfer as the major route for m/z 153 ion formation. The abundance of m/z 153 is much greater for the two aggregate candidates: 31% for cyclobutadiacenaphthylene and 60% for biacenaphthenylidene. Thus, formation of the m/z 153 ion may involve m/z 304 fragmentation or m/z 152 hydrogenation in these cases. Although the mechanism of m/z 153 ion formation is unclear, cyclobutadiacenaphthylene appears to be the better match for the acenaphthylene aggregate based on the ratio of m/z 153 to m/z 152.

The acenaphthylene aggregate, cyclobutadiacenaphthylene, and biacenaphthenylidene ions lost a maximum of four hydrogens during 5.0 s of lamp irradiation (Figure 5-19). However, fragmentation patterns for the three m/z 304 ions differed in relative intensities. The most abundant dehydrogenated photoproduct of the acenaphthylene aggregate was the m/z 301 ion. Photolysis of cyclobutadiacenaphthylene

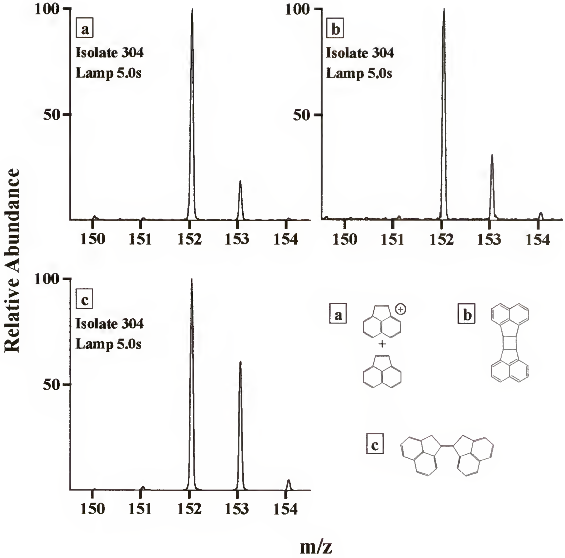

$$304 \xrightarrow{h\nu} 154, 153, 152, 151, 150$$

Figure 5-18. Photolysis of the acenaphthylene aggregate, cyclobutadiacenaphthylene, and biacenaphthenylidene cations (m/z 150-154 range). All mass spectra are after Xe lamp irradiation (5.0 s) of the isolated m/z 304 ion. A) FT-ICR mass spectrum of irradiated acenaphthylene aggregate cation. B) FT-ICR mass spectrum of irradiated cyclobutadiacenaphthylene cation. C) FT-ICR mass spectrum of irradiated biacenaphthenylidene cation.

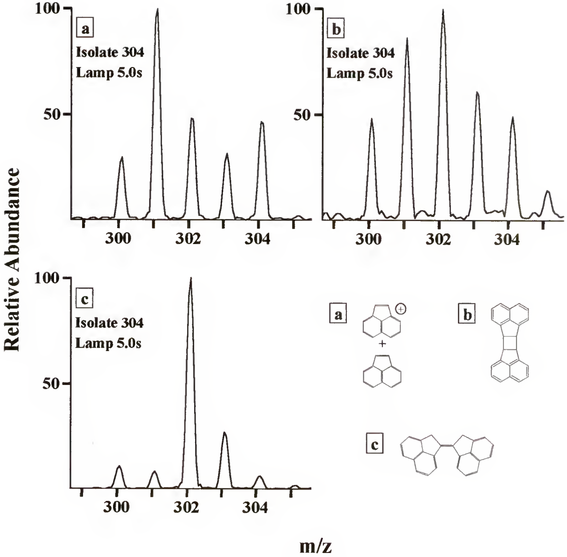

$$304 \xrightarrow{h\nu} 303, 302, 301, 300$$

Figure 5-19. Photolysis of the acenaphthylene aggregate, cyclobutadiacenaphthylene, and biacenaphthenylidene cations (m/z 299-305 range). All mass spectra are after Xe lamp irradiation (5.0 s) of the isolated m/z 304 ion. A) FT-ICR mass spectrum of irradiated acenaphthylene aggregate cation. B) FT-ICR mass spectrum of irradiated cyclobutadiacenaphthylene cation. C) FT-ICR mass spectrum of irradiated biacenaphthenylidene cation.

and biacenaphthenylidene cations yielded the m/z 302 ion as the most abundant dehydrogenated species. For cyclobutadiacenaphthylene, the m/z 301 ion is only 13% less than the m/z 302 ion; however, for biacenaphthenylidene, the m/z 301 ion is 91% less than the m/z 302 ion. Moreover, for the acenaphthylene aggregate and cyclobutadiacenaphthylene cations, the abundance of m/z 301 is greater than that of m/z 300. Photolysis of the biacenaphthenylidene cation yields more m/z 300 than m/z 301. Thus, based on the relative intensities of the dehydrogenated photoproducts, cyclobutadiacenaphthylene appears to be a better fit for the acenaphthylene aggregate.

Photofragmentation Pathway

Relative intensities in fragmentation patterns may fluctuate due to variations in lamp power. Therefore, a more accurate description of photolysis behavior is the fragmentation pathway, which should be independent of lamp power. The acenaphthylene aggregate ion lost four hydrogens sequentially during lamp photolysis. For example, ejection of m/z 302 during photolysis of m/z 304 eliminated the m/z 301 and m/z 300 ions (Figure 5-20). Photolysis of the cyclobutadiacenaphthylene cation also yielded sequential dehydrogenation: ejection of m/z 302 during irradiation removed m/z 301 and m/z 300. Dehydrogenation of biacenaphthenylidene, however, did not proceed sequentially. Ejection of the m/z 302 ion during photolysis removed the m/z 301 ion, but did not eliminate the m/z 300 ion. Therefore, biacenaphthenylidene is not a good match for the acenaphthylene aggregate.

Aggregate Formation and Cyclobutadiacenaphthylene Dehydrogenation

Based on fragmentation patterns and pathways, cyclobutadiacenaphthylene appears to be a good match for the acenaphthylene aggregate. Formation of the

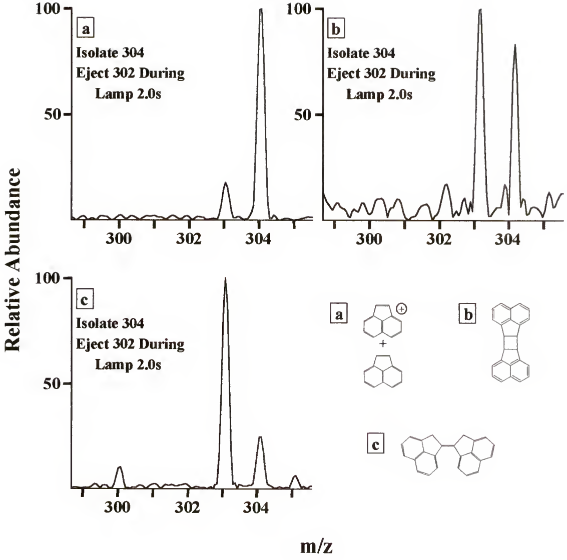

Figure 5-20. Fragmentation pathways for the acenaphthylene aggregate, cyclobutadiacenaphthylene, and biacenaphthenylidene cations (m/z 299-305 range). All mass spectra are after Xe lamp irradiation (2.0 s) of the isolated m/z 304 ion with simultaneous ejection of the m/z 302 ion. A) FT-ICR mass spectrum for the acenaphthylene aggregate cation. B) FT-ICR mass spectrum for the cyclobutadiacenaphthylene cation. C) FT-ICR mass spectrum for the biacenaphthenylidene cation.

cyclobutadiacenaphthylene structure from an acenaphthylene ion and an acenaphthylene neutral seems reasonable in that there is no hydrogen rearrangement required. Removal of four hydrogens from the four-membered ring to form the m/z 300 ion also seems reasonable. The resulting structure is similar to the photostable biphenylene cation. Furthermore, it seems likely that removal of one hydrogen from the four-membered ring of cyclobutadiacenaphthylene would prevent dissociation to the m/z 152 ion, as was observed for the acenaphthylene aggregate ion.

However, in the case of the acenaphthylene aggregate, the m/z 303 and m/z 302 ions were formed by combination of acenaphthylene fragment ions (m/z 151 and m/z 150) with the acenaphthylene neutral molecule. The predicted structures of the m/z 151 and m/z 150 ions require hydrogen abstraction from one six-membered ring of acenaphthylene. Consequently, the m/z 303 ion formed from the m/z 151 ion and the acenaphthylene neutral would have four hydrogens attached to the four-membered ring (Figure 5-21). Subsequent removal of three hydrogens from the four-membered ring to form the m/z 300 ion leaves one hydrogen on the four-membered ring. This structure seems unlikely to be photostable.

Thus, explanation of the photostability of the m/z 300 ion requires alternate dehydrogenation mechanisms: hydrogen rearrangement within the m/z 303 ion, or hydrogen abstraction from the six-membered ring. Formation of the m/z 303 ion from the acenaphthylene neutral and the m/z 151 fragment ion results in an empty position on one six-membered ring. Although the four-membered ring and six-membered rings are separated by one carbon position, hydrogen transfer from the four-membered ring to the empty position may be possible (Figure 5-22). This rearrangement mechanism

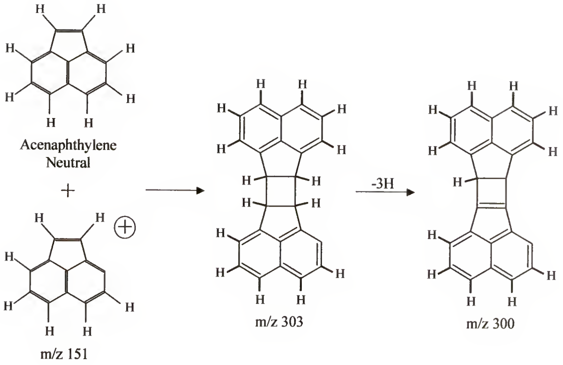

Figure 5-21. Formation and dehydrogenation route for the m/z 303 cation, assuming hydrogens are removed only from the four-membered ring.

would leave three abstractable hydrogens attached to the four-membered ring. However, formation of the m/z 302 ion from the acenaphthylene neutral and the m/z 150 fragment ion leaves two empty positions on one six-membered ring. It is unlikely that two hydrogens could transfer from the same side of the four-membered ring to fill these empty positions on the six-membered ring. Consequently, this hydrogen rearrangement mechanism is unreasonable.

The predicted dehydrogenation pathway for the acenaphthylene cation involved loss of hydrogens from the same six-membered ring. The dehydrogenation mechanism for the cyclobutadiacenaphthylene cation may also involve stripping hydrogens from one six-membered ring. However, this mechanism only accounts for the loss of three

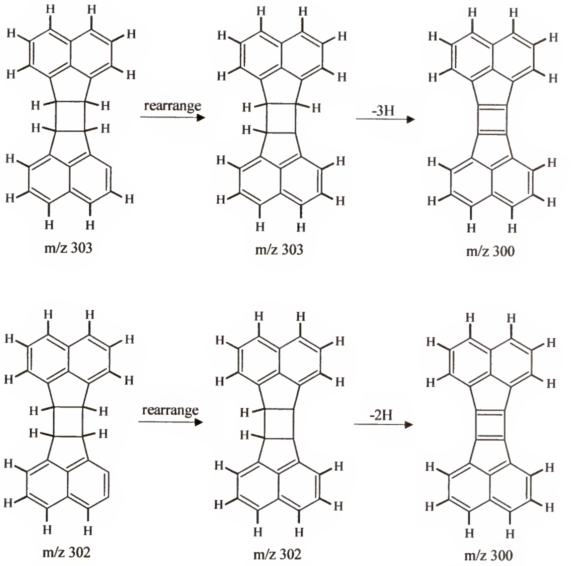

Figure 5-22. Possible dehydrogenation routes of the m/z 303 and m/z 302 ions following hydrogen rearrangement.

hydrogens. The fourth hydrogen may be removed from the position in the four-membered ring closest to the stripped six-membered ring, leaving a m/z 300 ion with one dehydrogenated quadrant (Figure 5-23). This mechanism would account for dehydrogenation of the m/z 303 and m/z 302 ions formed by aggregation of the acenaphthylene neutral with the m/z 151 ion and m/z 150 ion, respectively. However,

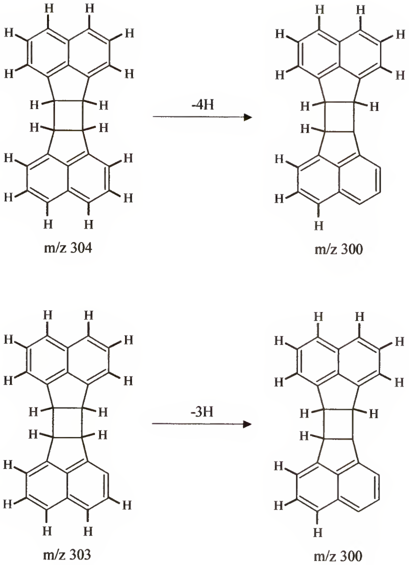

Figure 5-23. Possible dehydrogenation routes of the m/z 304 and m/z 303 ions assuming hydrogens are stripped from one quadrant of cyclobutadiacenaphthylene.

without calculated C-H bond energies for support, the accuracy of this mechanism remains questionable.

CHAPTER 6
2,3-BENZOFLUORENE

Background

The structure of the cata-condensed 2,3-benzofluorene ($C_{17}H_{12}$) consists of three aromatic six-membered rings and one five-membered ring (Figure 6-1). Although not fully conjugated, 2,3-benzofluorene is classified as a PAH due to the aromaticity of the six-membered rings. The "2,3" label refers to the positions in the fluorene molecule to which a benzenoid ring was added. For convenience, 2,3-benzofluorene will be referred to as benzofluorene from this point forward.

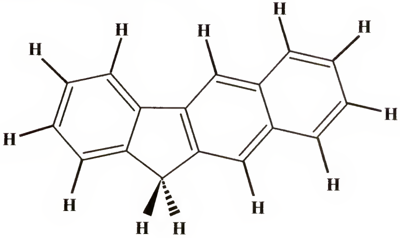

Figure 6-1. Structure of 2,3-benzofluorene.

Astrophysical Relevance

Although small, compact PAHs such as acenaphthylene exhibit photostability,[47] larger PAHs are more likely to be carriers of the UIR bands in the interstellar medium. Large PAHs contain a high density of vibrational states into which absorbed energy can be distributed. Thus, for large PAHs radiative IR emission should dominate dissociation as a relaxation mechanism. Because benzofluorene is a moderately-sized PAH containing a stabilizing pentagonal ring, it may contribute to the observed IR emission in the interstellar medium.

Previous Studies

In FT-ICR photodissociation experiments conducted by Ekern et al., most PAH cations losing acetylene units upon UV irradiation contained an exposed six-membered ring.[47] However, acetylene loss was observed from the fluorene cation ($C_{13}H_{10}^+$), in which both six-membered rings are fused directly to the central pentagonal ring.[47,52] The effect of additional rings on the acetylene loss fragmentation channel is of interest. Therefore, investigation of the photodissociation of the benzofluorene cation ($C_{17}H_{12}^+$) is a logical extension of the previous fluorene cation ($C_{13}H_{10}^+$) study.

Very few studies of benzofluorene have been conducted to date. Ion-molecule reactions involving the benzofluorene cation carbon skeleton (C_{17}^+) have previously been studied via FT-ICR mass spectrometry.[69] The C_{17}^+ ion was created by electron bombardment of perchlorinated benzofluorene ($C_{17}Cl_{12}$). However, since the most stable forms of C_n^+($n = 11$-20) species are monocyclic, the structure of C_{17}^+ is expected to be significantly different than the structure of $C_{17}H_{12}^+$. Fluorescence excitation and emission spectra for benzofluorene trapped in an argon matrix at 14 K were reported by Geigle and Hohlneicher.[70] The emission spectrum was dominated by bands at 795 cm^{-1} and 1369 cm^{-1}. The strongest bands in the excitation spectrum were at 712 cm^{-1} and 1376 cm^{-1}. Oscillator strengths for emission and excitation were 0.0060 and 0.0035, respectively.

DFT Calculations

Optimized geometries, fragmentation energies, and vibrational frequencies were calculated using the Gaussian 98 platform.[54] Hybrid density functional theory (B3LYP) was applied in conjunction with the 4-31G, 6-31G(d,p), or 6-311+G(d,p) basis set.

Optimized Geometries

Optimized geometries for the neutral and ionic ground states of benzofluorene were calculated with the 6-31G(d,p) basis set. The benzofluorene structure with labeled atom positions is shown in Figure 6-2. Numbered positions correspond to IUPAC numbering conventions. Letter designations are unique to this work.

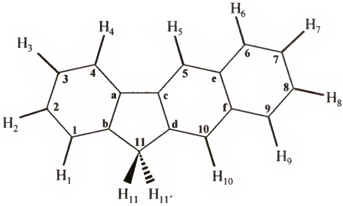

Figure 6-2. Structure and atom position labeling for benzofluorene.

Bond lengths and bond angles are presented in Table 6-1 and Table 6-2, respectively. For the benzofluorene neutral molecule, all hydrogens attached to the sp^2 hybridized carbons of the six-membered rings have a calculated carbon-hydrogen bond length of approximately 1.09 Å. The two hydrogens attached to the sp^3 hybridized carbon (C_{11}) in the five-membered ring have a slightly longer C-H bond length of 1.10 Å. All carbon-carbon bond lengths for the six-membered rings are approximately 1.40 ± 0.04 Å, indicating the delocalized double bond character of the C-C bonds in these rings.

Table 6-1. Calculated bond lengths (Å) at the B3LYP/6-31G(d,p) level of theory for neutral and cationic benzofluorene.

Bond	Neutral (Å)	Cation (Å)	Bond	Neutral (Å)	Cation (Å)
C_1-C_2	1.3989	1.4005	C_1-H_1	1.0870	1.0853
C_2-C_3	1.3994	1.4123	C_2-H_2	1.0861	1.0855
C_3-C_4	1.3954	1.3836	C_3-H_3	1.0861	1.0847
C_4-C_a	1.3972	1.4109	C_4-H_4	1.0864	1.0852
C_a-C_b	1.4102	1.4290	C_5-H_5	1.0872	1.0862
C_a-C_c	1.4682	1.4349	C_6-H_6	1.0870	1.0860
C_c-C_d	1.4315	1.4301	C_7-H_7	1.0861	1.0844
C_d-C_{11}	1.5168	1.5125	C_8-H_8	1.0860	1.0853
C_{11}-C_b	1.5162	1.5097	C_9-H_9	1.0871	1.0858
C_c-C_5	1.3772	1.4130	C_{10}-H_{10}	1.0878	1.0867
C_5-C_e	1.4206	1.4028	C_{11}-H_{11}	1.0981	1.0976
C_e-C_f	1.4373	1.4414	C_{11}-$H_{11'}$	1.0981	1.0976
C_f-C_{10}	1.4247	1.4376			
C_{10}-C_d	1.3702	1.3677			
C_e-C_6	1.4216	1.4271			
C_6-C_7	1.3764	1.3844			
C_7-C_8	1.4160	1.4040			
C_8-C_9	1.3771	1.4010			
C_9-C_f	1.4198	1.4002			

The C_b-C_{11} and C_d-C_{11} bonds in the five-membered ring have bond lengths of 1.52 Å, which is consistent with the expected single bonds involving the sp^3 hybridized C_{11} atom. Similarly, the C_a-C_c single bond in the five-membered ring has a bond length of 1.47 Å.

Carbon-hydrogen bond lengths in the benzofluorene radical cation are similar to those in neutral benzofluorene: 1.09 Å for hydrogens on sp^2 hybridized carbons and 1.10 Å for hydrogens on the sp^3 hybridized carbon. As in the neutral, all C-C bonds in the six-membered rings are calculated to be 1.40 ± 0.04 Å, indicating the expected π-bond

Table 6-2. Calculated bond angles (degrees) at the B3LYP/6-31G(d,p) level of theory for neutral and cationic benzofluorene.

Angle	Neutral	Cation
C_1-C_2-C_3	120.5	121.7
C_2-C_3-C_4	120.6	120.5
C_3-C_4-C_a	118.9	118.2
C_4-C_a-C_b	120.4	121.0
C_a-C_b-C_1	120.4	120.0
C_b-C_1-C_2	119.1	118.5
C_a-C_c-C_d	108.2	109.4
C_c-C_d-C_{11}	109.7	109.4
C_d-C_{11}-C_b	102.9	102.7
C_{11}-C_b-C_a	110.3	110.2
C_b-C_a-C_c	108.8	108.3
C_c-C_5-C_e	119.9	119.7
C_5-C_e-C_f	119.4	119.4
C_e-C_f-C_{10}	119.7	119.7
C_f-C_{10}-C_d	120.2	120.2
C_{10}-C_d-C_c	120.7	120.2
C_d-C_c-C_5	120.7	120.8
C_e-C_6-C_7	120.7	120.7
C_6-C_7-C_8	119.7	119.7
C_7-C_8-C_9	120.9	120.9
C_8-C_9-C_f	120.8	120.8
C_9-C_f-C_e	118.6	118.6
C_f-C_e-C_6	119.2	119.2

Angle	Neutral	Cation
H_1-C_1-C_2	120.1	120.2
H_2-C_2-C_3	119.7	119.0
H_3-C_3-C_4	119.7	120.1
H_4-C_4-C_a	120.8	121.1
H_5-C_5-C_e	119.8	119.8
H_6-C_6-C_7	120.4	120.4
H_7-C_7-C_8	120.0	120.0
H_8-C_8-C_9	119.4	119.4
H_9-C_9-C_f	119.5	119.5
H_{10}-C_{10}-C_d	121.2	121.2
H_{11}-C_{11}-C_b	111.9	111.9
$H_{11'}$-C_{11}-C_b	111.9	111.9
H_{11}-C_{11}-$H_{11'}$	106.4	106.5

character of the aromatic rings. Upon ionization, the C_c-C_5 bond length increases by 0.03 Å and the C_a-C_c bond length decreases by 0.04 Å. No significant change in bond length is observed for the remaining C-C bonds. Thus the overall structural effect of benzofluorene ionization is a slight distortion of the interior five-membered and six-membered rings.

Calculated atomic spin densities for the benzofluorene cation are presented in Table 6-3. In the radical cation, the largest atomic spin density resides on the C_5 atom. Significant spin density is also present on C_2, C_6, and C_8. Due to the lack of structural symmetry in benzofluorene, correlation between spin density and geometry change upon ionization is difficult.

Table 6-3. Calculated atomic spin densities at the B3LYP/6-31G(d,p) level of theory for the benzofluorene cation.

Atom	Spin Density	Atom	Spin Density
C_1	-0.060875	H_1	0.001826
C_2	0.164353	H_2	-0.006984
C_3	-0.020416	H_3	0.000306
C_4	0.047807	H_4	-0.002429
C_5	0.284727	H_5	-0.010907
C_6	0.226105	H_6	-0.00913
C_7	-0.086745	H_7	0.002534
C_8	0.179678	H_8	-0.007895
C_9	0.038863	H_9	-0.001701
C_{10}	0.101058	H_{10}	-0.003929
C_{11}	-0.005778	H_{11}	0.004499
C_a	0.067564	$H_{11'}$	0.004489
C_b	0.107644		
C_c	0.082807		
C_d	-0.045695		
C_e	-0.079735		
C_f	0.027956		

Sequential Hydrogen Loss

Hydrogen removal energies for the benzofluorene neutral and cation were calculated using the 6-31G(d,p) basis set and are presented in Table 6-4. In both cases, the easiest hydrogen to remove is one of the two hydrogens bonded to the sp^3 hybridized carbon (C_{11}) in the five-membered ring: 3.32 eV for the neutral and 2.60 eV for the cation. All other carbon-hydrogen bond energies were approximately 4.8 eV (45% higher) for the neutral and greater than 5 eV (96% higher) for the cation.

Table 6-4. Calculated carbon-hydrogen bond energies (eV) at the B3LYP/6-31G(d,p) level of theory for neutral and cationic benzofluorene.

	H_1	H_2	H_3	H_4	H_5	H_6	H_7	H_8	H_9	H_{10}	H_{11}	$H_{11'}$
Neutral	4.79	4.80	4.79	4.79	4.80	4.79	4.79	4.79	4.79	4.79	3.32	3.32
Cation	5.21	5.38	5.29	5.25	5.09	5.21	5.21	5.27	5.20	5.10	2.60	2.60

Energies for hydrogen removal from the benzofluorene cation and subsequent fragment ions are listed in Figure 6-3. After the removal of the first hydrogen from the five-membered ring to form the m/z 215 cation, removal of each of the remaining hydrogens requires approximately 4.90 eV. As such, there are eleven possible structures for the m/z 214 fragment ion. Due to the large number of calculations, the smaller, less expensive 4-31G basis set was used to calculate hydrogen removal energies from each possible m/z 214 fragment ion. Comparison of bond energies calculated using the 6-31G(d,p) basis set and those calculated using the 4-31G basis set yielded a maximum difference of only 0.04 eV. The carbon-hydrogen bond energies for each of the m/z 214 fragment ions will be divided into two groups for discussion: hydrogens removed from exterior rings and hydrogens removed from interior rings. Unfortunately, calculations for several C-H bond energies failed to converge. However, based on the observed trends in the m/z 214 cations, these bond energies are not expected to affect the lowest energy dehydrogenation routes.

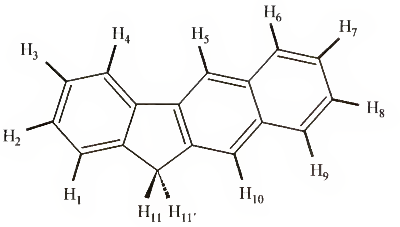

	H removed											
	H_1	H_2	H_3	H_4	H_5	H_6	H_7	H_8	H_9	H_{10}	H_{11}	$H_{11'}$
216	5.21	5.38	5.29	5.25	5.09	5.21	5.21	5.27	5.20	5.10	**2.60**	**2.60**
215 ($H_{11'}$)	**4.88**	**4.91**	**4.84**	**4.87**	**4.85**	**4.87**	**4.86**	**4.89**	**4.86**	**4.85**	**5.00**	
214 (H_1, $H_{11'}$)		**3.94**	4.56	X	6.42	6.57	6.62	6.60	6.67	6.52	5.81	
214 (H_2, $H_{11'}$)	**3.91**		**3.92**	4.97	X	6.41	649	6.40	6.49	6.40	6.34	
214 (H_3, $H_{11'}$)	4.58	**3.98**		**3.91**	6.30	6.62	6.69	6.65	6.70	6.35	6.47	
214 (H_4, $H_{11'}$)	X	5.01	**3.89**		6.26	X	6.43	6.42	6.47	6.34	**4.02**	
214 (H_5, $H_{11'}$)	6.45	X	6.30	6.29		5.95	6.23	6.55	5.48	**3.97**	**3.97**	
214 (H_6, $H_{11'}$)	6.58	6.45	6.60	X	5.93		**3.87**	4.84	5.48	5.35	6.57	
214 (H_7, $H_{11'}$)	6.64	6.54	6.68	6.44	6.22	**3.88**		**3.97**	4.49	6.45	6.54	
214 (H_8, $H_{11'}$)	6.58	6.41	6.61	6.40	6.50	4.81	**3.94**		**3.87**	X	6.58	
214 (H_9, $H_{11'}$)	6.69	6.54	6.69	6.49	5.47	5.49	4.49	**3.91**		5.86	6.54	
214 (H_{10}, $H_{11'}$)	6.55	6.47	6.35	6.37	**3.98**	5.37	6.46	X	5.88		5.85	
214 (H_{11}, $H_{11'}$)	5.67	6.23	6.30	**3.88**	**3.80**	6.42	6.38	6.45	6.38	5.68		

Figure 6-3. Calculated carbon-hydrogen bond energies (eV) for sequential hydrogen loss from the benzofluorene cation ($C_{17}H_{12}^+$, m/z 216). Nonconvergent bond energies are labeled with an "X".

Following hydrogen removal from one of the six-membered exterior rings of the m/z 215 cation, the hydrogen(s) adjacent to the removed hydrogen is (are) the next easiest to remove. For the m/z 214 cations formed by abstraction of H_2 (4.91 eV), H_3 (4.84 eV), H_7 (4.86 eV), or H_8 (4.89 eV) from the m/z 215 cation, the C-H bond energies of the two hydrogens directly adjacent to the removed hydrogen are between 3.87 eV and 3.98 eV. In each case, the fourth hydrogen on the same six-membered ring requires energies at least 13% higher (4.49 eV to 4.97 eV) for removal. All other hydrogens in these m/z 214 cations have C-H bond energies at least 56% higher (6.22 eV to 6.70 eV).

After removal of H_1 (4.88 eV), H_6 (4.87 eV), or H_9 (4.86 eV) from the m/z 215 cation, carbon-hydrogen bond energies for the single hydrogen directly adjacent to the abstracted hydrogen are between 3.87eV and 3.94 eV. All other hydrogens in these m/z 214 cations have C-H bond energies at least 14% higher (4.49 eV to 6.69 eV). Abstraction of H_4 (4.87 eV) from the m/z 215 cation affects two of the remaining C-H bond energies. As expected, the hydrogen adjacent to the removed hydrogen has a low C-H bond energy of 3.89 eV. However, the hydrogen on the five-membered ring also has a low C-H bond energy of 4.02 eV. This additional effect may be due to the close proximity and orientation of H_4 relative to the five-membered ring. All other C-H bond energies in this m/z 214 cation are at least 25% higher (5.01 eV to 6.47 eV).

Removal of one of the hydrogens (H_5 or H_{10}) attached to the interior six-membered ring results in a low C-H bond energy for the other hydrogen attached to the same ring. After abstraction of H_{10} (4.85 eV) from the m/z 215 cation, the C-H bond energy of H_5 is 3.98 eV. The energies of the other C-H bonds are at least 35% higher (5.37 eV to 6.55 eV). Similarly, removal of H_5 from the m/z 215 cation yields a C-H bond energy of 3.97 eV for H_{10} in the resulting m/z 214 cation. However, as in the case of H_4 abstraction, the hydrogen attached to the five-membered ring (H_{11}) also exhibits a low C-H bond energy (3.97 eV) when H_5 is removed. All other C-H bond energies are at least 38% higher (5.48 eV to 6.55 eV). Conversely, removal of H_{11} from the five-membered ring in the 215 cation, yields H_4 and H_5 bond energies of 3.88 eV and 3.80 eV, respectively. All other C-H bond energies are at least 46% higher (5.67 eV to 6.42 eV). Again, the relationship between H_5 and H_{11} and between H_4 and H_{11} is most likely due to the close proximity and orientation of H_4 and H_5 relative to the five-membered ring.

The multiple possibilities for hydrogen removal from both the m/z 215 cation and the m/z 214 cation prevent identification of structures for the m/z 214 and m/z 213 ions. An overall pathway for sequential hydrogen loss cannot be predicted based on the calculated C-H bond energies.

Carbon Fragment Loss

Based on earlier PAH photofragmentation studies,[47,52] acetylene (C_2H_2) removal is also a probable photofragmentation route for benzofluorene. For the fluorene cation ($C_{13}H_{10}^+$), Dibben et al. observed loss of acetylene following the removal of one hydrogen from the parent ion.[52] Because a similar photofragmentation route was observed for the benzofluorene cation, energies for acetylene loss were calculated for the m/z 215 fragment ion instead of the m/z 216 parent ion. In benzofluorene, acetylene loss can occur only from the exterior six-membered rings. Energies required for acetylene removal from each of these six positions were calculated at the B3LYP/4-31G level of theory and are presented in Table 6-5.

Table 6-5. Energies (eV) required for acetylene removal from the m/z 215 fragment ion calculated at the B3LYP/4-31G level of theory.

Acetylene Position	Energy (eV)	Acetylene Position	Energy (eV)
$H_1C_1C_2H_2$	5.59	$H_6C_6C_7H_7$	5.40
$H_2C_2C_3H_3$	6.35	$H_7C_7C_8H_8$	5.40
$H_3C_3C_4H_4$	5.59	$H_8C_8C_9H_9$	5.40

The three acetylene units furthest from the five-membered ring ($H_6C_6C_7H_7$, $H_7C_7C_8H_8$, and $H_8C_8C_9H_9$) are the easiest to abstract since they have the lowest removal energy (5.40 eV). The two acetylene units directly attached to the five-membered ring ($H_1C_1C_2H_2$ and $H_3C_3C_4H_4$) have slightly higher removal energies (5.59 eV). Thus, all five of these acetylene units are equally likely to be removed from the m/z 215 fragment ion. Since the energy required for removal of the sixth acetylene unit ($H_2C_2C_3H_3$) is 18% higher (6.35 eV), its removal is not expected to be a major photofragmentation route.

FT-ICR Photodissociation Studies

Experimental Conditions

The vapor pressure of benzofluorene (216 amu) was too low for introduction via a leak valve. As such, solid benzofluorene was vaporized using a resistively heated probe. The benzofluorene solid was loaded into a glass capillary tube, which was then mounted on the tip of a resistively heated stainless steel rod. The optimal probe temperature for benzofluorene vaporization was 80°C. Background pressure for these experiments was 5×10^{-9} Torr. Vaporization of benzofluorene at 80°C resulted in an operating pressure of 7×10^{-9} Torr, which corresponds to approximately 6×10^{7} benzofluorene molecules/cm^3. Gas-phase benzofluorene was ionized by electron ionization. Based on the calculated ground-state energies of the benzofluorene neutral and cation, the estimated ionization potential of benzofluorene is 6.97 eV. The optimal filament current for electron generation was 1.7 A. Electrons were accelerated towards the cell during the 30 ms ionization pulse by a repeller plate voltage of -18 V.

Results and Discussion

Electron bombardment of neutral benzofluorene (Figure 6-4) yielded the m/z 216 parent ion, ^{13}C isotope ions (m/z 217, m/z 218), dehydrogenated fragment ions (m/z 211-215), and ring-fragmented ions (m/z 185-190, m/z 163). Prior to lamp irradiation, the m/z 216 parent ion was isolated using a SWIFT waveform. Irradiation of the isolated m/z 216 ion with light from the xenon arc lamp (250 nm to 1100 nm) yielded two fragmentation routes: dehydrogenation to form the m/z 215, 214, and 213 ions, and carbon loss to form the m/z 189, 188, 187, and 163 ions.

The relative abundances of the major benzofluorene fragment ions (m/z 216, 215, 214, 213, and 189) as a function of irradiation time are shown in Figure 6-5. The relative abundance of the m/z 216 parent cation rapidly decreased to 3% during 3.0 s of irradiation. The abundance of m/z 215 initially increased proportionately with m/z 216 loss, reaching a maximum relative abundance of 80% at 1.7 s of lamp irradiation. After 1.7 s, the decrease of the m/z 215 ion was accompanied by an increase in the abundances of the m/z 213 and m/z 189 ions, indicating that the m/z 213 and m/z 189 ions were fragmentation products of m/z 215. The m/z 214 fragment exhibited a slow, relatively small increase over the 10.0 s irradiation period, and thus could not be correlated exclusively with either the m/z 216 parent ion or the m/z 215 fragment ion.

Hydrogen loss

During lamp irradiation, the m/z 216 parent ion lost a maximum of three hydrogen atoms. To distinguish between single and double hydrogen loss pathways,

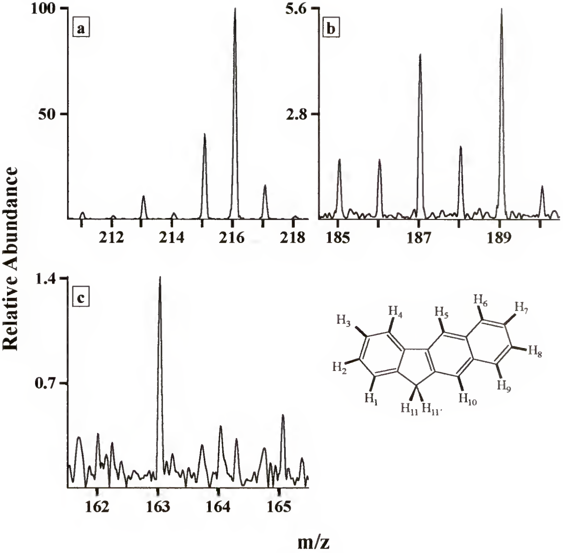

benzofluorene $\xrightarrow{\text{e- impact}}$ **215, 214, 213, 212, 211**

190, 189, 188, 187, 186, 185, 163

Figure 6-4. Electron ionization mass spectrum of benzofluorene ($C_{17}H_{12}$). A) FT-ICR mass spectrum in the m/z 211-218 range. B) FT-ICR mass spectrum in the m/z 185-190 range. C) FT-ICR mass spectrum in the m/z 161-165 range.

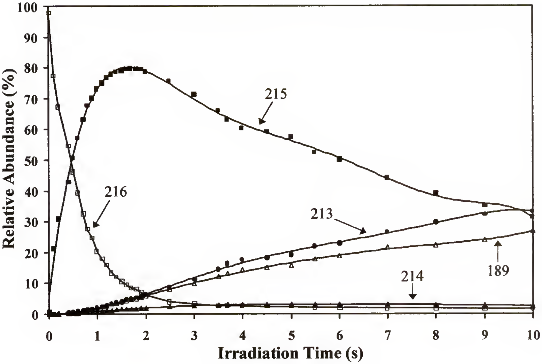

Figure 6-5. Relative abundance (%) of the m/z 216 parent ion and the m/z 215, 214, 213, and 189 fragment ions as a function of irradiation time (s).

specific ions were ejected during lamp irradiation. Ejection of the m/z 215 ion during 5.0 s of lamp irradiation resulted in a 60% reduction of m/z 214 (Figure 6-6). Thus, the predominant pathway for the formation of m/z 214 is single hydrogen loss from m/z 215. However, because 40% of the m/z 214 ion remained after ejection of m/z 215, double hydrogen loss from the m/z 216 parent ion is also a significant pathway for m/z 214 formation. Ejection of m/z 215 eliminated the m/z 213 ion; however, ejection of the m/z 214 ion had no significant effect on m/z 213. Thus, the pathway for m/z 213 formation must involve double hydrogen loss from m/z 215 rather than single hydrogen loss from m/z 214.

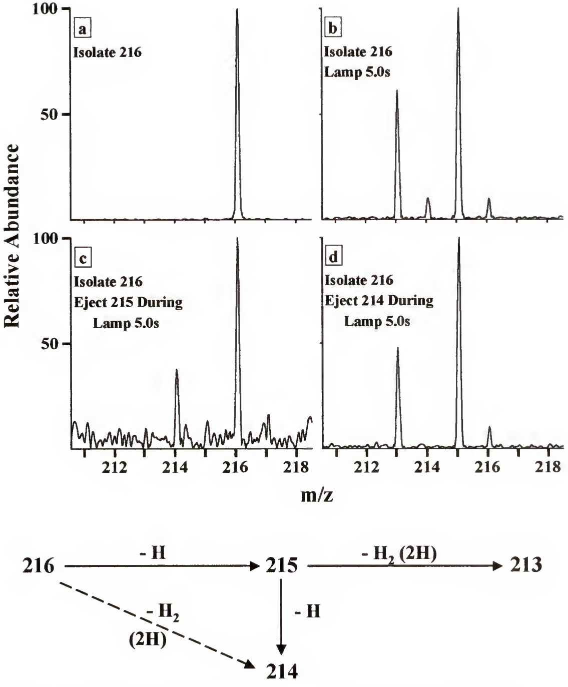

Figure 6-6. Dehydrogenation of the benzofluorene cation (m/z 216). Solid arrows represent primary pathways. The dashed arrow represents a secondary pathway. A) FT-ICR mass spectrum of isolated m/z 216. B) FT-ICR mass spectrum after Xe lamp irradiation (5.0 s). C) FT-ICR mass spectrum after Xe lamp irradiation (5.0 s) with simultaneous ejection of m/z 215. D) FT-ICR mass spectrum after Xe lamp irradiation (5.0 s) with simultaneous ejection of m/z 214.

Isolation and subsequent photolysis of the m/z 215 ion yielded both the m/z 214 and m/z 213 ions (Figure 6-7). Ejection of m/z 214 during photolysis yielded no significant m/z 213 reduction, confirming that m/z 213 is formed by double hydrogen loss from m/z 215, not single hydrogen loss from m/z 214. The abundance of the m/z 214 ion obtained by lamp photolysis was too small to allow subsequent isolation and photolysis. Isolation and subsequent photolysis of the m/z 213 ion yielded no further photoproducts (Figure 6-8).

Acetylene loss

Irradiation of the m/z 216 parent ion also yielded ions of mz 190, 189, 188, 187, and 163, indicating loss of carbons as well as hydrogens (Figure 6-9). The ions in the m/z 190-187 range correspond to the loss of two carbons and two to five hydrogens from the m/z 216 parent ion. The m/z 163 ion corresponds to the loss of four carbons and five hydrogens. As reported in earlier PAH photofragmentation studies,[47,52] such carbon loss most likely occurs as the loss of acetylene (C_2H_2, m/z 26) units. Due to limitations of the mass spectrometer, the low mass range needed for acetylene ion observation was unattainable. The loss of acetylene was therefore monitored as a function of the larger fragment ions.

The predominant fragment ion in the m/z 187-190 region was the m/z 189 ion, which corresponds to the loss of two carbons and three hydrogens from m/z 216. Ejection of the m/z 215 ion during lamp irradiation eliminated the m/z 189, 188, and 187 ions, indicating that these fragment ions are photolysis products of the m/z 215 ion (Figure 6-10). Because the m/z 190 fragment ion remained, the formation pathway of m/z 190 involves acetylene loss from the m/z 216 parent ion. Similarly, the m/z 189

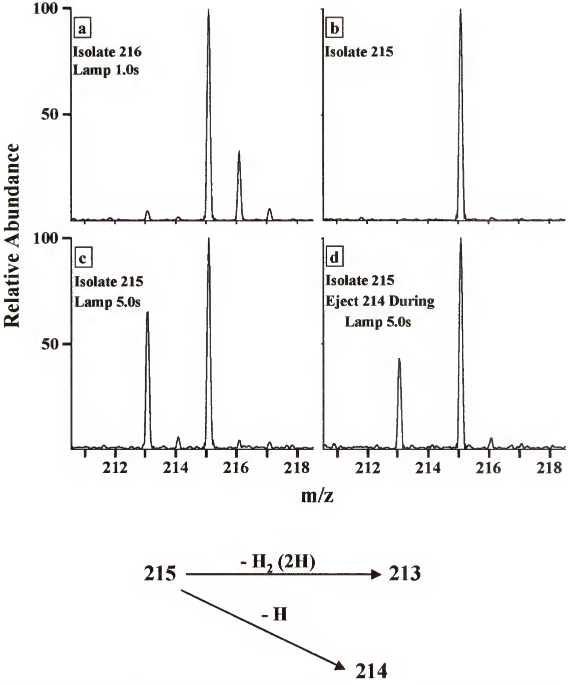

Figure 6-7. Dehydrogenation pathway for the m/z 215 fragment ion. A) FT-ICR mass spectrum after Xe lamp irradiation (1.0 s) of isolated m/z 216. B) FT-ICR mass spectrum of isolated m/z 215. C) FT-ICR mass spectrum after Xe lamp irradiation (5.0 s) of m/z 215. D) FT-ICR mass spectrum after Xe lamp irradiation (5.0 s) of m/z 215 with simultaneous ejection of m/z 214.

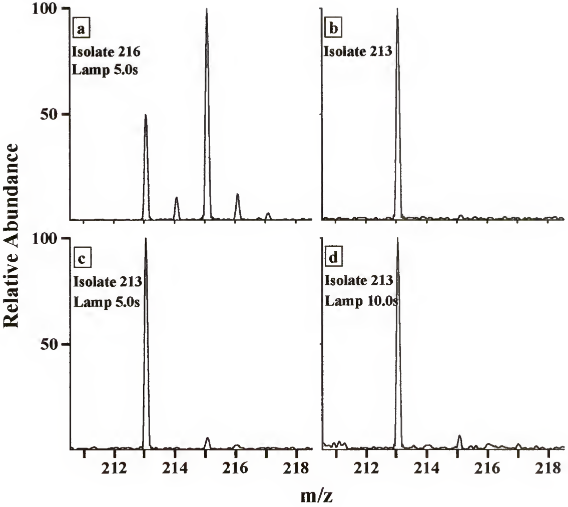

$$213 \xrightarrow{h\nu} X$$

Figure 6-8. Irradiation of the isolated m/z 213 fragment ion. A) FT-ICR mass spectrum after Xe lamp irradiation (5.0 s) of isolated m/z 216. B) FT-ICR mass spectrum after isolation of m/z 213. C) FT-ICR mass spectrum after Xe lamp irradiation (5.0 s) of m/z 213. D) FT-ICR mass spectrum after Xe lamp irradiation (10.0 s) of m/z 213.

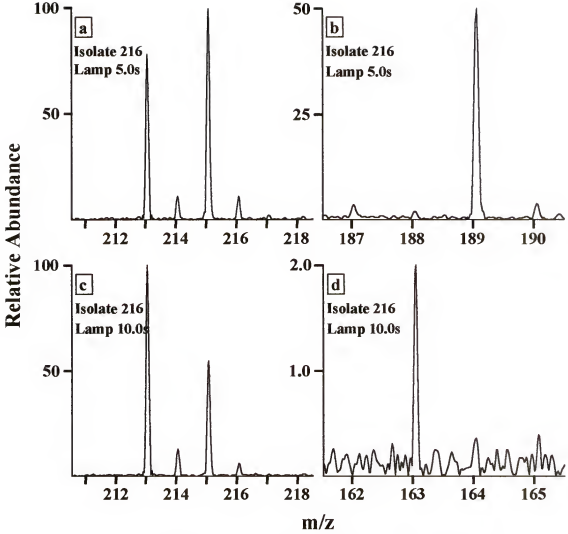

$$216 \xrightarrow{h\nu} 190, 189, 188, 187, 163$$

Figure 6-9. Photofragmentation of the benzofluorene cation (m/z 216). A) FT-ICR mass spectrum after Xe lamp irradiation (5.0 s) of isolated m/z 216 (m/z 211-218 range). B) FT-ICR mass spectrum after Xe lamp irradiation (5.0 s) of isolated m/z 216 (m/z 187-190 range). C) FT-ICR mass spectrum after Xe lamp irradiation (10.0 s) of isolated m/z 216 (m/z 211-218 range). D) FT-ICR mass spectrum after Xe lamp irradiation (10.0 s) of isolated m/z 216 (m/z 162-165 range).

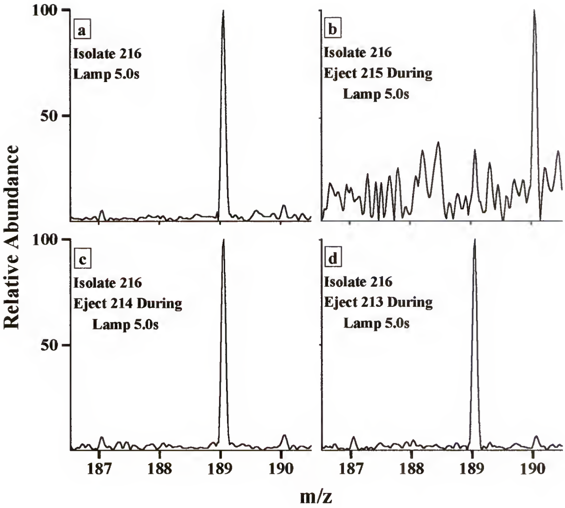

$$216 \xrightarrow{-C_2H_2} 190$$

$$215 \xrightarrow{-C_2H_2} 189$$

Figure 6-10. Acetylene loss pathways for the benzofluorene cation (m/z 216) and the m/z 215 fragment ion. A) FT-ICR mass spectrum of isolated m/z 216. B) FT-ICR mass spectrum after Xe lamp irradiation (5.0 s). C) FT-ICR mass spectrum after Xe lamp irradiation (5.0 s) with simultaneous ejection of m/z 214. D) FT-ICR mass spectrum after Xe lamp irradiation (5.0 s) with simultaneous ejection of m/z 213.

fragment ion is produced by acetylene loss from the m/z 215 fragment ion. Ejection of the m/z 214 and m/z 213 ions during photolysis had no effect on the m/z 188 and m/z 187 ions. Isolation and photolysis of the m/z 215 fragment ion produced the m/z 189 and m/z 187 fragment ions (Figure 6-11). Again, ejection of the m/z 214 and m/z 213 ions during lamp photolysis had no effect on the m/z 189 and m/z 187 ions, indicating that no acetylene loss occurs from either m/z 214 or m/z 213.

Isolation and photolysis of the m/z 189 fragment ion yielded the m/z 188 and m/z 187 ions (Figure 6-12). After 10.0 s of lamp irradiation, the abundances of m/z 188 and m/z 187 relative to m/z 189 were 2.7% and 7.3%, respectively. Due to significant charge transfer between the isolated m/z 189 ion and benzofluorene neutral molecules during long irradiation times, the source of the m/188 and m/z 187 ions was not immediately clear. However, ejection of the m/z 213-218 ions during photolysis had no effect on the m/z 188 and m/z 187 ions, leaving hydrogen loss from m/z 189 as the only possible pathway for m/z 188 and m/z 187 ion formation. Ejection of the m/z 188 ion during photolysis of m/z 189 eliminated the m/z 187 ion, indicating that the m/z 187 ion is formed by single hydrogen loss from the m/z 188 ion.

Photolysis of the isolated m/z 189 fragment ion also produced a small amount of the m/z 163 fragment ion (Figure 6-13). After 10.0 s of lamp irradiation, the abundance of m/z 163 was 3.0% relative to m/z 189. Ejection of the m/z 213-218 and m/z 188 ions during photolysis had no effect on the m/z 163 ion, leaving acetylene loss from the m/z 189 fragment ion as the only possible formation route for m/z 163.

The complete photofragmentation route for the benzofluorene cation is depicted in Figure 6-14. Percentages represent relative importance in cases where multiple

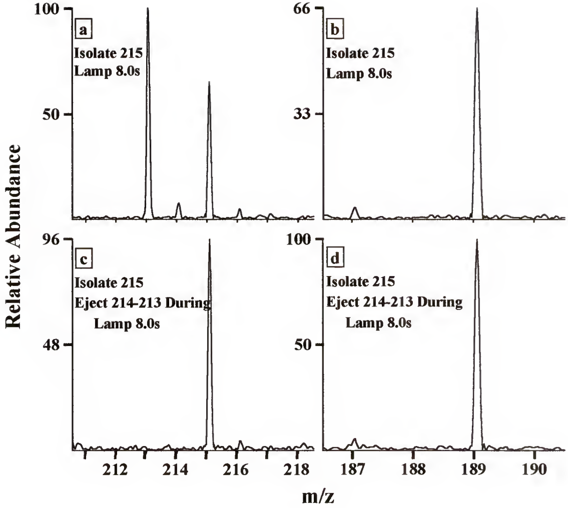

$$215 \xrightarrow{-C_2H_2} 189$$

Figure 6-11. Acetylene loss pathway for the m/z 215 fragment ion. A) FT-ICR mass spectrum after Xe lamp irradiation (8.0 s) of isolated m/z 215 (m/z 211-218 range). B) FT-ICR mass spectrum after Xe lamp irradiation (8.0 s) of isolated m/z 215 (m/z 187-190 range). C) FT-ICR mass spectrum after Xe lamp irradiation (8.0 s) of isolated m/z 215 with simultaneous ejection of m/z 214-213 (m/z 211-218 range). D) FT-ICR mass spectrum after Xe lamp irradiation (8.0 s) of isolated m/z 215 with simultaneous ejection of m/z 214-213 (m/z 187-190 range).

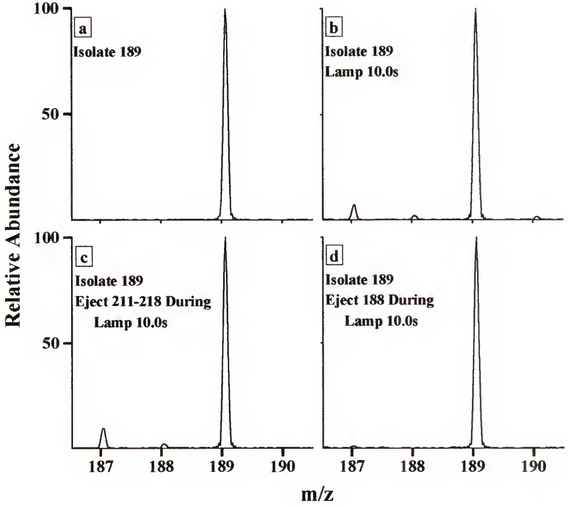

$$189 \xrightarrow{-\mathrm{H}} 188 \xrightarrow{-\mathrm{H}} 187$$

Figure 6-12. Dehydrogenation pathway for the m/z 189 fragment ion. A) FT-ICR mass spectrum of isolated m/z 189. B) FT-ICR mass spectrum after Xe lamp irradiation (10.0 s) of isolated m/z 189. C) FT-ICR mass spectrum after Xe lamp irradiation (10.0 s) of m/z 189 with simultaneous ejection of m/z 211-218. D) FT-ICR mass spectrum after Xe lamp irradiation (10.0 s) of m/z 189 with simultaneous ejection of m/z 188.

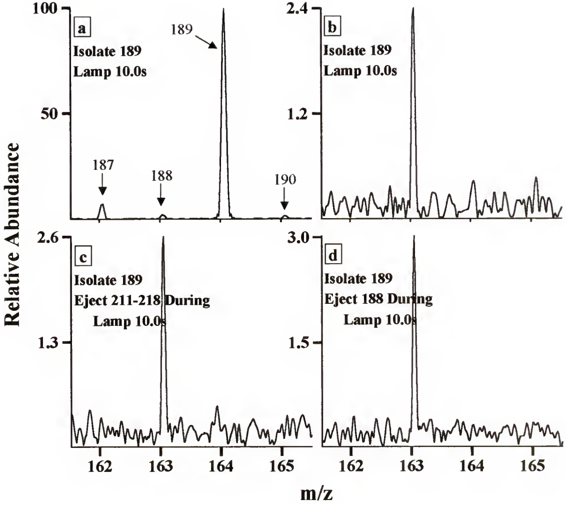

$$189 \xrightarrow{-\,C_2H_2} 163$$

Figure 6-13. Acetylene loss pathway for the m/z 189 fragment ion. A) FT-ICR mass spectrum after Xe lamp irradiation (10.0 s) of isolated m/z 189 (mz 187-190 range). B) FT-ICR mass spectrum after Xe lamp irradiation (10.0 s) of isolated m/z 189 (mz 162-165 range). C) FT-ICR mass spectrum after Xe lamp irradiation (10.0 s) of isolated m/z 189 with simultaneous ejection of m/z 211-218 (m/z 162-165 range). D) FT-ICR mass spectrum after Xe lamp irradiation (10.0 s) of isolated m/z 189 with simultaneous ejection of m/z 188 (m/z 162-165 range).

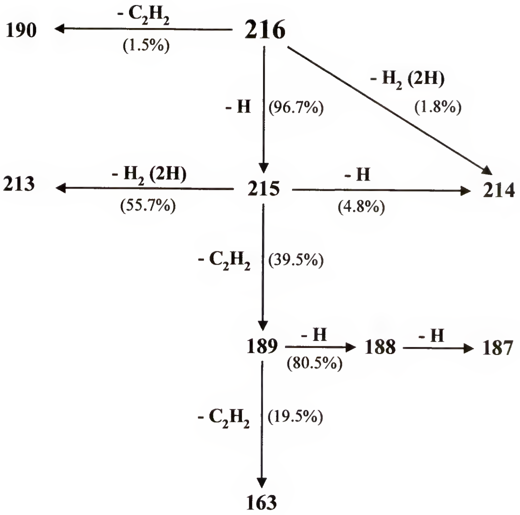

Figure 6-14. Overall observed photodissociation pathway for the benzofluorene cation (m/z 216). Percentages represent relative pathway importance.

pathways are available for photodissociation. Irradiation of the m/z 216 parent ion yields single hydrogen loss to form m/z 215 (96.5% yield), double hydrogen loss to form m/z 214 (1.8% yield), and acetylene loss to form m/z 190 (1.5% yield). Due to the low yields of m/z 214 and m/z 190, further fragmentation of these ions remains undetermined. The m/z 215 fragment ion photodissociates further to form m/z 214 via single hydrogen loss (4.8% yield), m/z 213 via double hydrogen loss (55.7% yield), and m/z 189 via acetylene loss (39.5% yield). The m/z 213 ion appears to be photostable. Again, the low yield of the m/z 214 ion prevents investigation of further dissociation pathways. Irradiation of the m/z 189 ion results in single hydrogen loss to form m/z 188 (80.5% yield) and acetylene loss to form m/z 163 (19.5% yield). The m/z 188 ion can undergo single hydrogen loss to form m/z 187. No fragments lower than m/z 163 were observed in the mass spectrum.

Comparison of observed and predicted dissociation pathways

The major observed photodissociation pathway for the m/z 216 parent ion was single hydrogen loss to form the m/z 215 fragment ion. Based on theoretical bond energy calculations, the removal of this first hydrogen from the five-membered ring requires 2.60 eV. Single hydrogen loss from the m/z 215 fragment ion to form m/z 214 was observed as a minor dissociation pathway (4.8% yield), which correlates well with the high predicted energy (~5 eV) required for this fragmentation route. The observed double hydrogen loss to form m/z 213 (55.7% yield) must therefore be more energetically favorable than single hydrogen loss. Unfortunately, methods for calculation of simultaneous hydrogen loss are quite complex and were not performed in this work. Nevertheless, if double hydrogen loss occurs as loss of an H_2 molecule, the two hydrogens removed most likely are attached to adjacent carbons. Such double hydrogen loss is therefore limited to one of the exterior six-membered rings.

The observed acetylene (C_2H_2) loss from the m/z 215 fragment ion to form the m/z 189 ion must occur from one of the exterior six-membered rings containing acetylene units. Calculated energies for acetylene loss were similar for all available acetylene units. However, removal of acetylene molecules furthest from the five-membered ring required slightly lower energies (5.40 eV) than those nearest the five-membered ring

(5.59 eV to 6.35 eV). Because double hydrogen loss from the m/z 215 ion yields the photostable m/z 213 ion, this simultaneous hydrogen loss must prevent the subsequent removal of acetylene. Therefore, the double hydrogen loss pathway and the acetylene loss pathway both must incorporate the six-membered ring furthest from the five-membered ring. However, since three acetylene positions are still equally likely, it remains undetermined which specific hydrogens or acetylene units are removed.

Photodissociation of the m/z 189 fragment ion occurs via sequential hydrogen loss to form the m/z 188 and m/z 187 ions. This sequential, rather than simultaneous hydrogen loss may indicate that the hydrogens removed are not on adjacent carbons. However, since the actual structure of m/z 189 is ambiguous, identification of the hydrogens lost is also not feasible.

Infrared and UV-visible Spectroscopy

Infrared and electronic absorption spectra were collected for benzofluorene neutral molecules and radical cations isolated in an argon matrix at 12 K. Neutral spectra were collected after codepositing benzofluorene vapor with argon on a CsI window. Benzofluorene cations were produced by electron bombardment of a benzofluorene/argon/CCl_4 mixture prior to deposition on a BaF_2 window.

Neutral Benzofluorene

The observed infrared absorption spectrum of neutral benzofluorene was compared to harmonic frequencies calculated at the B3LYP/6-311+G(d,p) and B3LYP/6-31G(d,p) levels of theory (Figure 6-15). To account for mode anharmonicities, the harmonic B3LYP/6-311+G(d,p) and B3LYP/6-31G(d,p) frequencies were scaled by

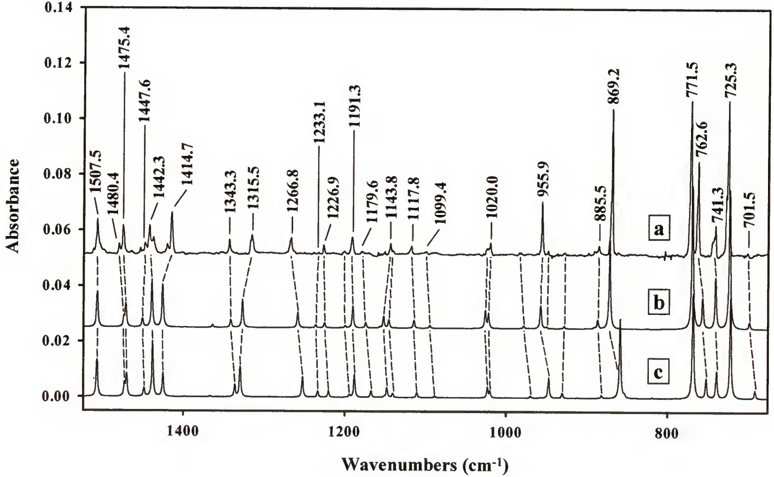

Figure 6-15. Experimental and calculated infrared absorption spectra (1525 cm^{-1} to 675 cm^{-1}) for neutral benzofluorene ($C_{17}H_{12}$). A) IR absorption spectrum of benzofluorene isolated in solid Ar at 12 K. B) IR absorption spectrum calculated at the B3LYP/6-311+G(d,p) level of theory (scaled by 0.98). C) IR absorption spectrum calculated at the B3LYP/6-31G(d,p) level of theory (scaled by 0.97).

factors of 0.98 and 0.97, respectively. Band frequencies, relative intensities, and mode descriptions for the observed and calculated spectra are listed in Table 6-6. Only bands with relative intensities greater than or equal to 0.2 are presented. Due to isolation of benzofluorene in different matrix sites, substructure was observed on all experimental bands. In each case, only the most intense sub-band is listed. Tabulated experimental band intensities were determined by summing the sub-band intensities.

Experimental vibrational frequencies were predicted reasonably well by both basis sets at the B3LYP level of theory. All observed bands were assignable to calculated frequencies. Differences between observed and calculated frequencies in the 400 cm^{-1} to 1700 cm^{-1} region were less than 12 cm^{-1} for the 6-311+G(d,p) basis set, and less than 15 cm^{-1} for the 6-31G(d,p) basis set. However, large shifts (30 cm^{-1} to 60 cm^{-1}) were observed for the C-H stretching modes in the 2900 cm^{-1} to 3200 cm^{-1} range for both levels of theory. These large energy shifts are due to the inability of a single scaling factor to account for anharmonicities associated with different vibrational modes. Nevertheless, because the single scaling factor adequately corrected the spectral range of interest, multiple scaling factors were not applied for different vibrational modes in this work. In terms of band position, the more extensive 6-311+G(d,p) basis set provided a slightly better fit than the 6-31G(d,p) basis set.

Both levels of theory predicted relative band intensities reasonably well. Tabulated experimental band intensities are relative to the intensity of the 771.5 cm^{-1} band. Similarly, intensities for the 769.6 cm^{-1} band predicted with the 6-311+G(d,p) basis set and the 768.5 cm^{-1} band calculated with the 6-31G(d,p) basis set were also scaled to 1.0. The integral intensities of the 769.6 cm^{-1} (6-311+G(d,p) basis set) and

Table 6-6. Calculated (B3LYP/6-311+G(d,p) and B3LYP/6-31G(d,p)) and observed (solid Ar) vibrational frequencies (cm^{-1}) for neutral benzofluorene. Relative intensities are given in parentheses. B3LYP/6-311+G(d,p) frequencies are scaled by a factor of 0.98. B3LYP/6-31G(d,p) frequencies are scaled by a factor of 0.97. *R* and *r* are stretching modes, α and β are in-plane bending modes, and τ and ε are out-of-plane vibrations.

Mode Description	6-311+G(d,p)	6-31G(d,p)	Experimental
τ(CCC)	203.1 (0.05)	205.8 (0.05)	
τ(CCC)	267.8 (0.07)	268.9 (0.08)	
τ(CCC)	305.0 (0.02)	302.3 (0.02)	
τ(CCC)	396.0 (0.07)	395.5 (0.04)	
τ(CCC)	426.3 (0.04)	427.4 (0.03)	
τ(CCC)	472.5 (0.33)	474.1 (0.31)	474.2 (0.30)
α(CCC)	538.1 (0.02)	532.7 (0.02)	
α(CCC)	570.4 (0.18)	564.9 (0.29)	571.4 (0.17)
α(CCC)	605.2 (0.06)	599.0 (0.09)	605.7 (0.04)
τ(CCC)	663.8 (0.02)	659.8 (0.02)	663.7 (0.03)
α(CCC)	698.8 (0.05)	691.8 (0.08)	701.5 (0.03)
ε(CCH) + τ(CCC)	723.5 (0.93)	722.2 (1.03)	725.3 (1.00)
ε(CCH) + τ(CCC)	740.9 (0.37)	739.4 (0.27)	741.3 (0.30)
ε(CCH) + τ(CCC)	756.8 (0.22)	752.2 (0.21)	762.6 (0.60)
ε(CCH) + τ(CCC)	769.6 (1.00)	768.5 (1.00)	771.5 (1.00)
ε(CCH) + τ(CCC)	872.0 (0.64)	858.8 (0.81)	869.2 (0.96)
ε(CCH) + τ(CCC)	886.8 (0.05)	881.7 (0.03)	885.5 (0.06)
ε(CCH) + τ(CCC)	957.5 (0.15)	947.2 (0.21)	955.9 (0.33)
α(CCC) + β(CCH)	1022.1 (0.11)	1020.1 (0.08)	1020.0 (0.07)
α(CCC) + β(CCH)	1026.0 (0.13)	1023.0 (0.11)	1024.1 (0.06)
α(CCC) + β(CCH)	1094 .7 (0.02)	1088.1 (0.02)	1099.4 (0.01)
α(CCC) + β(CCH)	1114.3 (0.06)	1110.3 (0.05)	1117.8 (0.05)
α(CCC) + β(CCH)	1145.6 (0.05)	1140.4 (0.04)	1143.8 (0.05)
β(CCH) + *R*(CC)	1152.1 (0.08)	1147.7 (0.10)	1150.6 (0.02)
β(CCH) + *R*(CC)	1174.2 (0.04)	1167.3 (0.07)	1179.6 (0.02)
β(CCH) + *R*(CC)	1190.1 (0.15)	1187.8 (0.24)	1191.3 (0.10)
β(CCH) + *R*(CC)	1225.3 (0.02)	1220.1 (0.07)	1226.9 (0.05)
β(CCH) + *R*(CC)	1236.3 (0.02)	1233.3 (0.06)	1233.1 (0.02)

Table 6-6. Continued.

Mode Description	6-311+G(d,p)	6-31G(d,p)	Experimental
β(CCH) + R(CC)	1258.3 (0.11)	1252.2 (0.21)	1266.8 (0.11)
R(CC) + β(CCH)	1326.8 (0.20)	1329.5 (0.29)	1315.5 (0.16)
β(CCH) + R(CC)	1341.4 (0.05)	1336.1 (0.13)	1343.3 (0.12)
R(CC) + β(CCH)	1363.9 (0.02)	1367.0 (0.02)	
ε(HC(sp^3)H) + R(CC)	1425.7 (0.31)	1425.0 (0.25)	1414.7 (0.26)
β(CCH) + R(CC) + ε(HC(sp^3)H)	1439.0 (0.35)	1437.9 (0.58)	1442.3 (0.22)
β(CCH) + R(CC)	1450.6 (0.06)	1448.3 (0.10)	1447.6 (0.04)
β(CCH) + R(CC)	1471.6 (0.17)	1470.4 (0.23)	1475.4 (0.17)
β(CCH) + R(CC)		1472.7 (0.16)	
R(CC) + β(CCH)	1507.4 (0.25)	1507.5 (0.36)	1507.5 (0.24)
R(CC)	1582.8 (0.02)	1583.2 (0.04)	
R(CC)	1589.2 (0.03)	1589.6 (0.03)	
R(CC)	1614.9 (0.03)	1615.2 (0.04)	
R(CC)	1619.0 (0.03)	1619.9 (0.08)	
R(CC)	1642.0 (0.06)	1641.1 (0.10)	1645.2 (0.02)
R(C(sp^3)H)	2961.7 (0.36)	2946.8 (0.63)	2917.4 (0.15)
R(C(sp^3)H)	2985.6 (0.16)	2974.2 (0.41)	2944.6 (0.10)
r(CH)	3094.2 (0.34)	3080.3 (0.31)	3029.0 (0.44)
r(CH)	3096.8 (0.03)	3083.4 (0.48)	3032.0
r(CH)	3099.6 (0.02)	3085.2 (0.53)	
r(CH)	3111.7 (0.96)	3101.1 (1.79)	3065.7
r(CH)	3123.8 (1.27)	3113.3 (2.42)	3071.0 (1.10)

768.5 cm^{-1} (6-31G(d,p) basis set) bands were 41.9 km/mol and 27.8 km/mol, respectively. Relative intensities for the observed 3029.0 cm^{-1} and 3071.0 cm^{-1} bands include the intensities of the 3032.0 cm^{-1} and 3065.7 cm^{-1} bands. As expected for neutral PAH molecules, the C-H out-of-plane bending modes in the 700 cm^{-1} to 1000 cm^{-1} range were stronger than the C-C stretches and C-H in-plane bends in the 1000 cm^{-1} to 1650 cm^{-1} region. A slightly better fit was observed for relative intensities calculated at the B3LYP/6-311+G(d,p) level of theory.

The electronic absorption spectrum for benzofluorene neutral is presented in Figure 6-16. Transitions were assigned by comparing observed absorption bands to vertical excitation energies and oscillator strengths (*f*) calculated via time-dependent density functional theory (TDDFT) with the BLYP/6-31++G(d,p) functional/basis set (Table 6-7). Because TDDFT underestimates excitation energies to high-lying excited states, assignments of transitions to excited states above the fourth excited state (S_4) are tentative. Oscillator strengths for experimental bands were estimated by comparing infrared and UV absorption bands assigned to the benzofluorene neutral molecule. Because both IR and UV-visible spectra were recorded for the same matrix, the integral intensity of the observed IR bands was related to the molar absorptivity of bands in the UV-visible region. The estimated molar absorptivity of the observed UV bands was then used to calculate oscillator strengths for each electronic transition.

Table 6-7. Calculated (TDDFT BLYP/6-31++G(d,p)) and observed (solid Ar) vertical excitation energies (eV) and oscillator strengths for neutral benzofluorene.

	Calculated		**Experimental**		
Transition	**ω (eV)**	***f***	**λ (nm)**	**ω (eV)**	***f***
$S_1(^1A') \leftarrow S_0(^1A')$	3.53	0.124	337.3	3.68	0.013
$S_2(^1A') \leftarrow S_0(^1A')$	3.61	0.020	322.2	3.85	0.011
$S_3(^1A') \leftarrow S_0(^1A')$	4.04	0.125	312.2	3.97	0.056
$S_4(^1A') \leftarrow S_0(^1A')$	4.15	0.037	298.5	4.15	0.041
$S_5(^1A') \leftarrow S_0(^1A')$	4.38	0.508	259.4	4.78	0.778
$S_6(^1A') \leftarrow S_0(^1A')$	4.46	0.047			
$S_7(^1A'') \leftarrow S_0(^1A')$	4.52	0.002			
$S_8(^1A') \leftarrow S_0(^1A')$	4.54	0.066	250.3	4.95	0.419
$S_9(^1A'') \leftarrow S_0(^1A')$	4.66	0.000			

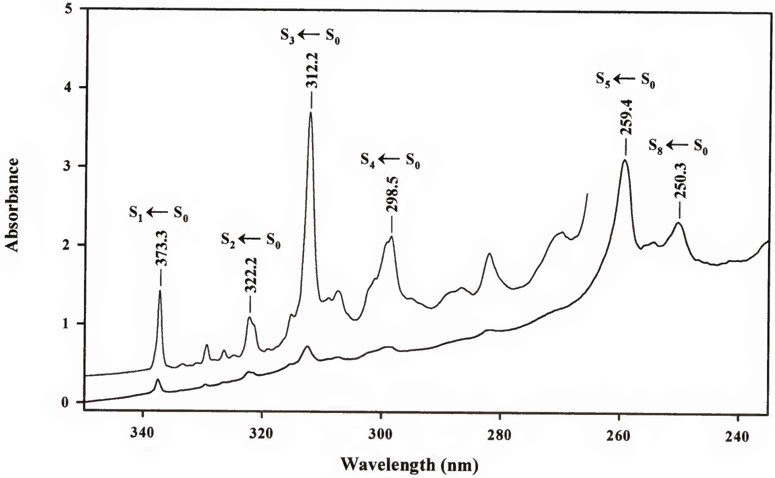

Figure 6-16. Electronic absorption spectrum (350 nm to 235 nm) of neutral benzofluorene isolated in solid Ar at 12 K. Assigned transitions correspond to vertical excitation energies calculated at the BLYP/6-31++G(d,p) level of theory.

For neutral benzofluorene, the strong infrared absorption observed at 869.2 $\mathrm{cm^{-1}}$ was used to calculate oscillator strengths in the electronic spectrum (Figure 6-17). The molar absorptivity (ε_{IR}) for this band was estimated from the predicted integral intensity (I) and the observed full-width at half-maximum ($\Delta\nu_{1/2}$):

$$I = 2.303\varepsilon_{IR}\Delta\nu_{1/2}$$

For the observed 869.2 $\mathrm{cm^{-1}}$ band, the closest calculated frequency is 872.0 $\mathrm{cm^{-1}}$, which has a predicted integral intensity of 27 km/mol. The $\Delta\nu_{1/2}$ for the observed 869.2 $\mathrm{cm^{-1}}$ band is 2.2 $\mathrm{cm^{-1}}$. The estimated ε_{IR} is therefore 530 $\mathrm{M^{-1}cm^{-1}}$.

Because the infrared and electronic absorption spectra were recorded for the same matrix, the sample concentration (c) and pathlength (l) are identical for each absorption:

$$A_{UV} = (\varepsilon_{UV})(c)(l) \qquad\qquad A_{IR} = (\varepsilon_{IR})(c)(l)$$

$$\varepsilon_{UV} = (A_{UV}/A_{IR})\varepsilon_{IR}$$

Therefore, the molar absorptivity for a UV-visible band can be calculated based on the relative IR and UV-visible band absorbances (A) recorded for the same matrix. For the 869.2 $\mathrm{cm^{-1}}$ infrared band, the measured absorbance is 0.01. For the 337.3 nm electronic band, the measured absorbance is 0.74. Thus, the calculated molar absorptivity for the 337.3 nm band is 39400 $\mathrm{M^{-1}cm^{-I}}$.

The oscillator strength (*f*) for an electronic transition can be calculated from the molar absorptivites (ε) for each band associated with the particular transition:

$$f = 4.33 \times 10^{-9} \int \varepsilon(\nu)\, d\nu \approx 4.33 \times 10^{-9} \Sigma\, \varepsilon(\nu)\, \Delta\nu_{1/2}$$

Thus, after calculating the molar absorptivities for the observed 337.3 nm, 329.3 nm, and 326.4 nm bands, the oscillator strength (*f*) for the $S_1 \leftarrow S_0$ transition is estimated to be 0.013 for neutral benzofluorene.

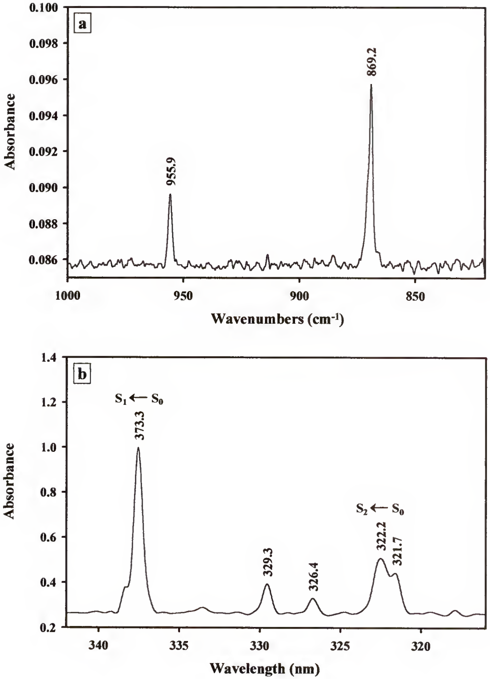

Figure 6-17. Infrared and electronic absorption spectra of neutral benzofluorene used to calculate oscillator strengths for the observed electronic transitions. A) Infrared absorption spectrum from 1000 cm^{-1} to 820 cm^{-1}. B) Electronic absorption spectrum from 342 nm to 316 nm.

The observed absorptions at 337.3 nm, 322.2 nm, 312.2 nm, and 298.5 nm matched the calculated excitation energies within 0.3 eV. Therefore, these bands were assigned to transitions from the ground state to the first four excited states. The weaker bands observed at 329.3 nm and 326.4 nm are most likely due to vibrational progression within the first excited state. The strongest observed band at 259.4 nm was assigned to the $S_5 \leftarrow S_0$ transition based on the relatively large predicted oscillator strength. The strong band at 250.3 nm is tentatively assigned to the $S_8 \leftarrow S_0$. Although the predicted $S_9 \leftarrow S_0$ transition is closer in energy to the 250.3 nm band, the calculated oscillator strength (0.000) is not a reasonable match to the observed band intensity.

Benzofluorene Cation

Electron bombardment of the gas mixture prior to deposition yielded a variety of species in the argon matrix: benzofluorene cation and fragment ions, benzofluorene neutral and neutral fragments, and carbon tetrachloride fragments and fragment ions. Cation bands were identified through matrix annealing, matrix photolysis, and comparison to the benzofluorene neutral spectrum. Annealing the matrix allows movement of negatively charged species that can neutralize PAH cations. Photolysis of the matrix with UV irradiation liberates electrons from negatively charged species in the matrix. These free electrons can then neutralize the trapped PAH cations.

Infrared absorption spectra collected after bombarding the gas mixture with low energy electrons (210 eV) are shown in Figure 6-18 and Figure 6-19. The lower spectrum is the infrared spectrum of neutral benzofluorene recorded previously. The middle spectrum corresponds to the electron bombarded gas mixture. The upper spectrum was recorded after annealing the matrix containing the electron bombardment

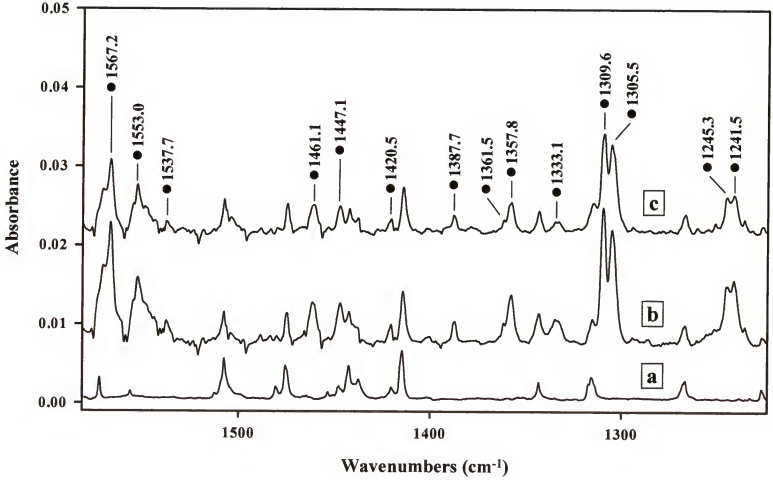

Figure 6-18. Experimental infrared absorption spectra (1580 cm^{-1} to 1225 cm^{-1}) of neutral and cationic benzofluorene isolated in solid Ar at 12 K. Bands assigned to the benzofluorene cation are labeled with black dots. A) IR absorption spectrum of neutral benzofluorene. B) IR absorption spectrum of neutral and cationic benzofluorene with 0.1% CCl_4. C) IR absorption spectrum recorded after annealing matrix B to 34 K.

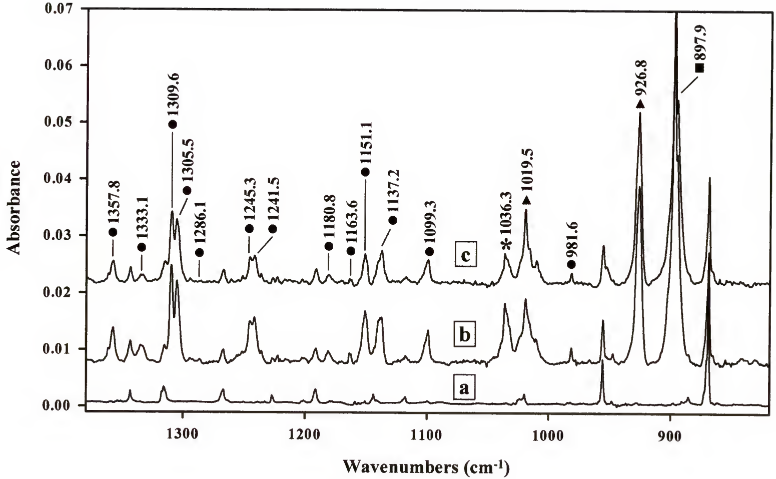

Figure 6-19. Experimental infrared absorption spectra (1380 cm^{-1} to 820 cm^{-1}) of neutral and cationic benzofluorene isolated in solid Ar at 12 K. Dots indicate benzofluorene cation bands. Asterisks, triangles, and squares indicate bands due to CCl_3^+, $CCl_3{\bullet}Cl$, and CCl_3, respectively. A) IR absorption spectrum of neutral benzofluorene. B) IR absorption spectrum of neutral and cationic benzofluorene with 0.1% CCl_4. C) IR absorption spectrum recorded after annealing matrix B to 34 K.

products to 34 K. Bands corresponding to CCl_3, CCl_3^+, and the $CCl_3{\bullet}Cl$ complex were assigned based on previous argon matrix studies.[32] Warming the matrix to 34 K reduced several bands by 20-30%. Bands previously assigned to benzofluorene neutral remained unchanged. Thus, the bands reduced upon annealing were assigned to benzofluorene cations trapped in the matrix.

Vibrational frequencies for the benzofluorene cation were calculated at the B3LYP/6-311+G(d,p) level of theory. The 6-311+G(d,p) basis set was chosen since it accurately predicted frequencies and intensities for the benzofluorene neutral molecule. A scaling factor of 0.98 was applied to account for mode anharmonicities. The observed and calculated vibrational spectra for the benzofluorene cation are depicted in Figure 6-20. Frequencies and relative intensities are listed in Table 6-8. The integral intensity of the calculated 1571.6 cm^{-1} band is 359.3 km/mol. As expected for PAH cations, the C-C stretches and C-H in-plane bends in the 1000 cm^{-1} to 1650 cm^{-1} region were stronger than the C-H out-of-plane bending modes in the 700 cm^{-1} to 1000 cm^{-1} range.

Several regions of the calculated spectrum were inaccessible in the experimental spectrum due to species other than benzofluorene in the matrix. The spectral region from 880 cm^{-1} to 940 cm^{-1} was dominated by the CCl_3 and $CCl_3{\bullet}Cl$ bands. The strong CCl_3^+ and $CCl_3{\bullet}Cl$ bands at 1036.3 cm^{-1} and 1019.5 cm^{-1} prevented observation of the cation band predicted at 1012.7 cm^{-1}. The 1580 cm^{-1} to 1600 cm^{-1} spectral region was obscured by H_2O trapped in the matrix. To better display the correlation between calculated and observed cation frequencies, a synthetic experimental spectrum was created based on the observed cation bands (Figure 6-21). Synthetic bands with 3 cm^{-1} bandwidths were constructed for each observed cation frequency using 50% Gaussian and 50%

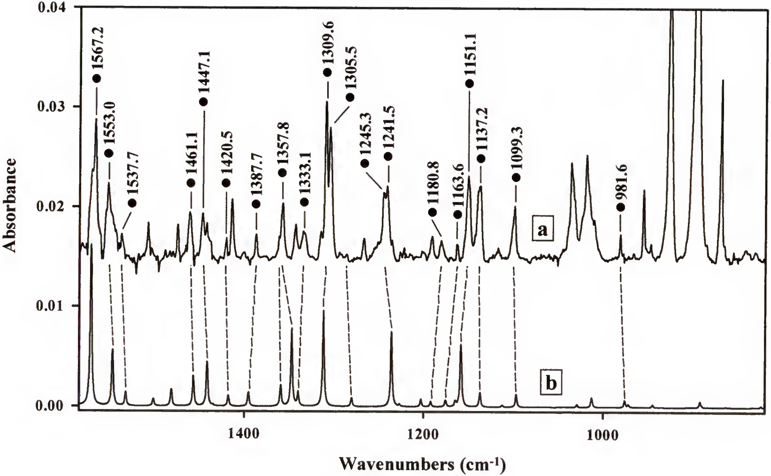

Figure 6-20. Experimental and calculated infrared absorption spectra (1585 cm^{-1} to 820 cm^{-1}) for the benzofluorene cation ($C_{17}H_{12}^{+}$). Dots indicate benzofluorene cation bands. A) IR absorption spectrum of neutral and cationic benzofluorene isolated in solid Ar at 12 K. B) IR absorption spectrum of benzofluorene cation calculated at the B3LYP/6-311+G(d,p) level of theory (scaled by 0.98).

Table 6-8. Calculated (B3LYP/6-311+G(d,p)) and observed (solid Ar) vibrational frequencies (cm^{-1}) for the benzofluorene cation. Relative intensities are given in parentheses. Calculated frequencies are scaled by a factor of 0.98. R and r are stretching modes, α and β are in-plane bending modes, and τ and ε are out-of-plane vibrations.

Mode Description	6-311+G(d,p)	Experimental
α(CCC)	303.3 (0.02)	
τ(CCC)	439.1 (0.04)	
α(CCC)	617.2 (0.07)	
ε(CCH) + τ(CCC)	713.7 (0.09)	
α(CCC) + R(CC)	732.0 (0.16)	
ε(CCH) + τ(CCC)	756.0 (0.05)	
ε(CCH) + τ(CCC)	780.9 (0.22)	
ε(CCH) + τ(CCC)	891.9 (0.03)	
α(CCC) + β(CCH)	975.6 (0.04)	981.6 (0.04)
β(CCH) + R(CC)	1012.7 (0.05)	
β(CCH) + R(CC)	1096.7 (0.07)	1099.3 (0.18)
β(CCH) + R(CC)	1137.4 (0.07)	1137.2 (0.32)
β(CCH) + R(CC)	1158.5 (0.39)	1151.1 (0.29)
β(CCH) + R(CC)	1175.4 (0.05)	1163.6 (0.04)
β(CCH) + R(CC)	1192.2 (0.03)	1180.8 (0.05)
β(CCH) + R(CC)	1203.0 (0.04)	
β(CCH) + R(CC)	1236.0 (0.42)	1241.5, 1245.3 (0.45)
β(CCH) + R(CC)	1280.4 (0.05)	1286.1 (0.04)
β(CCH) + R(CC)	1311.8 (0.55)	1305.5, 1309.6 (1.00)
β(CCH) + R(CC)	1340.1 (0.08)	1334.8, 1333.1 (0.11)
β(CCH) + R(CC)	1347.1 (0.46)	1357.8 (0.18)
β(CCH) + R(CC)	1359.2 (0.07)	1361.5 (0.03)
β(CCH) + R(CC) + ε(HC(sp^3)H)	1395.4 (0.09)	1387.7 (0.05)
β(CCH) + R(CC) + ε(HC(sp^3)H)	1417.7 (0.07)	1420.5 (0.04)
β(CCH) + R(CC)	1441.5 (0.28)	1447.1 (0.15)
β(CCH) + R(CC)	1456.6 (0.19)	1461.1 (0.18)
β(CCH) + R(CC)	1481.4 (0.10)	
R(CC)	1501.4 (0.05)	
R(CC)	1532.5 (0.06)	1537.7 (0.09)
R(CC)	1547.4 (0.35)	1553.0 (0.34)
R(CC)	1571.6 (1.00)	1567.2 (0.77)
R(CC)	1595.8 (0.26)	
R(CC)	1598.0 (0.34)	

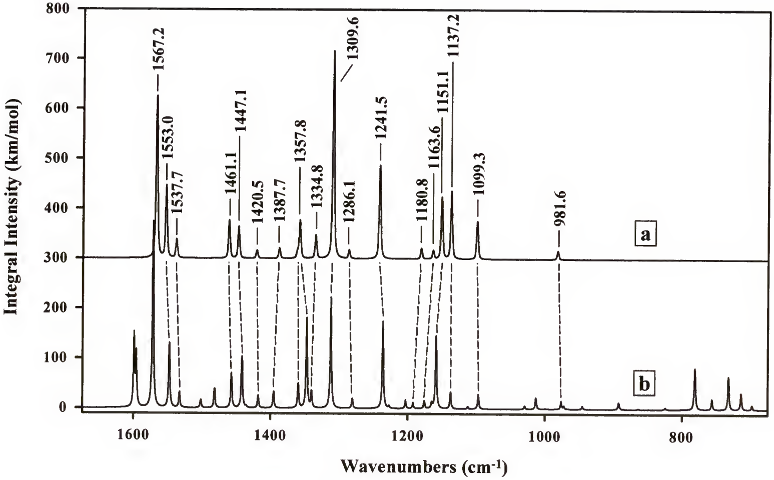

Figure 6-21. Synthetic experimental and calculated infrared absorption spectra (1675 cm^{-1} to 675 cm^{-1}) for the benzofluorene cation ($C_{17}H_{12}^{+}$). A) Synthetic IR absorption spectrum of the benzofluorene cation created from energies and relative intensities observed in solid Ar at 12 K. B) IR absorption spectrum of benzofluorene cation calculated at the B3LYP/6-311+G(d,p) level of theory (scaled by 0.98).

Lorentzian functions. Intensities were assigned based on the observed relative intensities in the matrix. Overall, good agreement was found for the observed and predicted frequencies and intensities.

The UV-visible absorption spectrum collected after electron bombardment of the gas mixture contained three new features at 714.5 nm, 599.0 nm, and 508.5 nm (Figure 6-22). Because PAH cations generally absorb at energies in the visible range, these bands were possibly due to benzofluorene cations. Annealing of the matrix to 34 K decreased the 714.5 nm and 599.0 nm bands by 30% and 20%, respectively (Figure 6-23). However, the 508.5 nm band remained unchanged by matrix annealing. Due to their reduction upon annealing, the 714.5 nm and 599.0 nm bands were assigned to cationic species. However, based on vertical excitation energies and oscillator strengths calculated by TDDFT, only the 714.5 nm band was assignable to an electronic transition ($D_3 \leftarrow D_0$) in the benzofluorene cation (Table 6-9). Because the 508.5 nm band was unaffected by matrix annealing, it was assigned to a neutral species.

Singly Dehydrogenated Benzofluorene ($C_{17}H_{11}$)

Since the 508.5 nm band and the 599.0 nm band appeared only in electron bombardment experiments and were not assignable to neutral or cationic benzofluorene, these bands were likely due to fragmentation products of benzofluorene. Photolysis of the matrix with the full output of a 100 W medium-pressure Hg lamp for 5 hours reduced the 714.5 nm band by 47% (Figure 6-24). The 599.0 nm band and the 508.5 nm band increased by 38% and 230%, respectively during matrix irradiation. The new band appearing at 490.8 nm was attributed to vibrational progression of the 508.5 nm band. The 47% decrease of the 714.5 nm band is due to both neutralization and fragmentation

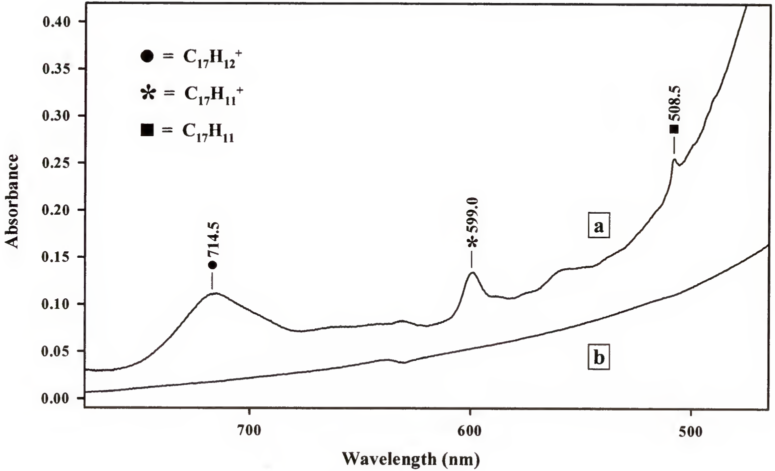

Figure 6-22. Electronic absorption spectra (775 nm to 465 nm) of neutral, cationic, and fragmented benzofluorene isolated in solid Ar at 12 K. A) Electronic absorption spectrum recorded after electron bombardment of an Ar/benzofluorene/CCl_4 (0.1%) gas mixture. B) Electronic absorption spectrum of neutral benzofluorene.

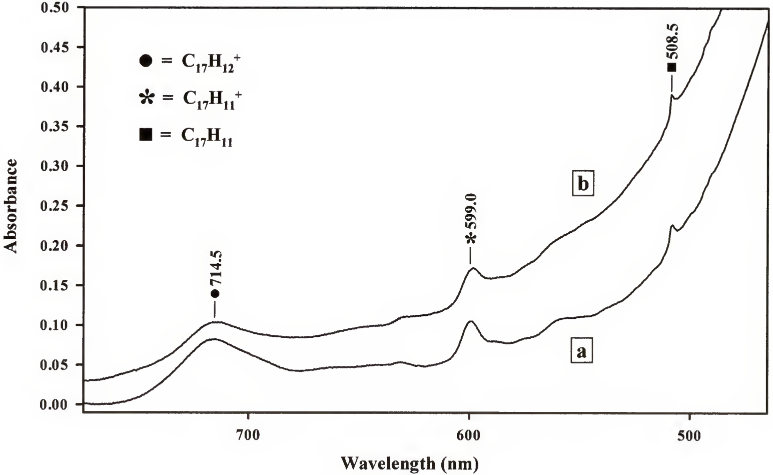

Figure 6-23. Electronic absorption spectra (775 nm to 465 nm) of neutral, cationic, and fragmented benzofluorene isolated in solid Ar at 12 K. A) Electronic absorption spectrum recorded after electron bombardment of an Ar/benzofluorene/CCl_4 (0.1%) gas mixture. B) Electronic absorption spectrum recorded after annealing matrix A to 34 K.

Table 6-9. Calculated (TDDFT BLYP/6-31G(d,p)) and observed (solid Ar) vertical excitation energies (eV) and oscillator strengths for the benzofluorene radical cation.

	Calculated		Experimental		
Transition	**ω (eV)**	***f***	**λ (nm)**	**ω (eV)**	***f***
$D_1(^2A'') \leftarrow D_0(^2A'')$	0.77	0.013			
$D_2(^2A'') \leftarrow D_0(^2A'')$	1.01	0.007			
$D_3(^2A'') \leftarrow D_0(^2A'')$	1.87	0.119	714.5	1.74	0.034
$D_4(^2A'') \leftarrow D_0(^2A'')$	2.25	0.004			
$D_5(^2A'') \leftarrow D_0(^2A'')$	2.86	0.030			
$D_6(^2A') \leftarrow D_0(^2A'')$	2.89	0.000			
$D_7(^2A') \leftarrow D_0(^2A'')$	3.00	0.000			
$D_8(^2A'') \leftarrow D_0(^2A'')$	3.13	0.039			
$D_9(^2A'') \leftarrow D_0(^2A'')$	3.22	0.169			
$D_{10}(^2A') \leftarrow D_0(^2A'')$	3.34	0.000			
$D_{11}(^2A') \leftarrow D_0(^2A'')$	3.39	0.000			
$D_{12}(^2A'') \leftarrow D_0(^2A'')$	3.47	0.001			

of the benzofluorene cation. Since the 599.0 nm band was already assigned to a cationic species, the 38% increase likely results from fragmentation of the benzofluorene cation. The 508.5 nm band was previously assigned to a neutral fragment of benzofluorene. The substantial 230% increase of this band during UV irradiation may result from both fragmentation of neutral benzofluorene and neutralization of the benzofluorene fragment ion. Therefore, the 599.0 nm band and the 508.5 nm band are assigned to the cationic and neutral forms of the same benzofluorene fragment.

Based on theoretical bond energy calculations, the lowest energy fragmentation route (< 3.50 eV) for both neutral and cationic benzofluorene is removal of a hydrogen atom ($H_{11'}$) from the five-membered ring. Loss of this hydrogen was observed in the

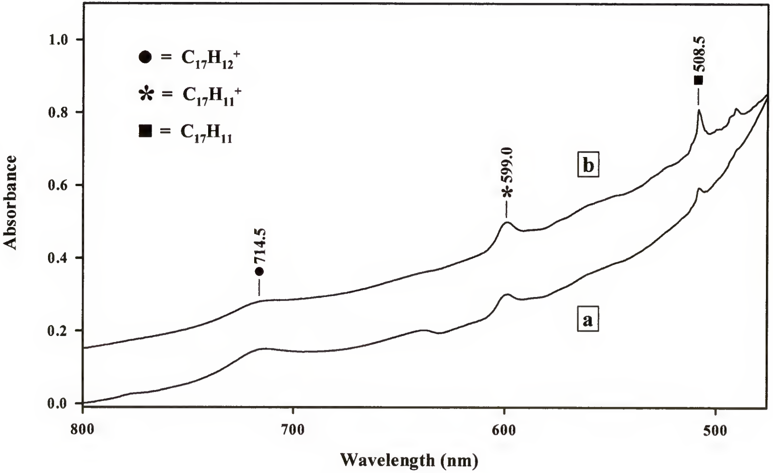

Figure 6-24. Electronic absorption spectra (800 nm to 475 nm) of neutral, cationic, and fragmented benzofluorene isolated in solid Ar at 12 K. A) Electronic absorption spectrum recorded after electron bombardment of an Ar/benzofluorene/CCl_4 (0.1%) gas mixture. B) Electronic absorption spectrum recorded after irradiating matrix A with the output of a 100 W medium-pressure Hg lamp for 5 hours.

previously described FT-ICR MS experiments involving electron bombardment and UV photolysis of gas-phase benzofluorene. Therefore, electron bombardment of gas-phase benzofluorene prior to deposition would likely yield singly-dehydrogenated benzofluorene neutrals ($C_{17}H_{11}$) and cations ($C_{17}H_{11}^+$) in the matrix. Similarly, UV irradiation of the matrix would also abstract hydrogen atoms from trapped neutral and cationic benzofluorene. Thus, calculated vertical excitation energies and vibrational frequencies for $C_{17}H_{11}$ and $C_{17}H_{11}^+$ were compared to the recorded electronic and IR absorption spectra.

The 508.5 nm band is within 0.3 eV of the strongest transition ($D_3 \leftarrow D_0$) predicted by TDDFT calculations at the B3LYP/6-31++G(d,p) level of theory for $C_{17}H_{11}$ (Table 6-10). The observed 599.0 nm band is within 0.3 eV of the relatively strong $S_2 \leftarrow S_0$ transition predicted by TDDFT calculations at the BLYP/6-31G(d,p) level of theory for $C_{17}H_{11}^+$ (Table 6-11). Although the $S_9 \leftarrow S_0$ transition is predicted to be stronger than the $S_2 \leftarrow S_0$ transition, the band is most likely obscured by the strong benzofluorene neutral band at 298.5 nm.

Vibrational frequencies for $C_{17}H_{11}$ and $C_{17}H_{11}^+$ were calculated at the B3LYP/6-31G level of theory (Table 6-12). However, no direct evidence of dehydrogenated neutral or cationic benzofluorene was found in the experimental infrared absorption spectrum. In general, maximum IR integral intensities for cationic PAHs are much higher than IR integral intensities for neutral PAHs. The largest IR integral intensity for $C_{17}H_{11}$ was 70 km/mol, whereas the largest calculated IR integral intensity for $C_{17}H_{11}^+$ was 594 km/mol. Thus, assuming equal concentrations of benzofluorene neutral and

Table 6-10. Calculated (TDDFT BLYP/6-31++G(d,p)) and observed (solid Ar) vertical excitation energies (eV) and oscillator strengths for the $C_{17}H_{11}$ radical.

	Calculated		Experimental	
Transition	ω (eV)	f	λ (nm)	ω (eV)
$D_1(^2A'') \leftarrow D_0(^2A'')$	1.65	0.004		
$D_2(^2A'') \leftarrow D_0(^2A'')$	2.00	0.016		
$D_3(^2A'') \leftarrow D_0(^2A'')$	2.21	0.059	508.5	2.44
$D_4(^2A'') \leftarrow D_0(^2A'')$	2.81	0.002		
$D_5(^2A'') \leftarrow D_0(^2A'')$	2.88	0.002		
$D_6(^2A'') \leftarrow D_0(^2A'')$	3.10	0.040		
$D_7(^2A'') \leftarrow D_0(^2A'')$	3.21	0.009		
$D_8(^2A'') \leftarrow D_0(^2A'')$	3.35	0.002		
$D_9(^2A'') \leftarrow D_0(^2A'')$	3.48	0.001		
$D_{10}(^2A'') \leftarrow D_0(^2A'')$	3.60	0.024		
$D_{11}(^2A') \leftarrow D_0(^2A'')$	3.69	0.000		

Table 6-11. Calculated (TDDFT BLYP/6-31++G(d,p)) and observed (solid Ar) vertical excitation energies (eV) and oscillator strengths for the $C_{17}H_{11}^+$ cation.

	Calculated		Experimental	
Transition	ω (eV)	f	λ (nm)	ω (eV)
$S_1(^1A') \leftarrow S_0(^1A')$	1.32	0.002		
$S_2(^1A') \leftarrow S_0(^1A')$	2.26	0.249	599.0	2.07
$S_3(^1A') \leftarrow S_0(^1A')$	2.62	0.013		
$S_4(^1A') \leftarrow S_0(^1A')$	3.37	0.039		
$S_5(^1A') \leftarrow S_0(^1A')$	3.54	0.025		
$S_6(^1A'') \leftarrow S_0(^1A')$	3.74	0.000		
$S_7(^1A') \leftarrow S_0(^1A')$	3.89	0.011		
$S_8(^1A'') \leftarrow S_0(^1A')$	3.91	0.000		
$S_9(^1A') \leftarrow S_0(^1A')$	4.16	0.946		
$S_{10}(^1A'') \leftarrow S_0(^1A')$	4.22	0.000		
$S_{11}(^1A'') \leftarrow S_0(^1A')$	4.29	0.000		

Table 6-12. Calculated (B3LYP/6-31G(d,p)) vibrational frequencies (cm^{-1}) for the $C_{17}H_{11}$ neutral radical and the $C_{17}H_{11}^+$ cation. Integral intensities (km/mol) are given in parentheses.

$C_{17}H_{11}$		$C_{17}H_{11}^+$	
Freq.(Int.)	**Freq.(Int.)**	**Freq.(Int.)**	**Freq.(Int.)**
65.0 (0.6)	1162.5 (1.9)	62.3 (1.4)	1136.9 (67.4)
335.2 (0.6)	1187.5 (1.1)	203.5 (1.5)	1173.1 (58.6)
398.3 (2.3)	1204.2 (1.1)	336.1 (4.3)	1181.2 (11.1)
442.5 (0.7)	1262.2 (2.2)	351.0 (0.8)	1188.0 (7.8)
472.8 (8.9)	1268.3 (13.3)	386.4 (4.1)	1216.4 (12.9)
482.9 (1.7)	1360.3 (4.3)	432.2 (1.4)	1228.2 (1.2)
534.5 (2.3)	1369.1 (2.6)	460.1 (9.9)	1257.8 (33.5)
540.6 (0.9)	1417.0 (0.6)	476.1 (31.3)	1269.5 (18.4)
569.9 (2.0)	1442.7 (2.7)	527.6 (30.8)	1298.7 (31.5)
610.2 (0.5)	1455.6 (4.4)	536.0 (4.1)	1328.0 (48.4)
630.4 (1.9)	1473.0 (4.4)	564.9 (5.3)	1338.8 (17.8)
683.7 (6.7)	1488.6 (7.5)	609.9 (5.4)	1366.6 (216.4)
730.0 (5.8)	1525.3 (35.1)	624.9 (5.2)	1375.2 (25.2)
747.7 (32.4)	1577.5 (33.2)	686.7 (4.9)	1421.3 (11.9)
754.2 (18.9)	1588.0 (7.1)	750.3 (12.4)	1446.4 (6.6)
772.4 (9.8)	1603.4 (3.8)	756.2 (2.4)	1474.3 (2.6)
773.8 (11.7)	1628.9 (3.4)	767.1 (53.6)	1493.0 (22.9)
847.1 (5.2)	3121.4 (9.8)	769.8 (18.9)	1505.4 (45.3)
861.5 (3.9)	3123.7 (14.5)	805.3 (12.0)	1552.1 (160.3)
872.7 (22.8)	3139.5 (42.1)	864.4 (1.3)	1584.9 (175.2)
897.8 (3.9)	3151.5 (69.8)	888.6 (2.3)	1600.0 (593.5)
923.5 (1.2)	3174.0 (10.6)	911.4 (4.7)	1615.7 (46.7)
940.2 (3.8)		927.4 (9.0)	1618.9 (157.6)
1025.7 (0.8)		954.6 (3.3)	1640.6 (28.3)
1034.7 (2.2)		978.0 (23.9)	3145.9 (2.0)
1101.7 (3.1)		1023.5 (2.4)	3160.9 (2.0)
1117.9 (6.0)		1041.9 (5.7)	3162.7 (1.4)
1143.1 (5.3)		1107.4 (10.3)	3172.9 (5.0)
1159.2 (1.7)		1121.0 (203.4)	

cation fragments in the matrix, vibrational bands corresponding to $C_{17}H_{11}^+$ should be more intense than those corresponding to $C_{17}H_{11}$.

Calculated oscillator strengths for $C_{17}H_{11}^+$ are greater than those predicted for the benzofluorene cation ($C_{17}H_{12}^+$). The predicted oscillator strength for the observed $D_3 \leftarrow D_0$ transition in the benzofluorene cation is 0.119. The oscillator strength for the observed $S_2 \leftarrow S_0$ transition in $C_{17}H_{11}^+$ is 0.249. Thus, at equal concentrations of $C_{17}H_{11}^+$ and $C_{17}H_{12}^+$, the fragment ion band at 599.0 nm should be twice as intense as the benzofluorene cation band at 714.5 nm. However, the observed intensity ratio of the 599.0 nm band to the 714.5 nm band is approximately 1:5, indicating that the concentration of $C_{17}H_{11}^+$ is much lower than the concentration of the benzofluorene cation. If the same intensity ratio for $C_{17}H_{11}^+$ and the benzofluorene cation applies to the IR absorption spectrum, vibrational bands due to $C_{17}H_{11}^+$ would be too weak to observe. Because no IR bands were assignable to $C_{17}H_{11}$ and $C_{17}H_{11}^+$, experimental oscillator strengths could not be determined for the 599.0 nm and 508.5 nm bands.

Comparison to UIR Emission Features

Several infrared absorption bands observed for the benzofluorene cation match the UIR emission features. The strong bands at 1305.5 cm^{-1} (7.66 μm) and 1309.6 cm^{-1} (7.64 μm) correlate well with the most intense UIR band at 7.7 μm. Furthermore, the 1245.3 cm^{-1} (8.03 μm), 1241.5 cm^{-1} (8.05 μm), 1151.1 cm^{-1} (8.69 μm), and 1137.2 cm^{-1} (8.79 μm) bands fit within the broad UIR envelope defined by the 7.7 μm and 8.6 μm features. The band at 1567.2 cm^{-1} (6.38 μm) is close to the 6.2 μm emission feature. Potential bands contributing to the 11.3 μm (885 cm^{-1}) UIR feature may be obscured by the strong CCl_3 band at 897.9 cm^{-1} or the benzofluorene neutral band at 869.2 cm^{-1}. The calculated IR absorption spectrum for the benzofluorene cation contains bands in this obscured experimental range. The weak predicted band at 891.9 cm^{-1} (11.2 μm) may contribute to the 11.3 μm feature. Thus, IR absorption bands for the benzofluorene cation may account for the 6.2 μm, 7.7 μm, 8.6 μm, and 11.3 μm UIR emission features. However, no significant bands were observed in the 3000 cm^{-1} (3.3 μm) region of the benzofluorene cation spectrum.

The relative band intensities in the infrared absorption spectrum of the benzofluorene cation also correlated well with the UIR emission spectrum. For the benzofluorene cation, the C-C stretching and C-H in-plane bending modes in the 1100 cm^{-1} to 1650 cm^{-1} (9.1 μm to 6.1 μm) range are more intense than the C-H out-of-plane bending modes in the 700 cm^{-1} to 1000 cm^{-1} (14.3 μm to 10.0 μm) range. The 1305.5 cm^{-1} (7.66 μm), 1309.6 cm^{-1} (7.64 μm), and 1567.2 cm^{-1} (6.38 μm) bands are the strongest bands observed in the experimental spectrum. These bands are at least twenty times more intense than the experimental 981.6 cm^{-1} (10.2 μm) band. Calculated bands at 780.9 cm^{-1} (12.8 μm) and 732.0 cm^{-1} (13.7 μm) are predicted to be five times stronger than the observed 981.6 cm^{-1} band. However, the BaF_2 deposition window, which is transparent only from 67,000 cm^{-1} to 870 cm^{-1}, prevents observation of experimental frequencies near the predicted 780.9 cm^{-1} and 732.0 cm^{-1} bands. Nevertheless, these bands are predicted to be weaker than the intense bands in the 1100 cm^{-1} to 1650 cm^{-1} region. Thus, the observed intensity pattern for the benzofluorene cation correlates well with the relative intensities of the UIR emission spectrum, in which the 6.2 μm, 7.7 μm, and 8.6 μm features are observed to be stronger than the 11.3 μm feature.

However, a few experimental bands do not correlate well with the UIR features. The observed band at 981.6 cm^{-1} (10.2 μm) does not appear in the UIR emission spectrum, which is generally flat from 9.0 μm to 11.0 μm. Vibrational modes in this region were attributed to breathing modes exhibited by PAHs with an aromatic ring not fused directly to another aromatic ring.[41] Because benzofluorene contains an aromatic ring fused only to a non-aromatic pentagonal ring, it is also expected to exhibit these breathing modes. In this respect, the benzofluorene cation may not significantly contribute to the UIR emission bands. Furthermore, the predicted bands at 780.9 cm^{-1} (12.8 μm) and 732.0 cm^{-1} (13.7 μm) are not in agreement with the UIR spectrum. If these bands are dependent upon hydrogen adjacency, they may shift to higher frequencies if the benzofluorene cation is dehydrogenated.

Due to low concentration, the singly-dehydrogenated benzofluorene fragment ion ($C_{17}H_{11}^+$) was not observed in the IR spectrum. However, strong bands are predicted at 1600.0 cm^{-1} (6.25 μm), 1366.6 cm^{-1} (7.32 μm), and 1121.0 cm^{-1} (8.92 μm). The 7.32 μm and 8.92 μm bands do not correlate well with the UIR emission features at 7.7 μm and 8.6 μm. Furthermore, the calculated 767.1 cm^{-1} (13.0 μm) band does not appear in the UIR emission spectrum. The $C_{17}H_{11}^+$ fragment ion most likely results from hydrogen abstraction from the pentagonal ring of the benzofluorene cation. Thus, the hydrogen adjacency of the six-membered rings is unaffected by single hydrogen removal. Since significant dehydrogenation would be required for the C-H out-of-plane vibrational modes to shift to higher frequencies, the $C_{17}H_{11}^+$ fragment ion does not appear to be a significant contributor to the UIR emission features.

CHAPTER 7
SUMMARY AND CONCLUSIONS

Polycyclic aromatic hydrocarbon (PAH) cations are believed to be the carriers of the unidentified infrared (UIR) emission bands observed in the interstellar medium. To date, very little research has been conducted on PAH cations containing five-membered rings. This study focused on three PAH cations containing five-membered rings: acenaphthene, acenaphthylene, and benzofluorene. The photochemical behavior of these PAH cations was investigated via FT-ICR mass spectrometry, DFT calculations, and matrix isolation spectroscopy.

Acenaphthene

The loss of four hydrogens was observed upon UV irradiation of the acenaphthene cation ($C_{12}H_{10}^+$). The major photoproduct was the relatively stable acenaphthylene cation ($C_{12}H_8^+$). This photofragmentation route involved the sequential loss of two hydrogens from the aliphatic pentagonal ring. Energies predicted for each hydrogen removal were relatively low (< 3.5 eV). After loss of the first hydrogen from the acenaphthene cation, a lower yield simultaneous hydrogen loss fragmentation channel was observed. Energies required for simultaneous hydrogen loss were not calculated. The predicted sequential hydrogen loss pathway for acenaphthene involved stripping hydrogens from one six-membered ring after two hydrogens were removed from the pentagonal ring. Calculated energies required for removal of these two hydrogens from the six-membered ring were ~ 4 eV.

The photofragmentation of acenaphthene is of astrophysical interest due to the stability of its doubly-dehydrogenated photoproduct. In regions of low UV flux, the acenaphthene cation ($C_{12}H_{10}^+$) may remain fully hydrogenated or lose one hydrogen to form the closed-shell $C_{12}H_9^+$ fragment ion. In regions of moderate UV flux, the doubly-dehydrogenated form ($C_{10}H_8^+$) should predominate. In regions of high UV flux, the loss of two additional hydrogens is possible. Because the hydrogens are most likely removed from adjacent positions on the same six-membered ring, benzyne bond formation is expected. Thus, in addition to contributing to the standard UIR emission features, the acenaphthene cation and its fragment ions may be responsible for the weaker aliphatic C-H stretches (3.4 μm) or C-C benzyne stretches (5.1-5.3 μm) depending on the interstellar region.

Acenaphthylene

The sequential loss of two hydrogens was observed upon irradiation of the acenaphthylene cation ($C_{12}H_8^+$). The low yields of the dehydrogenated fragment ions supported earlier conclusions that the acenaphthylene cation was photostable.[47] Furthermore, the predicted energy for hydrogen loss from the six-membered ring was relatively high (~5 eV), supporting the observed low fragment yields.

Acenaphthylene has been considered a building block for larger PAHs in the interstellar medium.[15] Due to its photostability, the acenaphthylene cation is expected to survive in a variety of interstellar environments. In regions of high atomic hydrogen abundance, the acenaphthylene cation can hydrogenate to form the acenaphthene cation.[37] In areas of high carbon abundance, acenaphthylene may be involved in the formation of larger PAHs. In regions of high UV photon flux, dehydrogenation of the acenaphthylene cation can contribute to UIR features associated with C-C benzyne stretches. Therefore, the astrophysical role of acenaphthylene may be quite significant.

In FT-ICR studies, acenaphthylene cation was also observed to participate in ion-molecule reactions to form $C_{24}H_{16}^+$. Upon UV irradiation, the $C_{24}H_{16}^+$ aggregate ion either photodissociated to neutral and cationic acenaphthylene, or underwent sequential dehydrogenation to form the photostable $C_{24}H_{12}^+$ ion. The dimerization of neutral acenaphthylene was previously observed to form cyclobutadiacenaphthylene.[63] Based on fragmentation patterns and pathways, the cyclobutadiacenaphthylene cation was determined to be the best match for the acenaphthylene aggregate ion. Due to the large size of the cyclobutadiacenaphthylene system, carbon-hydrogen bond energies were not calculated. Thus, the structure of the photostable $C_{24}H_{12}^+$ ion remains undetermined. If ion-molecule reactions are relevant in the interstellar medium, the formation and dehydrogenation of cyclobutadiacenaphthylene may yield a potential photostable carrier of the UIR emission bands.

Benzofluorene

Photodissociation pathways for the benzofluorene cation ($C_{17}H_{12}^+$) involved both hydrogen and carbon loss. Loss of three hydrogens was observed upon UV irradiation. Removal of the first hydrogen from the pentagonal ring required very little energy (2.60 eV). Subsequent dehydrogenation proceeded as both single and double hydrogen loss. However, calculated C-H bond energies were too similar for prediction of a sequential dehydrogenation pathway. Acetylene (C_2H_2) loss was observed following single hydrogen loss from the benzofluorene cation. Although acetylene units are most likely removed from the exposed six-membered ring, the exact positions of acetylene loss remain undetermined. Thus, as suggested in earlier studies,[47] linear PAH cations with exposed six-membered rings are not expected to survive in interstellar regions of high photon flux. However, acetylene loss was not observed following the loss of three hydrogens from the benzofluorene cation, indicating that the triply-dehydrogenated benzofluorene cation was photostable. Therefore, dehydrogenation of PAH cations may increase photostability in the interstellar medium.

Infrared and electronic spectra were collected for the benzofluorene cation trapped in solid argon at 12 K. Several observed IR absorption bands correlated well with the UIR emission bands. However, the observed bands near 10 μm associated with vibrational breathing modes do not appear in the UIR emission spectrum. Photolysis of the isolated benzofluorene cation produced the singly-dehydrogenated $C_{17}H_{11}^+$ fragment ion. Although observable in the electronic spectrum, the concentration of this fragment ion was too low to appear in the infrared spectrum. The calculated IR absorption spectrum of $C_{17}H_{11}^+$ was not consistent with the UIR bands. However, more extensive fragmentation of the benzofluorene cation may yield potential UIR carriers.

PAHs Containing Pentagonal Rings

In general, the class of PAHs containing five-membered rings may be quite significant in the interstellar medium. Small, compact PAHs, such as acenaphthene and acenaphthylene, appear to have a photostable base-structure. Thus, they may undergo dehydrogenation/hydrogenation cycles in different interstellar regions. Although linear PAHs, such as benzofluorene, appear to be less stable, they may yield stable fragment ions that can contribute to the observed UIR emission bands. Consequently, further studies on PAHs containing pentagonal rings should prove valuable in identifying the carriers of the UIR features.

REFERENCE LIST

1. Gillett, F. C.; Forrest, W. J.; Merrill, K. M. *Astrophys. J.* **1973**, *183*, 87.

2. Russell, R. W.; Soifer, B. T.; Willner, S. P. *Astrophys. J.* **1977**, *217*, L149.

3. Merrill, K. M.; Soifer, B. T.; Russell, R. W. *Astrophys. J.* **1975**, *200*, L37.

4. Geballe, T. R.; Tielens, A. G. G. M.; Allamandola, L. J.; Moorhouse, A.; Brand, P. W. J. L. *Astrophys. J.* **1989**, *341*, 278.

5. Sloan, G. C.; Hayward, T. L.; Allamandola, L. J.; Bregman, J. D.; DeVito, B.; Hudgins, D. M. *Astrophys. J.* **1999**, *513*, L65.

6. Williams, D. A. *Molecules and Grains in Space*; Nenner, I., Ed; American Institute of Physics Press: New York, 1993; p 3.

7. Savage, B. D.; Sembach, K. R. *Annu. Rev. Astron. Astrophys.* **1996**, *34*, 279.

8. Allamandola, L. J.; Greenberg, J. M.; Norman, C. A. *Astron. Astrophys.* **1979**, *77*, 66.

9. Schutte, W. A.; Tielens, A. G. G. M.; Allamandola, L. J. *Astrophys. J.* **1993**, *415*, 397.

10. Duley, W. W.; Williams, D. A. *Mon. Not. R. Astron. Soc.* **1981**, *196*, 269.

11. Dwek, E.; Sellgren, K.; Soifer, B. T.; Werner, M. W. *Astrophys. J.* **1980**, *238*, 140.

12. Sellgren, K. *Astrophys. J.* **1984**, *277*, 623.

13. Leger, A.; Puget, J. L. *Astron. Astrophys.* **1984**, *137*, L5.

14. Snow, T. P.; Witt, A. N. *Science* **1995**, *270*, 1455.

15. Keller, R. *Polycyclic Aromatic Hydrocarbons and Astrophysics*; Leger, A., d'Hendecourt, L., Boccara, N., Eds.; Reidel: Dordrecht, 1987; p 3.

16. Gail, H. P.; Sedlmayr, E. *Physical Processes in Interstellar Clouds*; Morfill, G. E., Scholer, M., Eds.; Reidel: Dordrecht, 1987; p 275.

17. Joblin, C.; Tielens, A. G. G. M.; Geballe, T. R.; Wooden, D. H. *Astrophys. J.* **1996**, *460*, L119.

18. Bernstein, M. P.; Sandford, S. A.; Allamandola, L. J. *Astrophys. J.* **1996**, *472*, L127.

19. Allamandola, L. J.; Tielens, A. G. G. M.; Barker, J. R. *Astrophys. J.* **1985**, *290*, L25.

20. Pauzat, F.; Talbi, D.; Ellinger, Y. *Astron. Astrophys.* **1997**, *319*, 318.

21. Langhoff, S. R. *J. Phys. Chem.* **1996**, *100*, 2819.

22. Hudgins, D. M.; Sandford, S. A.; Allamandola, L. J. *J. Phys. Chem.* **1994**, *98*, 4243.

23. Szczepanski, J.; Vala, M. *Nature* **1993**, *363*, 699.

24. Allamandola, L. J.; Tielens, A. G.; Baker, J. R. *Astrophys. J. Suppl.* **1989**, *71*, L733.

25. Snow, T. P.; Le Page, V.; Keheyan, Y.; Bierbaum, V. M. *Nature* **1998**, *391*, 259.

26. Bauschlicher, C. W. *Astrophys. J.* **1998**, *509*, L125.

27. Bakes, E. L. O.; Tielens, A. G. G. M.; Bauschlicher Jr., C. W.; Hudgins, D. M.; Allamandola, L. J. *Astrophys. J.* **2001**, *560*, 261.

28. Bakes, E. L. O.; Tielens, A. G. G. M.; Bauschlicher Jr., C. W.; *Astrophys. J.* **2001**, *556*, 501.

29. Hudgins, D. M.; Allamandola, L. J. *J. Phys. Chem.* **1995**, *99*, 3033.

30. Hudgins, D. M.; Allamandola, L. J. *J. Phys. Chem.* **1995**, *99*, 8978.

31. Hudgins, D. M.; Bauschlicher, C. W.; Allamandola, L. J.; Fetzer, J. C. *J. Phys. Chem. A* **2000**, *104*, 3655.

32. Szczepanski, J.; Roser, D.; Personette, W.; Eyring, M.; Pellow, R.; Vala, M. *J. Phys. Chem.* **1992**, *96*, 7876.

33. Szczepanski, J.; Vala, M. *Astrophys. J.* **1993**, *414*, 646.

34. Szczepanski, J.; Vala, M.; Talbi, D.; Parisel, O.; Ellinger, Y. *J. Chem. Phys.* **1993**, *98*, 4494.

35. Szczepanski, J.; Banisaukas, J.; Vala, M.; Hirata, S.; Bartlett, R. J.; Head-Gordon, M. *J. Phys. Chem. A* **2002**, *106*, 63.

36. Szczepanski, J.; Banisaukas, J.; Vala, M.; Hirata, S.; Wiley, W. R. *J. Phys. Chem. A* **2002**, *106*, 6935.

37. Banisaukas, J.; Szczepanski, J.; Eyler, J.; Vala, M.; Hirata, S.; Head-Gordon, M.; Oomens, J.; Meijer, G.; von Helden, G. *J. Phys. Chem. A* **2003**, *107*, 782.

38. Piest, H.; von Helden, G.; Meijer, G. *Astrophys. J.* **1999**, *520*, L75.

39. Piest, J. A.; Oomens, J.; Bakker, J.; von Helden, G.; Meijer, G. *Spectrochimica Acta A* **2001**, *57*, 717.

40. Oomens, J.; van Roij, A. J. A.; Meijer, G.; von Helden, G. *Astrophys. J.* **2000**, *542*, 404.

41. Oomens, J.; Meijer, G.; von Helden, G. *J. Phys. Chem. A* **2001**, *105*, 8302.

42. Cook, D. J.; Schlemmer, S.; Balucani, N.; Wagner, D. R.; Steiner, B.; Saykally, R. J. *Nature* **1996**, *380*, 227.

43. Kim, H. S.; Saykally, R. J. *Astrophys. J. Suppl.* **2002**, *143*, 455.

44. Boissel, P.; de Parseval, P.; Marty, P.; Lefevre, G. *J. Chem. Phys.* **1997**, *106*, 4973.

45. Boissel, P.; Lefevre, G.; Thiebot, P. *Molecules and Grains in Space*; Nenner, I., Ed; American Institute of Physics Press: New York, 1993; p 667.

46. Ekern, S. P.; Marshall, A. G.; Szczepanski, J.; Vala, M. *Astrophys. J.* **1997**, *488*, L39.

47. Ekern, S. P.; Marshall, A. G.; Szczepanski, J.; Vala, M. *J. Phys. Chem. A* **1998**, *102*, 3498.

48. Allain, T.; Leach, S.; Sedlmayr, E. *Astron. Astrophys.* **1996**, *305*, 602.

49. Jochims, H. W.; Rasekh, E.; Ruhl, H.; Baumgartel, H. *Chem. Phys.* **1992**, *168*, 159.

50. Jochims, H. W.; Ruhl, E.; Baumgartel, H.; Tobita, S.; Leach, S. *Astrophys. J.* **1994**, *420*, 307.

51. Jochims, H. W.; Baumgartel, H.; Leach, S. *Astrophys. J.* **1999**, *512*, 500.

52. Dibben, M. J.; Kage, D.; Szczepanski, J.; Eyler, J. R.; Vala, M. *J. Phys. Chem.* **2001**, *105*, 6024.

53. Szczepanski, J.; Dibben, M. J.; Pearson, W.; Eyler, J. R.; Vala, M. *J. Phys. Chem. A* **2001**, *105*, 9388.

54. Frisch, M. J.; Trucks, G. W.; Schlegel, H. B.; Scuseria, G. E.; Robb, M. A.; Cheeseman, J. R.; Zakrzewski, V. G.; Montgomery, J. A., Jr.; Stratmann, R. E.; Burant, J. C.; Dapprich, S.; Millam, J. M.; Daniels, A. D.; Kudin, K. N.; Strain, M.

C.; Farkas, O.; Tomasi, J.; Barone, V.; Cossi, M.; Cammi, R.; Mennucci, B.; Pomelli, C.; Adamo, C.; Clifford, S.; Ochterski, J.; Peterson, G. A.; Ayala, P. Y.; Cui, Q.; Morokuma, K.; Malick, D. K.; Rabuck, A. D.; Raghavachari, K.; Foresman, J. B.; Cioslowski, J.; Ortiz, J. V.; Stefanov, B. B.; Liu, G.; Liashenko, A.; Piskorz, P.; Komaromi, I.; Gomperts, R.; Martin, R. L.; Fox, D. J.; Keith, T.; Al-Laham, M. A.; Peng, C. Y.; Nanayakkara, A.; Gonzalez, C.; Challacombe, M.; Gill, P. M. W.; Johnson, B.; Chen, W.; Wong, M. W.; Andres, J. L.; Gonzalez, C.; Head-Gordon, M.; Replogle, E. S.; Pople, J. A. *Gaussian 98*, Revision a.3; Gaussian, Inc.: Pittsburgh, PA, 1998.

55. Stevens, P. J.; Devlin, F. J.; Chablowski, C. F.; Frisch, M. J. *J. Phys. Chem.* **1994**, *98*, 11623.

56. *Cermax Lamp Engineering Guide*, ILC Technology, 399 West Java Drive, Sunnyvale, CA 94089.

57. Senko, M. W.; Canterbury, J. D.; Guan, S.; Marshall, A. G. *Rapid Commun. Mass Spectrom.* **1996**, *10*, 1839.

58. Marshall, A. G.; Wang, T. C. L.; Ricca, T. L. *J. Am. Chem. Soc.* **1985**, *107*, 7893.

59. Beegle, L. W.; Wdowiak, T. J.; Robinson, M. S.; Cronin, J. R.; McGehee, M. D.; Clemett, S. J.; Gillette, S. *Astrophys. J.* **1997**, *487*, 976.

60. Beegle, L. W.; Wdowiak, T. J.; Arnoult, K. M. *Astrophys. J.* **1997**, *486*, L153.

61. Sloan, G. C.; Bregman, J. D.; Geballe, T. R.; Allamandola, L. J.; Woodward, C. E. *Astrophys. J.* **1997**, *474*, 735.

62. Diogo, H. P.; Kiyobayashi, T.; Minas da Piedade, M. E.; Burlak, N.; Rogers, D. W.; McMasters, D.; Persy, G.; Wirz, J; Liebman, J. F. *J. Am. Chem. Soc.* **2002**, *124*, 2065.

63. Dziewonski, K.; Rapalski, G. *Chem. Ber.* **1912**, *45*, 2491.

64. Dunitz, J. D.; Weisman, L. *Acta. Crystallogr.* **1949**, *2*, 62.

65. Bowen, E. J.; Marsh, J. D. F. *J. Chem. Soc.* **1947**, 109.

66. Livingston, R.; Wei, K. S. *J. Phys. Chem.* **1967**, *71*, 541.

67. Cowan, D. O.; Drisko, L. E. *J. Am. Chem. Soc.* **1970**, *92*, 6286.

68. Haga, N.; Takayanagi, H.; Tokumaru, K. *J. Org. Chem.* **1997**, *62*, 3734.

69. Sun, J.; Grutzmacher, H.; Lifshitz, C. *J. Am. Chem. Soc.* **1993**, *115*, 8382.

70. Geigle, K. P.; Hohlneicher, G. *J. Molec. Struct.* **1999**, *480-481*, 247.

BIOGRAPHICAL SKETCH

John James Banisaukas III was born in Greer, South Carolina, on August 25, 1974, to John and Carol Banisaukas. He has a younger sister, Heather, who received a Master of Science degree in materials science and engineering from the University of Florida. John graduated magna cum laude from Furman University with a Bachelor of Science degree in chemistry in June of 1996. He earned a Master of Science degree in physical chemistry from Furman University in August of 1997. John enrolled in the University of Florida in August of 1997 in pursuit of a Doctor of Philosophy degree in physical chemistry.

I certify that I have read this study and that in my opinion it conforms to acceptable standards of scholarly presentation and is fully adequate, in scope and quality, as a dissertation for the degree of Doctor of Philosophy.

Martin Vala

Martin T. Vala, Chair
Professor of Chemistry

I certify that I have read this study and that in my opinion it conforms to acceptable standards of scholarly presentation and is fully adequate, in scope and quality, as a dissertation for the degree of Doctor of Philosophy.

R. E. Hummel

Rolf E. Hummel
Professor of Materials Science and
Engineering

I certify that I have read this study and that in my opinion it conforms to acceptable standards of scholarly presentation and is fully adequate, in scope and quality, as a dissertation for the degree of Doctor of Philosophy.

Nils Y. Ohrn
Professor of Chemistry

I certify that I have read this study and that in my opinion it conforms to acceptable standards of scholarly presentation and is fully adequate, in scope and quality, as a dissertation for the degree of Doctor of Philosophy.

William Weltner Jr.

William Weltner, Jr.
Professor of Chemistry

I certify that I have read this study and that in my opinion it conforms to acceptable standards of scholarly presentation and is fully adequate, in scope and quality, as a dissertation for the degree of Doctor of Philosophy.

Richard A. Yost
Professor of Chemistry

This dissertation was submitted to the Graduate Faculty of the Department of Chemistry in the College of Liberal Arts and Sciences and to the Graduate School and was accepted as partial fulfillment of the requirements for the degree of Doctor of Philosphy.

August 2003

Dean, Graduate School